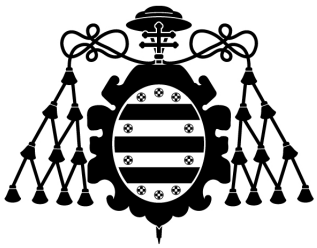

Universidad de Oviedo
Universidá d'Uviéu
University of Oviedo

Master's Degree in Advanced Physics:

Particles, Astrophysics, NanoPhysics and Quantum Materials

Studying the Submillimetre Galaxies Magnification Bias by Simulating their Stacked Lensing Effect

Carlos Alonso Álvarez

Supervisors:
Laura Bonavera
Joaquín González-Nuevo González

July 12, 2022

Contents

1 Introduction **5**
- 1.1 Historical Aspects and some Clarifications about Lensing . . . 5
- 1.2 Magnification Bias in the Framework of Cosmology and Astrophysics . . . 9

2 General Relativity **14**
- 2.1 Standard Cosmological Model: Cosmological Parameters & Distances in Cosmology . . . 14
- 2.2 General Relativistic Bending of Light . . . 18
- 2.3 Lensing Phenomena . . . 22
- 2.4 Weak Gravitational Lensing: Magnification Bias . . . 26

3 Previous Works, Motivation and Framework **30**
- 3.1 González-Nuevo et al. 2014: Cross-Correlation Indicates (Weak) Lensing Phenomena . . . 30
- 3.2 Bonavera et al. 2019: Magnification Bias through Stacking . . . 30
- 3.3 Fernández et al. 2022: The Right Choice of Profile . . . 32

4 Methodology **36**
- 4.1 Sources: Redshift Distribution and Selection . . . 36
- 4.2 Cross-Correlation Estimators . . . 38
- 4.3 Dark Matter Profiles . . . 40

5 Simulator Development and Toy Model **47**
- 5.1 Toy Model (I): Magnification and Source Counts . . . 51
- 5.2 Toy Model (II): Cross-Correlation Functions . . . 58

6 Results **72**
- 6.1 Profile Characterisation . . . 72
- 6.2 Reviewing Bin 4 of Richness from Fernández et al. 2022 [1] . . . 84

7 Conclusions **87**

A Extra Theoretical Notes **95**
- A.1 Cosmological Parameters (I): Newton's Mechanics with a Some Concepts from Cosmology . . . 95
- A.2 Cosmological Parameters (II): Non-Stop Flight from FLRW to H(z) . . . 99
- A.3 Galaxies and Clusters are Bound . . . 101

B Coding Lines **103**
- B.1 Random Fluxes . . . 103
- B.2 Maps of Counts . . . 104
- B.3 CCF Construction and Fitting . . . 113

C Additional Figures **119**

ABSTRACT

This work is a review of the properties about background (e.g. submillimetre galaxies) and foreground sources (e.g. clusters of galaxies or massive bound dark matters regions) that an algorithm built up to simulate the cross-correlation function between them is able to reproduce in the framework of Weak Gravitational Lensing (WGL). This cosmological phenomenon has been proven as a solid observable in order to constrain not only astrophysical parameters regarding the Halo Ocupation Model but also parameters of the current Cosmological Concordance Model ΛCDM. The cross-correlation function (CCF) between two families of sources (as explained in section 3.1) is shown to track the magnification bias effect induced by WGL. Knowing so, further works have also revealed that the stacking method, when applied to deflectors of similar size and characteristics, is able to feature better the cross-correlation at small angular scale.

A methodology section is presented in order to comment the various steps and requirements that have to be applied over the samples (sources) selection in those works. This will help to understand some of the limits that will be put on some of those properties. The estimators and statistics used to work with the simulated data are also presented in this section, which concludes with a summary of the models for the dark matter profiles, the magnification and cross-correlation functions.

The simulator offers a good opportunity to understand the effects of magnification bias on the background source counts first. Section 5 accounts for this, explaining the various regions of the magnification functions and how they translate into maps of counts. Then we move on to work with simulated cross-correlation functions and the reconstruction of properties from the dark matter profiles. Those profiles have been used to produce the magnification functions, which are related to the theoretical CCFs by simple equations, that alter the intrinsic flux of the background sources.

Among the most interesting results we have obtained, stands out the detection of a plateau-like behaviour of the CCF where strong lensing (measured as where the magnification function reaches certain high values) occurs. Although at first we thought it was some kind of statistical flaw of our computations, we discovered that it was due to the distribution of intrinsic fluxes assigned to the background sources. Therefore, it should extend as well to realistic works with real data. In any case, this effect can only be perceived when the amount of data that is available to be treated is large enough. Observed CCFs by our main reference, Fernández et

al. 2022 [1] (FER22), showed this behaviour at low angular scale, prompting the presence of a brightest central galaxy (BCG) at low angular scales at the centre of clusters. The trends did not blow up, according to our observations of the plateau with the simulator. Although the amount of data that FER22 used in their works was not comparable to the number of simulated sources we used, the lowest bins of richness in which they separated the samples had enough statistics to ensure that this plateau-like behaviour is also present in real work with data. Therefore, we concluded that WGL and the induced magnification bias is also useful to unveil characteristics of the background sources -their intrinsic flux distributions-.

Finally, in section 6 we showed that our simulator could be used to reconstruct compound profiles as the ones used in FER22. We were able to obtain a readout of four parameters at the same time and discussed the possibility of performing a precision-level analysis, concluding that the variability of the readout depending on the input values was important. At the end of that section we reviewed the work by FER22 by trying a new model to explain the gaps observed in their CCFs. Particularly, we explored their results for the fourth bin of richness, we discovered that a case in which the oscillatory behaviour was so relevant at angular scales beyond the scope of the BCG could well be reproduced if the outer term is replaced or added up with a compound of SIS profiles. This is not only relevant for its use to keep track of the observed trend in their works, but also because the masses needed for such combination of profiles are well in line with expected masses for average or medium-sized galaxies ($\sim 10^{11} - 10^{12}\ M_{\odot}$). Moreover, the angular scale at the redshift of clusters (~ 0.3) is compatible with typical distances between galaxies within them. Certainly, an oscillatory behaviour as the one described should be studied even further in detail. Beyond that analysis, our simulator is able to reject any statistical flaw as the reason behind it. If anything, statistical issues such as a lack of sources at certain angular scales due to limited data (e.g. the fourth bin of richness in FER22 only counts with 424 detected background sources) can only exaggerate the effect, but when great numbers of sources are used (e.g. the first or second bins of richness) the effect is still seen. This is an indication that there is physics yet to be unveiled in this issue.

'Everyone is pleased, the relativists [...] who are suddenly experts in a field they hardly knew existed [and] the astrophysicists for having enlarged their domain, their empire, by the annexation of another subject -general relativity-.'

Thomas Gold before the 1st Texas Symposium on Relativistic Astrophysics (1965)

1 Introduction

This introduction is aimed to present the effects of lensing from a descriptive point of view, since it does not constitute typically a main issue in undergraduate courses of General Relativity or Astrophysics. Apart from a historical introduction to that effect, we will address the most interesting concepts of **dark matter** and **magnification bias** and differentiate the three main regimes of lensing, focusing on **weak lensing** since it is basic in this work.

In the second subsection, the use of weak lensing magnification bias to constrain cosmological and astrophysical parameters is reviewed presenting state-of-the-art results in the area. It is not our task to constrain cosmological parameters nor the main Halo Occupation Model astrophysical ones but rather work with the cross-correlation and magnification functions and their mass and concentration parameters. However, dependency on several cosmological parameters is manifest. For that reason, it is natural to comment on the results obtained by recent research.

1.1 Historical Aspects and some Clarifications about Lensing

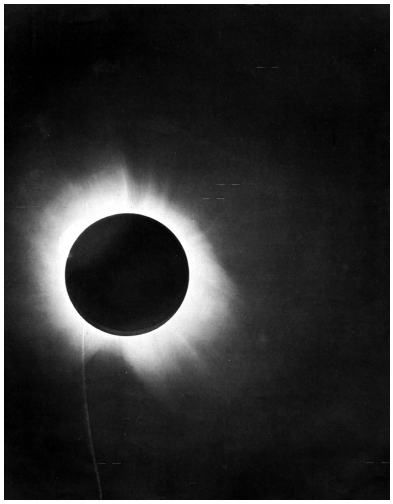

Figure 1.1: Figure shown in the original paper by Dyson et al. 1920 [2] between pages 292 and 293.

The first description in science of gravitational lensing does not come from Albert Einstein's Theory of General Relativity, but much earlier when Isaac Newton theorised that in case light was regarded as a particle with mass, it would be deflected when passing near a massive object. We know today that photons do not carry mass, which would be otherwise forbidden from a relativistic point of view. The fist measurement of light deflection in the framework of General Relativity took place in 1919 [2], and constituted the very first empirical proof[1] of the newborn theory of Geometry and Gravitation by Albert Einstein. The experimental work by Dyson, Eddington and Davidson proved that light from nearby stars that should fall behind the sun by their celestial coordinates -the moment a solar eclipse was taking place- could be seen around our star. The deflection of the light rays followed the bending angle predicted by General Relativity, and not the one (half the value[2]) they would in the classical theory from Newton, being corpuscular massive particles.

[1] Along with the good description of the perihelion precession of Mercury's orbit.

[2] Some comment on this point will be made in section 2.

Although these first results involved physics in a flat space-time, in which all that is needed is a Minkowski metric with a transition to a Schwarzschild metric[3] in some particular moments, gravitational lensing at cosmological scales requires from an understanding of the metric of Friedmann-Lemaître-Robertson-Walker and the framework of the ΛCDM model. According to conventional wisdom, when people are asked about *Lensing Phenomena*, figures as the ring-shaped galaxies around foreground deflectors at some cluster of galaxies arise. For example figure 1.2 is an actual[4] picture of how a Luminous Red Galaxy (LRG) can deflect the incoming light from a background galaxy in such a way that distorts its shape.

Apart from astonishing imagery, the role of lensing in science is state-of-the-art when it comes to applications in cosmology and dark matter research, as will be reviewed in the following subsection and in section 3. There, magnification bias through weak lensing is the main object of the discussion. Since the present work relies in source counting as a source of valuable information, and is triggered by the results from works presented in those sections, some basic concepts that appear everywhere in those papers should be commented on before. These concepts are **dark matter**, **weak (vs. strong and micro) lensing** and **magnification bias**.

Figure 1.2: Red Luminous Galaxy LRG 3-757 strongly deflecting light from a background galaxy, distorting it to form a ring around the foreground source. Picture from NASA (Hubble Space Telescope) [3].

Dark matter is needed in order to explain the shape and deepness of potential wells where galaxies and clusters of galaxies fall. The history behind its *discovery*[5] is quite long and controversial; nevertheless, it is hard to argue in favour of the existence of something that has not been directly measured -nor most of its properties[6]-. For it being established as a widely recognised problem -see the article from de Swart et al. from 2017 [4] where a deep insight into the history of dark matter is displayed-, physics had to wait until the 1970s. Two papers tend to

[3]Only needed when discussing deflection of light rays or some other interesting phenomena that involve massive compact objects such as our star.

[4]Possibly colours are allocated following photometric techniques in several bands.

[5]It is rather inaccurate to say it has been discovered since it has not been. We could say instead that it was postulated.

[6]Although we know some things, and particularly this work aims to characterise the magnification and cross-correlation functions associated to certain types of mass-distribution profiles describing dark matter.

be acclaimed for being responsible for the standardisation of dark matter into modern physics and dragging the attention of scientists to do research in the topic. The people behind them were Fritz Zwicky, who worked in describing the virial stability of clusters of galaxies realising that much more than the visible baryonic mass was needed to match the kinetic energy of the particles[7] within (around 1930); and Vera Rubin, who was the first scientist to study the rotation curves of a nearby galaxy, Andromeda (M31), finding[8] that there was a lack of mass if the baryons alone were to explain them. The paper from Rubin and Ford gave research a push into rotation curves, what in the end resulted in many more papers analysing them and finding evidence for the lack of matter (from 1970 onwards).

When Cosmology started being the great-scale general relativistic counterpart[9] of the Standard Model of Particle Physics, dark matter fitted as a natural part of the model. Great obscurity[10] remains around it, though. However, some of the properties that dark matter was found to have proved to be -from the point of view of several theorists- as safe points to redirect physical research into the *true* discovery of dark matter. One of the most accepted options is that it is made up of fundamental particles that could be included as an extension to the Standard Model. The range of beyond the standard model theories that have new particles is quite explosive[11] so as to be commented here, so we restrict the discussion to mentioning axions. This candidate has consistently been reviewed as most promising; thus we refer to the review by Marsh in 2016 [7]. It constitutes a comprehensive explanation of axions from their conception in the QFT framework to the role several models of them played in the various stages of the universe.

Regarding our involvement with Dark Matter this introduction is more than enough to set the stage. Turning away in order to address the different regimes of lensing we aim to draw a distinction between them. All throughout this work, we are going to work with **weak lensing**. This is no different from the type of phenomena that Dyson, Eddington and Davidson studied,

[7]The word particles, in this context, refer to Galaxies or bound structures that were explained and mostly -as we will see reading from Rubin's work, it is not accurate to say so- understood by that time.

[8]In the referred article there is a full explanation on how the breakthrough was perceived at that time, arguing that there were doubts in the scientific community regarding how the rotation curves were extrapolated and its implications.

[9]This is my way of saying that the standard cosmological model also has input parameters, a complex model developed and many open questions ahead with some tensions the community thinks will lead to new physics in the coming future.

[10]The word *dark* blurs a bit the intention of Herni Poincaré when he described this type of matter -theorised by Lord Kelvin some time before- (see reference [5] from Bucklin (2017) for further information on historical aspects) as *elusive* or hard to define. The word he used in french *obscure* [*matière*] possibly referred to its rather unknown nature.

[11]The paper from Roszkowski et al. from 2018 [6] offers a wide view on the current status of Weakly Interacting Massive Particles (WIMPs) -theorised fundamental particles- candidates.

but it being addressed from a cosmological point of view offers widely new opportunities. As a general description, WGL covers all the phenomena that occurs far[12] enough from the lens. This is any macroscopic effect having to do with position change -deflection by an angle-, flux increase and small distortions in shape. The last requirement is worth a slow read: we are not talking about the stunning deformations observed of ring-shaped strong lensed background galaxies as that of figure 1.2, but rather little twists and size changes.

If a whole cluster was affecting background sources weak lensing would be hard to spot by eye from randomly shaped galaxies, unless a mathematical approach is used e.g. source counting of sources above certain flux. Figure 1.3 represents the effect a cluster of galaxies could make on a background population of sources, with some preferred direction of shear that can be hardly identified in case the real sources do not have all the same intrinsic shapes.

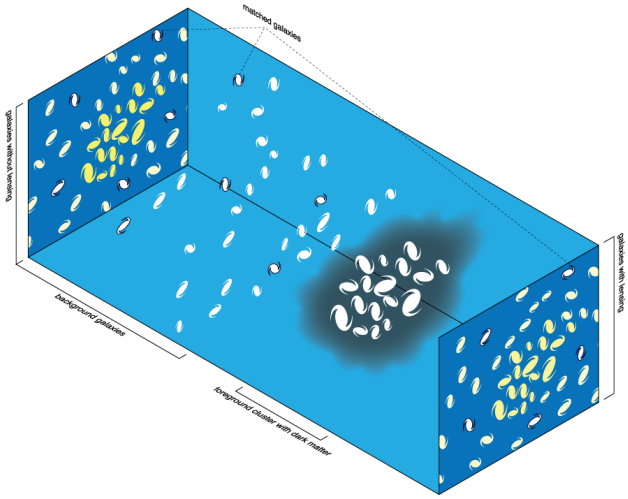

Figure 1.3: Representation of how a population of background sources would be seen around a deflector -e.g. a cluster- in a case with magnification (bottom-right map) and without it (upper-left panel). In the magnified case, a slight oriented distortion in shape can be perceived. Figure taken from the Wikimedia repository of free media [8].

Microlensing is another known variety of lensing which has been honoured with a very own name since it is useful to uncover hidden objects -due to our telescopes flux or resolution limited capacities- thanks to the interposition of massive fast[13] moving deflectors. This creates transient phenomena that can be studied through optical techniques. Further from strict theoretical definitions whatsoever, the use we are going to make of strong and weak lensing during some parts of the work can be rather confusing with respect to what has been explained in the last paragraph; for that reason we explain it here. We will sometimes refer to strong lensing when sources undergo[14] magnifications greater than some value -typically a factor $\sim 2-4$ of magnification is enough to take sources from being non-observable to being recorded by detectors if a minimum intrinsic flux of sources is set around 10 mJy-. Due to the shape of the dark matter profiles, the magnification and cross-correlation functions will also present some characteristic shapes when plotted against angular separation. Weak lensing

[12] In the plane of the lens, e.g. at great angular scale.
[13] Galaxies do not move *fast* on human timescales, but compact objects can.
[14] We know it since we create the magnification, the source and the intrinsic flux.

and *extreme*-weak lensing, as we have coined when referring to arcmin-separated regions from the deflector where magnification asymptotically meets the unity, fall further away from the deflector than strong lensing regions.

Working with actual sources and their shapes can be tiring since requires quite a lot of effort put into every single source. Counting sources, instead, relies on simply putting restrictions to the acceptance of sources according to some criteria. This way, an extensive gathering of sources can be undergone and one can count with big amounts of data to perform analyses. The effect that weak lensing has on the total number of observed sources is called **magnification bias**. It is in fact the object of science that we will use all throughout this work.

1.2 Magnification Bias in the Framework of Cosmology and Astrophysics

Current research in the field of Cosmology aim to constrain the main cosmological parameters that set a certain evolution of our universe in time, according to a theoretical-observational model known as ΛCDM (standing for the cosmological constant Λ and the dark matter component[15], which is though to be made up of fundamental -yet unknown- massive particles). Some[16] of those parameters are the Hubble constant H_0, the tensor to scalar ratio r, the parameter of the equation of state of the dark energy w_Λ, the present amplitude of matter fluctuation σ_8, or the density parameters of the different types of cosmological fluids today $\Omega_{i,0}$. The current stage of research in Cosmology is the precision-level Cosmology, not guessing which theory fits best our observations of the universe, but rather once we have accepted the ΛCDM model as our basic scheme, putting competitive constraints in the values of the parameters aforementioned. Weak Gravitational Lensing has emerged as a novel observable when it comes to constraining parameters of the model, as will be explained in the following lines. Apart from that, it has the unique feature -with respect to the other observables used in Cosmology- to provide researchers with information about some characteristics of dark matter haloes and astrophysical properties of the sets of galaxies used as sources. Particularly, dark matter haloes attached to baryonic-matter and standard-model-radiation emitters such as QSOs or Clusters of Galaxies have been studied in detail by Bonavera et al. 2019 [9] (hereafter BON19) and Fernández et

[15]CDM means *Cold Dark Matter*, for it should be non relativistic and have an equation of state comparable to that of ordinary (non-relativistic) baryonic matter.

[16]Many other parameters not mentioned in the text are important for the full understanding of the ΛCDM model or intlation theories. Some of them will be explained in detail in the theoretical section as they would have critical effects on the magnification and cross-correlation functions used when working with cosmological lensing phenomena.

al. 2022 [1] (hereafter FER22) respectively. Sections 3.2 and 3.3 are dedicated to these papers, since they will be the basis of this work as they offer insight into the description of dark matter haloes using the magnification bias effect derived from WGL phenomena.

Weak Gravitational Lensing as an Observable to Constrain Parameters in the Framework of the ΛCDM Model

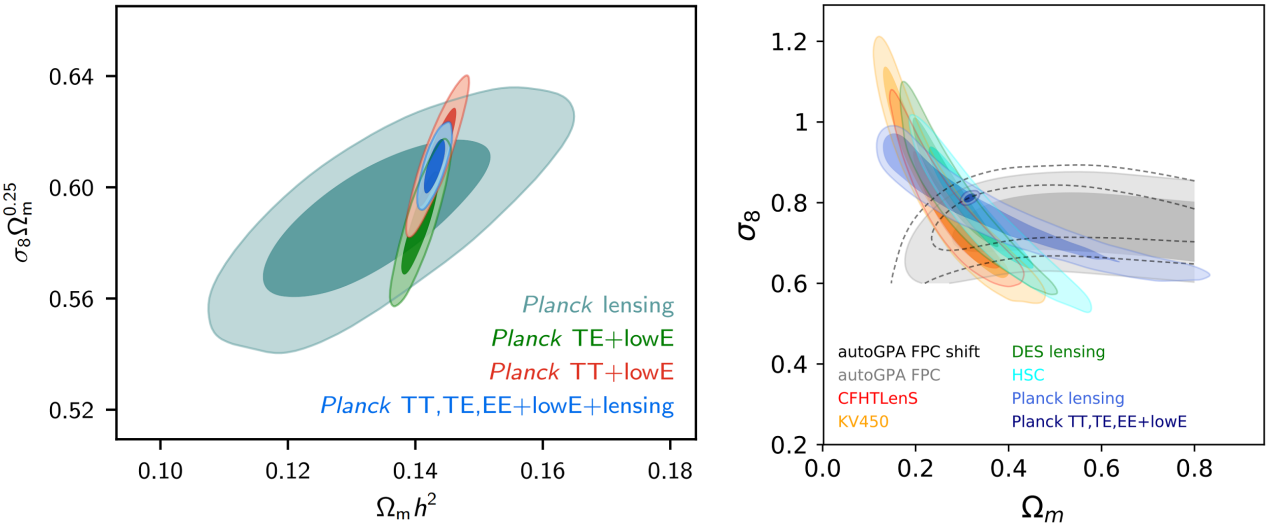

Figure 1.4: Left panel (figure 6 from Planck18) shows the results on the compound parameters of $\Omega_{m,0}\cdot h^2$ and $\sigma_8\cdot\Omega_{m,0}^{1/4}$ providing confidence level regions. They take into account some observable features -the richest case in terms of the amount of them used is plotted in blue- of the CMB. The right panel (figure 10 right from BON20) shows the competitive confidence levels that an auto-correlation analysis of the SMGs magnification bias can provide. Particularly relevant are the results constraining the σ_8 parameter.

Analysts of data and experimental scientists in Cosmology and Astrophysics have been using a varied range of observables (e.g. the Cosmic Microwave Background, the Baryon Acoustic Oscillations or the type Ia Supernovae) to put competitive limits to those parameters. The reason behind it is that some of these observables are *blind*[17] in a degeneracy level; this is, a region of the possible values for two or more parameters is valid to account for the observed data. For example, the Planck Collaboration in their results of 2018 [published in 2020] [10] (hereafter Plank18) showed that the CMB results combining several features of the CMB such as the power spectrum or measurements of lensing effects on it using temperature and polarisation are able to provide constraints to the confidence regions for several parameters. The left panel of figure 1.4, numbered as the sixth figure in the aforementioned paper, shows confidence levels between[18] $\Omega_{m,0}\cdot h^2$ and $\sigma_8\cdot\Omega_{m,0}^{1/4}$. There is a region of confidence that covers a really narrow

[17]To be understood as unable to provide an unambiguous readout of a certain parameters, but only certain of a set of combined values for several observables.

[18]These are compound parameters from the original base parameters -some of which where mentioned in the previous paragraph-. They are chosen this way so that the plot remains more linear than when plotting σ_8 vs.

interval for the first variable ~ 0.14 while some more degeneracy is allowed in the second one $\sim [0.58, 0.62]$, in an almost linear correlation. Also, results on the degeneration in pairs of other parameters can be seen in figure 5 of that paper, where the concept of *degeneracy* can be so easily understood by looking at the $\Omega_{m,0}$ vs. $\Omega_{CDM,0}$ -dark matter density parameter- plot. When plotting degenerate confidence regions for a certain pair of parameters obtained from different observables altogether, one restricts further the confidence regions.

This is just an example of how cosmological parameters can be constrained through one cosmological observable as the CMB, possible one of the most popular ones for its strong constraints and good results. Lately, as commented in the first paragraph, WGL has been of great use to put competitive constraints on some of the parameters -e.g. Bonavera et al. 2020 [11] (BON20) and González-Nuevo et al. 2021 [12] (GN21)-, and the great results obtained for physics beyond the ΛCDM model in Bonavera et al. 2021 [13] (BON21) makes it a contender to provide further insight in the field of the wide reange of cosmological parameters.

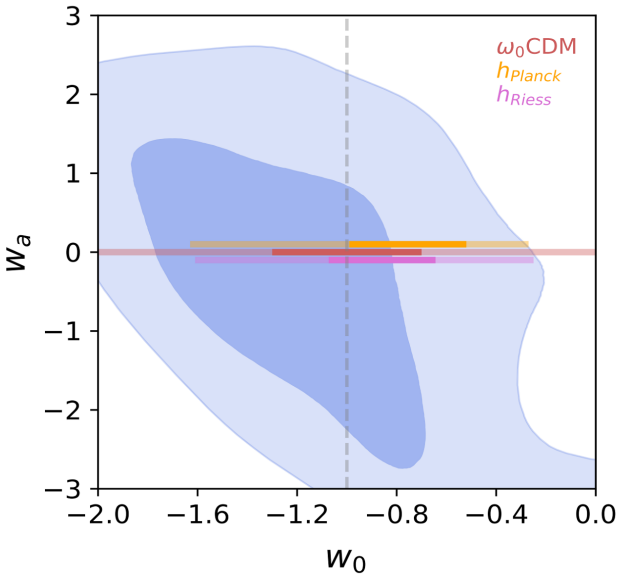

Figure 1.5: Results in the plane w_a vs w_0 regarding one evolution model with refshift for the dark energy equation of state. Figure 10 from BON21.

Reviewing the work of BON20 (grey CL region in the right panel of figure 1.4), we see that although poor limits were obtained for the $\Omega_{m,0}$ parameter, the σ_8 one was competitively determined in comparison to some other current studies. When it comes to the overall confidence levels, it was only overtaken by the results of Planck18 when all the features of the CMB were taken into account (the little dark-blue circular region in the plot). GN21 obtained at a 68% confidence level some better results than BON20 by performing a tomographic analysis, as can be seen in their seventh figure.

When it comes to beyond the ΛCDM model, BON21 tried to put into test a theory in which the parameter of the dark energy equation of state was allowed to evolve with redshift (time). This is described with two parameters w_0 and w_a, which should return -1 and 0 as

$\Omega_{m,0}$ as seen in the results from BON20 -right panel of the figure- (see the reference in the following paragraph).

experimentally obtained values in case the parameter of the equation of state was to remain constant. The results, as shown in figure 1.5, are indeed competitive with respect to the results shown by Planck18 using the variety of *sub*-observables from the CMB used in figure 1.4 (for the dark-blue CL regions).

Weak Gravitational Lensing as an Observable to Constrain Astrophysical Parameters and Dark Matter Halo Models

From an astrophysical point of view, perhaps the most interesting applications of WGL and magnification bias are the constraints on the Halo Occupation Distribution (HOD) model parameters. In many of the reviewed papers, BON19, BON20, BON21, González-Nuevo et al. 2017 [14] (GN17) and GN21 , this issue is addressed. The HOD is a model that explains the probability of finding a central galaxy in a halo depending on its mass. Then, satellite galaxies are contemplated when a certain mass level M_1 is achieved, following a power law that depends on a parameter α (check BON20 for a good description that can be further followed in references given there). The results obtained in any of these papers show robust correlations between the parameters, namely $M_{\rm min}$, M_1 and α.

Astrophysics regarding dark matter haloes came to another level with the work of FER22. Trying to use the stacking method to discover the presence of central galaxies haloes superposed to the general halo of their host clusters is quite of a novel technique that allows us to study magnification functions from up close. In section 3.3 this work will be reviewed and, indeed, it is the one we will refer to mostly during the results and toy model sections. Nevertheless, the aim of this work is to develop a simulator able to distinguish brightest central galaxies (BCGs) due haloes from general haloes that are common to all clusters. The idea behind FER22's work -previously introduced by BON19- is that maps of counts can be used as a synonym for the shape of magnification profiles. Just as an astronomer that works with photometry uses photons to trace images of science, an astrophysicist or cosmologist can use the maps of background galaxy counts to trace magnification profiles.

From the wide range of options up for study; i.e. ΛCDM parameters, HOD parameters, and other astrophysical opportunities, only the latter will be central in this work. Regarding the other two, the HOD model will be completely separated from anything that we will directly or tangentially address here, so no further development will be done. When it comes to ΛCDM parameters, the previously mentioned papers do not rely on the stacking technique to put constraints on them; however, some parameters -$\Omega_{\Lambda,0}$, $\Omega_{\rm m,0}$ and H_0- enter in the definition

of the dark matter profiles and their magnification functions. It is possible, therefore, that stacking is used to constrain cosmological parameters when all the dependence on any other variable is sufficiently well constrained. In any case, that is something that goes beyond the scope of this work.

2 General Relativity

When working with events at a cosmological scale, some background of general relativity is needed. Namely we need to build up the lens equation for gravitational lensing phenomena working with distances in megaparsecs. What is more, some key parameters or variables needed (mainly distances) are hidden from us. We will need to work with angular distances, but we typically know them thanks to the redshift of the objects we work with -a feature that telescopes can indeed measure thanks to photometry and spectroscopy-.

We will begin with some basics of General Relativity and the ΛCDM model, commenting on the Friedmann-Lemtaître-Robertson-Walker metric, the parameters of the Concordance Model and how they affect the variables within mathematical expressions related to the lensing effect.

Once the Cosmology basics are displayed, a brief introduction into the theoretical framework of light deviation is given, following the most traditional derivation from the geodesics equation. Nevertheless, this will be a fast way to get to the deflection angle without losing theoretical accuracy. With all this knowledge gathered, we will be able to build up the (gravitational) deflection potential. From there, mathematical expressions for the convergence, magnification function and magnification bias are obtained.

2.1 Standard Cosmological Model: Cosmological Parameters & Distances in Cosmology

Galaxy X at redshift z_X would be a sentence to be commonly found in a work similar to this one, or perhaps in papers alike those that will be discussed later on in section 3. Distances then, which will enter critically in theoretical lensing expressions, have to be treated from a general-relativistic and cosmological point of view.

The metric[19] used then takes the analytic form of equation 2.1, where we have loosened up the curvature parameter k, and chosen it to be a freely varying parameter in $\mathbb{R}$. Note as well that $[k] = [r]^{-2}$ is kept so that S_k in equation (2.2) has units of distance. Despite this introduction of the parameter k, the aim of this work is not considering or constraining the associated density parameter for the curvature Ω_k. When the time comes, the parameter will be set to 0 as the concordance model suggests we live in a flat universe, or at least one in which the radius of

[19]There are several ways to write down the analytic expression for the metric and all of them are the same from a physical point of view. Another choice in the definition

curvature[20] is far beyond the observable limit.

$$ds^2 = -c^2\ dt^2 + a^2(t)\left(\frac{dr^2}{\sqrt{1-kr^2}} + r^2\ d\Omega^2\right) \tag{2.1}$$

For further references, equation (2.1) displays the metric of Friedmann-Lemaître-Robertson-Walker (FLRW). Equation (2.2) introduces the resolution of the comoving distance, parameterised by the the curvature k. It is calculated radially $d\Omega \equiv d\theta^2 + \sin^2\theta d\phi^2 = 0$ and instantaneously $dt = 0$, so our only dependence is in r and k.

Note that with this definition, the FLRW metric could be rewritten as $ds^2 = -(c\ dt)^2 + a^2(t)\,(dr^2_{\text{comv}} + r^2_k(r_{\text{comv}})\ d\Omega^2)$, after having renamed $S_k \equiv r_{\text{comv}}$. That was a way of having the comoving distance as a lonely parameter and putting all the dependence on the curvature on the r_k function, which is nothing but the inversion of $S_k(r)$.

$$S_k(r) \equiv \int_0^s \frac{ds(r,k,t)}{a(t)} = \int_0^r \frac{dr}{\sqrt{1-kr^2}} = \begin{cases} k^{-1/2}\sin\left(r\ k^{1/2}\right) & (k > +1) \\ r & (k = 0) \\ k^{-1/2}\sinh\left(r\ k^{1/2}\right) & (k < -1) \end{cases} \tag{2.2}$$

It would be a huge simplification to say that all modern Cosmology falls into knowing accurately towards the past and the future the shape of the scale factor $a(t)$; however, doing so, would give us solutions and certainty over a lot of open questions today. Similar to the latter equation is the evolution of the Hubble parameter with time, or alternatively as is our case, with redshift. Equation (2.3) shows the evolution of the Hubble parameter with redshift; the order we have chosen for presenting the density parameters of the different components is due to the present time standard model of their respective values.

We can take now the curvature to be 0, since we know that the first term of the equation is heavily supressed in the concordance model. For radiation, we know that it dominated only at the early stages of the universe. This means that we can also get rid of it. Finally matter and the cosmological constant are the main variables regarding the current expansion of the universe, with a incipient domination of the cosmological constant in a rate of ~ 0.3 vs 0.7 in its favour.

[20] Continuing with the idea of the previous footnote, another parameterisation of the parameter k would allow for the introduction of R_0 (the radius of curvature at present time) in the expression for the metric.

$$H(z) \equiv H_0 \cdot E(z) = H_0 \cdot \left(\Omega_{k,0}\left(1+z\right)^2 + \Omega_{\mathrm{rad},0}\left(1+z\right)^4 + \Omega_{\mathrm{m},0}\left(1+z\right)^3 + \Omega_{\Lambda,0}\right)^{1/2} \tag{2.3}$$

The density parameters today are defined as usual $\Omega_{i,0} \equiv \epsilon_{i,0}/\epsilon_{c,0}$. The critical density of the universe today $\epsilon_{c,0}$ is defined as $\epsilon_{c,0} = 3H^2/8\pi G$; and $\epsilon_{i,0}$ is the energy[21] density of a fluid of certain characteristics today.

Distance (e.g. the r coordinate in the metric) is the variable that matters us the most. However from a physical point of view it is not something measurable. To be accurate, the word *distance* accepts a lot of definitions from a cosmological point of view. When we refer to that r coordinate we are talking about the physical or *proper* distance. The fact that we live in an expanding universe spoils our ability to measure this quantity directly unfortunately, so we need another way to measure distances. As Ryden amusingly points out in her book [15], we would need a tape and instant communication -or at least a stop in the expansion of the universe while measurements of distance are taking place- between its two ends in order to measure this quantity.

Since working with angles and distances (angles) on the celestial sphere is needed[22], the right distance to be used is the *angular* distance. This is the notion of distance that we get when we divide the real size[23] of a source by its angular size on the celestial sphere. To be as much accurate as we can, the angular distance to the source multiplied by the sine of half the angle it subtends in the sky gives back half its real size. There's no need the use the sine of the angle however, since the biggest source that we can see in the night sky, which is the moon, only takes 31 arcmin. This allows for the approximation $\sin\theta \approx \theta$ being perfectly valid here.

$$d_A = \frac{\Delta x}{\delta\theta} \tag{2.4}$$

In the previous equation, Δx stands for the real size of the object, and $\delta\theta$ for its angular size on the celestial sphere. Essentially we would not need anything else to work our physics out, but

[21] Debate could be raised on the accuracy of using *energy* to describe the density ϵ. It is appropriate when we work in a relativistic framework -the whole derivation could be done just with thermodynamics-, and ϵ refers to the time-time component of the energy-momentum tensor $T_{\mu\nu}$. For a comprehensive theoretical path from equation (2.1) to equation (2.3), we refer to appendix A.

[22] To be thoroughly detailed in section 2.2.

[23] Obviously one cannot go to the light years apart the source falls to measure this, but for the most cases, we can make good approximations of the real size of the object from a comparison to similar ones that live closer to us, or by other physical helping hands. As Ryden puts it, we know a standard yardstick's real size, so placing it somewhere far away and measuring its angular size on the celestial sphere gives back a notion of distance.

since typically sources are measured by its redshift z, we would get our computations shorter if we had something that relates the latter with the angular distance, since redshift is easier to get[24]. First, knowing that we measure *sizes* in the plane of the celestial sphere, we can go back to the FLRW metric, and conclude that $\Delta x = a(t_e)\ r\ \delta\theta \equiv r\delta\theta/(1+z)$; where t_e stands for the time at which light was emitted. Again, to be accurate, Δx up there represents the size of the object when light was emitted, but the assumption that cosmological expansion is negligible for bound objects is natural. r is not something we can measure easily, but corresponds to the radial coordinate position in the comoving system. For its definition it corresponds to the proper distance, which can be expressed as a function of redshift as follows

$$\begin{aligned} r(z) &= c\int_{t_e}^{t_0}\frac{dt}{a(t)} = \frac{c}{H_0}\int_0^z dz'\frac{H_0}{H(z',\{\Omega_{k,0},\Omega_{\mathrm{rad},0}\}\approx 0)} \\ &= \frac{c}{H_0}\int_0^z \frac{dz'}{\sqrt{(1+z)^4+\Omega_{\mathrm{m},0}\,(1+z)^3+\Omega_{\Lambda,0}}} \end{aligned} \tag{2.5}$$

Several steps have been taken between the two terms at the right in the first line of previous expression[25]. Some of these are the relation between the Hubble parameter and the scale factor, then the relation between the differential of time and the differential of redshift etc. On the other hand, if we wanted to avoid integration, and just apply a simple equation at some moment we could refer to the simplifications made for example by Ryden. Expanding the Hubble parameter to first order in z, one finds the expressions below

$$d_p(t_0) \approx \frac{c}{H_0}z\left(1-\frac{1+q_0}{2}z\right) \quad \Rightarrow \quad d_A \approx \frac{c}{H_0}\frac{z}{1+z}\left(1-\frac{1+q_0}{2}z\right) \tag{2.6}$$

This is an approximation that works when the second derivative of the scale factor today is dominant over the their derivative, and can be extended back and forward in time as long as this holds[26]. q_0 is known as the *deceleration parameter* and is related to the second derivative of the scale factor by

$$q_0 \equiv -\left(\frac{\ddot{a}}{aH^2}\right)_{t=t_0} = \Omega_{r,0}+\frac{1}{2}\Omega_{m,0}-\Omega_{\Lambda,0} \tag{2.7}$$

where in the right-hand side of the equation has been used the acceleration equation. It can

[24]There are several experimental techniques to access it. For example, it can be calculated through photometry or spectroscopy.

[25]For further information one can refer, for example, to the lectures of Prof. Max Pettini [16].

[26]This is the relation that can be found in chapter 6 of Ryden's book; which works works well when close in time -or redshift-, as can be checked in figure 2.1

be derived from the first law of thermodynamics, as Ryden does (see section 4.3), and be written relating the scale factor and its second derivative with the energy density and pressure of an ideal gas that we introduce in the $T_{\mu\nu}$ of the general relativity: $\ddot{a}/a = -(4\pi G/3c^2) \cdot \sum_i (\rho_i + 3P_i)$. Alternatively P_i can be substituted by the equation of state corresponding to the certain component by $w_i\rho_i$.

Keeping with equation (2.5), we only need to substitute in equation (2.4) to have a closed expression that we can work with easily through numerical integration. The result and validity of the approximation made by Ryden are compared to the most accurate result given by equation (2.8) in figure 2.1, shown both in units of Mpc. It can be translated to units of $[c/H_0]$ by recalling that $c/H_0 \approx 4286$ Mpc.

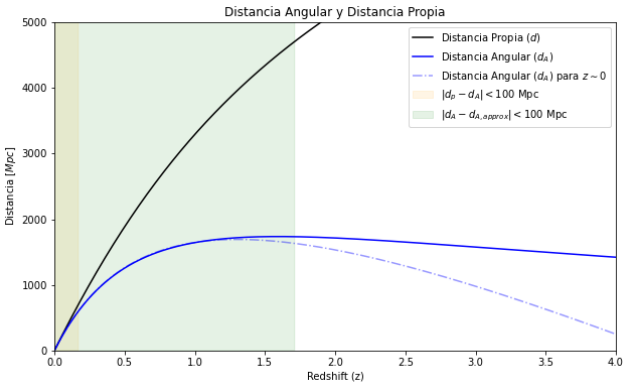

Figure 2.1: Proper distance (solid black), angular distance (solid blue) and the approximation for low z (dash-dotted blue). In addition, the regions where treating proper distance and angular distance (yellow) or angular distance and the approximation by Ryden (green) indistinctly mean a mistake of less than 100 Mpc are shaded.

$$d_A(z) = \frac{c}{H_0}\frac{1}{1+z}\int_0^z \frac{dz}{\sqrt{\Omega_{\mathrm{m},0}\,(1+z)^3 + \Omega_{\Lambda,0}}} \tag{2.8}$$

2.2 General Relativistic Bending of Light

With the arrival of General Relativity the mathematical expressions describing the lensing phenomenon were developed. We are following Carroll's book [17] on space-time and geometry to provide solid grounds, although there are hundreds of references with nice descriptions as well. At page 286, departing from working with the Einstein Equation, a weak intensity of the gravitational field $g_{\mu\nu}$ is imposed, decomposing the metric of space time as a flat Minkowski background $\eta_{\mu\nu}$ with a perturbation $h_{\mu\nu} = -2\Phi\delta_{\mu\nu}$. The gravitational potential Φ is defined after having set a gauge fixing for the gravitational field. It obeys the Poisson equation $\nabla^2\Psi = 4\pi G\rho$ and is defined after the split of the metric intro background and perturbation aimed at explaining phenomena arising from linearised gravity such as gravitational waves. $\Phi \equiv -1/2h_{00}$, in this case it also happens $\Phi = \Psi$; with $\Psi \equiv -1/6\delta^{ij}h_{ij}$, so that the perturbation becomes traceless.

We introduce the path of a massless particle split into background (straight Minkowski) and perturbation as $x^\mu \equiv x^{(0)\mu}(\lambda) + x^{(1)\mu}(\lambda)$. Then the wave vector and deviation vector as $k^\mu \equiv \dot{x}^{(0)\mu}$ and $l^\mu \equiv \dot{x}^{(1)\mu}$ respectively; where the dot stands for the conventional derivation with respect to the parameter. We can then write the geodesics equation for the light rays as

$$g_{\mu\nu}\dot{x}^\mu\dot{x}^\nu = 0 \tag{2.9}$$

The equation solved to first order simply gives $(k^0)^2 = \vec{k}^2 \equiv k^2$, so that when it gets introduced into the geodesics equation at first order[27] with $h_{\mu\nu} = -2\Phi\delta_{\mu\nu}$ results in

$$2\eta_{\mu\nu}k^\mu l^\mu - 2\Phi\delta_{\mu\nu}k^\mu k^\nu = -2kl^0 + 2\vec{k}\cdot\vec{l} - 4\Phi k^4 = 0 \tag{2.10}$$

The Christoffel simbols can be shown to be as equation (2.11) indicates[28]. Then one gets to $\dot{l}^\mu = -\Gamma^\mu_{\rho\sigma}k^\rho k^\sigma$, which is free of linear terms in l^μ since Φ is, as already said, first order in perturbation theory.

$$\begin{aligned}\Gamma^0_{0i} &= \Gamma^i_{00} = \partial_i\Phi \\ \Gamma^i_{jk} &= \delta_{jk}\partial_i\Phi - \delta_{ik}\partial_j\Phi - \delta_{ij}\partial_k\Phi\end{aligned} \tag{2.11}$$

We can work the equation of deviation split into its time component and its spatial components

$$\frac{dl^\mu}{d\lambda} = -\Gamma^\mu_{\rho\sigma}k^\rho k^\sigma \quad \Rightarrow \quad \frac{dl^0}{d\lambda} = -2k\left(\vec{k}\cdot\vec{\nabla}\Phi\right) \ , \qquad \frac{d\vec{l}}{d\lambda} = -2k^2\left(\vec{\nabla}\Phi - k^{-2}\left(\vec{k}\cdot\vec{\nabla}\Phi\right)\vec{k}\right) \tag{2.12}$$

Integrating the temporal part can be done easily[29]

$$l^0 = -2k\int\left(\vec{k}\cdot\vec{\nabla}\Phi\right)\,d\lambda = -2k\int\left(\frac{d\vec{x}}{d\lambda}\cdot\vec{\nabla}\Phi\right)\,d\lambda = -2k\Phi \tag{2.13}$$

Introducing this into the first order equation (2.10) yields $\vec{l}\cdot\vec{k} = 0$, verifying that the deflection occurs perpendicular to the flat trajectory. One can calculate the deflection angle observed in figure 2.2.

[27] First order requires either one deviation vector l^μ **or** the gravitational potential Φ in each term. This is the effect of the approximation taken above.

[28] Again, all this relies on the choice of the transverse gauge when defining the perturbation field, then setting some components of that field to zero (it be possible) and $h_{ij} = -2\Phi\delta_{ij}$ as it is manifest here.

[29] All integration constants can be dodged by making optimal choices of the initial conditions. For example, one can demand $l^0 = 0$ when $\Phi = 0$.

Now it seems like the perfect moment to introduce talking about angles in these circumstances as vectors: we have to measure distances between objects on the celestial sphere. The location of objects there is given by two coordinates (a vector), their difference is another vector whose modulus, **in the planar approximation**, is the *angle* we talk about all the time. In the case of $\hat{\alpha}$, it belongs to the plane perpendicular to the vector $\vec{k}$. Moreover, since no torsion can happen in the situation of figure 2.2, the vector[30] $\hat{\alpha}$ must be parallel to the vector $\vec{l}$, specifically

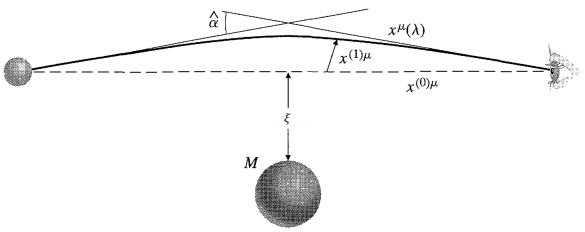

Figure 2.2: Sketch of the deflection of the geodesic $x^{\mu}(\lambda)$ a light ray follows, measured by the angle (vector) $\hat{\alpha}$. Figure taken from Carroll's page 288, there numbered as figure 7.3.

$$\begin{aligned}\hat{\alpha} &= -\frac{\Delta\vec{l}}{k} = -\frac{1}{k}\int \frac{d\vec{l}}{d\lambda}d\lambda = 2k\int\left(\vec{\nabla} - \frac{\vec{k}}{k^2}\left(\vec{k}\cdot\vec{\nabla}\right)\right)\Phi\ d\lambda \equiv 2k\int \vec{\nabla}_{\perp}\Phi\ d\lambda \\ &\equiv 2\int \vec{\nabla}_{\perp}\Phi\ ds\end{aligned} \tag{2.14}$$

where in the last two steps we have made two definitions; first $\vec{\nabla}_{\perp} \equiv \vec{\nabla} - \frac{\vec{k}}{k^2}\left(\vec{k}\cdot\vec{\nabla}\right)$, then we have made use of the physical spatial distance $s = k\lambda$.

The deflection vector $\vec{l}$, the impact parameter (yet to be introduced) and the deflection angle α are three vectors in close relation. The second one enters the potential Φ, and represents what is depicted in figure 2.2. Actually, we are using the same notation for coordinates, therefore the potential can be expressed as

$$\Phi = -\frac{GM}{r} = -\frac{GM}{\sqrt{\xi^2 + x^2}} \tag{2.15}$$

Performing the transverse ($\perp$) gradient simply implies doing its definition, or in short, the derivation sees the coordinate proportional to the impact parameter b as a constant, then one takes the derivative with respect to the other coordinates; in this simple yet general case, only

[30]**This footnote is important to keep track of what we mean when we introduce in an equation an angle**. In general we **will not** put the vector marker (e.g. $\vec{\theta}$) over an angle that has two components, but it is expected it be understood by the context (as the celestial sphere can be parameterised by two coordinates). All angles have two components, and referring to e.g. θ_i means the i component of the vector. When we put e.g. θ in general we will be talking about either the full vector or its module (to be understood from the text). For example the vector marker over the gradient in equations (2.14) or (2.26) explicitly implies that α is a vector there. Seeing an angle in a denominator, as in the convergence for the SIS model (4.4) is to be understood as θ being its modulus. In the case of the shear γ, since it is not strictly an angle, we will leave the notation γ for the full angle and $|\gamma|$ for its modulus.

x is to matter. The result is $\vec{\nabla}\Phi = -\left(\xi^2 + x^2\right)^{-1}\Phi\vec{\xi}$. Then we have a closed[31] expression for the deflection angle[32]

$$\hat{\alpha} = \frac{4GM}{c^2\xi} \tag{2.16}$$

However, this equation is only valid when we assume that the deflector mass can be thought as point-like, or its span shorter than the impact parameter ξ. In a more general computation one can write

$$\hat{\alpha} = \frac{4G}{c^2}\int d\xi' \int ds\ \rho(\xi', s)\frac{\xi - \xi'}{|\xi - \xi'|^2} \tag{2.17}$$

where the prime refers to the radial distance, in the plane where deflection occurs, of the mass element. The integration along the line of sight $\int ds$ is what is to be used, after we introduce some insights about distances in Cosmology, to relate convergence and the lensing potential. **It can be summarised that using equation (2.16) is appropriate when $\xi \gg \xi'$ and using (2.17) is appropriate otherwise**.

It is customary at this point to comment that Newton had arrived to half this result a few centuries before, which might not surprise us much, since a lesson that current Cosmology and General Relativity teaches is that radiation and matter may be not as much different as they might seem in our classical limit lives.

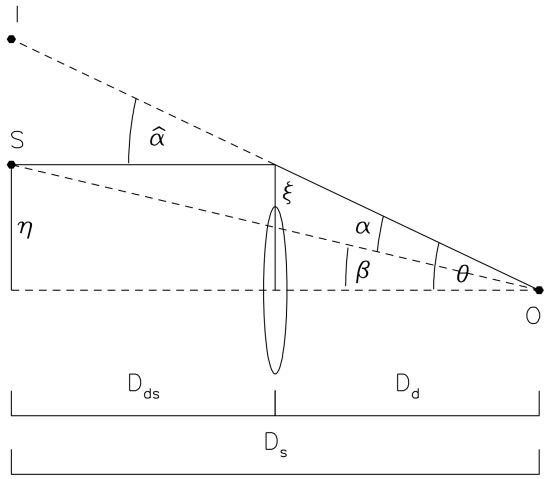

Figure 2.3: We can check all the angles and relations that happen among them. Picture obtained from NB97, there numbered as figure 5.

Once here, all that was needed from general relativity has been displayed. However, it is obviously useful to connect this with theory of lenses; in particular the region where deflection occurs can be thought of as a prism with refraction index

[31] We introduced **here** the factor c^{-2} to reverse the tradition by Carroll (which has been used all along, and is conventional) of doing calculations in general relativity with $c = 1$. We leave the factor to keep in mind that units are important. The c^{-2} that appears in equation 2.18 accounts for the same.

[32] We commented that Newtonian physics allow for light deflection if it was a massive particle -which is not-. The mathematical derivation following that hypothesis can be found in Soares' paper [18].

$$n = 1 - \frac{2}{c^2}\Phi \tag{2.18}$$

Nevertheless, the macroscopic effect of time delay that a medium other than vacuum exerts over light rays is an immediate computation that can be done; we refer to Carroll's for such derivation.

2.3 Lensing Phenomena

What makes our particular case of lensing distinct from, for example, the gravitational lensing produced by stellar objects in our galaxy that magnify stars from satellite galaxies (LMC, SMC...), is how we treat distances. To that end we had introduced section 2.1 since we have to work with angular distances. Figure 2.3, taken from Narayan & Bartelmann 1997 (NB97) [19], is valid in any context. For our case D_{ds}, D_d and D_s refer to angular distances.

From figure 2.3 we come across the lens equation $\theta = \alpha + \beta$. That sum can be made because the angles are measured by the same observer; however this does not hold in other cases. For example, $\hat{\alpha} \neq \theta$. If distances were proper, $D_{ds} + D_d = D_s$. In that case, $\hat{\alpha} = \theta$ as well. Just as happened with distances, the angles from figure 2.3 depend heavily on the redshift. In the cosmological case, physical invariants would be measurements made at the same redshift. For example, the distance between I and S in the figure cannot change depending on the angular distance and angle we use to measure it. We then come to the relation $\alpha D_s = \hat{\alpha} D_{ds}$, which combined with the lens equation translates into

$$d(I,S) = \alpha\ D_s = \hat{\alpha}\ D_{ds}\ \Rightarrow\ \beta = \theta - \frac{D_{ds}}{D_s}\hat{\alpha} \tag{2.19}$$

But angle $\hat{\alpha}$ had a closed expression as a function of the distance separating the light ray traveling towards us and the gravitational center of the deflector as shown in equations (2.16) and (2.17). This means that we can work with either $\hat{\alpha}$ or α. We are choosing the latter. In the $\xi \gg \xi'$ case this reads

$$\begin{aligned} \alpha(\theta) = \frac{D_{ds}}{D_s}\frac{4GM}{c^2\xi} = \frac{4\pi G\Sigma}{c^2}\frac{D_{ds}D_d}{D_s}\theta\ , \quad \Sigma(\xi) &\equiv \int ds\ \rho(\xi,s) \equiv \int ds\ \rho(D_d\cdot\theta, s) \\ &= \frac{M}{\pi\xi^2}\ \text{si}\ \xi \gg \xi' \end{aligned} \tag{2.20}$$

where Σ is a surface density defined in the plane of the lens, and we have taken into account[33] that $\vec{\xi} = D_d \cdot \theta$. This is a most important point: now the lens equation reads as a function β of the angle θ. When we are not working with the approximation commented in the paragraph above, but keep to equation (2.17) instead, the angle α would then be written as

$$\alpha(\theta) = \frac{D_{ds}}{D_s\ D_d}\frac{4G}{c^2}\int d\theta'\ \frac{\theta-\theta'}{|\theta-\theta'|^2}\int ds\ \rho(\theta', s) = \frac{D_{ds}}{D_s\ D_d}\frac{4G}{c^2}\int d\theta'\ \frac{\theta-\theta'}{|\theta-\theta'|^2}\Sigma(\theta') \tag{2.21}$$

We define the critical convergence (also named surface-mass density, as it has such dimensions) as the inverse of everything that multiplies $\Sigma\ \theta$ in equation (2.20), as specified in equation (2.22). If we fix a standard angular length at 1 Gpc so that the mix $D_{ds}D_d/D_s$ (which has units of distance) is measured in such unit, then we can express the critical convergence as

$$\Sigma_{\text{crit}} = \frac{c^2}{4\pi G}\frac{D_s}{D_d D_{ds}} = \frac{0.35\ \text{g cm}^{-2}}{\frac{D_d D_{ds}}{D_s}\ [\text{Gpc}]} \tag{2.22}$$

For the most general case, following equation (2.21), we would not get a great simplification by substituting the critical convergence, but for the approximation $\theta \gg \theta'$ we do get a simplified lens equation

$$\beta(\theta) = \theta\left(1 - \frac{\Sigma(\theta)}{\Sigma_{cr}}\right) \tag{2.23}$$

We define the Einstein Radius to be the angle at which a source is deflected when it sits back in the centre of the projected plane, equivalently $\eta = 0$ in figure 2.3.

$$\theta_E \equiv \sqrt{\frac{4GM}{c^2}\frac{D_{ds}}{D_d D_s}} \tag{2.24}$$

To get the notions and expressions of **convergence**, **magnification** and **shear** it is useful to start by defining a deflection potential[34] as

$$\psi(\theta) \equiv \frac{D_{ds}}{D_s\ D_d}\frac{2}{c^2}\int ds\ \Phi(\theta D_d, s) \tag{2.25}$$

ψ is built up so that its gradient in the direction of the angle on the celestial sphere matches

[33] Go back to figure 2.3 to recall the variables we are using.

[34] Shortly ago we introduced the concept of integrating the density function along the coordinate of the line of sight. Indeed the deflection potential has to do with this.

the angle α.

$$\alpha = \vec{\nabla}_\theta \psi = \frac{2}{c^2}\frac{D_{ds}}{D_s\ D_d}\int \vec{\nabla}_\theta \Phi\ ds = \frac{2}{c^2}\frac{D_{ds}}{D_s}\int \vec{\nabla}_\xi \Phi\ ds \tag{2.26}$$

which is essentially the same of equation (2.14) but for the factor D_{ds}/D_s and the c^2 coming from the restoration of c in equation (2.16). Now we have two expressions for α, the latter (2.26) and (2.21). We find, comparing those equations, that

$$\int \Phi\ ds = 2G\int d\theta'\ \Sigma(\theta')\int d\theta \frac{\theta-\theta'}{|\theta-\theta'|^2} = 2G\int d\theta'\ \Sigma(\theta')\ln|\theta-\theta'| \tag{2.27}$$

which we can introduce in the expression of the deflection potential to find the potential expressed as

$$\begin{aligned}\psi(\theta) &= \frac{D_{ds}}{D_s\ D_d}\frac{4G}{c^2}\int d\theta'\ \Sigma(\theta')\ln|\theta-\theta'| = \frac{1}{\pi\ \Sigma_{\rm crit}}\int d\theta'\ \Sigma(\theta')\ln|\theta-\theta'| \\ &= \frac{1}{\pi}\int d\theta' \kappa(\theta')\ln|\theta-\theta'|\ , \quad \kappa(\theta) \equiv \frac{\Sigma(\theta)}{\Sigma_{\rm crit}}\end{aligned} \tag{2.28}$$

It is straightforward to find out that the Laplacian of the deflection potential is proportional to the convergence κ, which is an important variable to compute the magnification, as will be seen soon.

$$\nabla^2_\theta \psi = \frac{1}{\pi}\int d\theta'\ \kappa(\theta')\nabla^2_\theta \ln|\theta-\theta'| = 2\kappa(\theta) \tag{2.29}$$

Finally since our objective was to relate θ (the angle to the image) to β (the angle to the source), we need the matrix of the change of basis between the angles $\mathcal{A}$.

The trace of the matrix of second derivatives of the potential is the Laplacian, and therefore can be substituted by the convergence. Also, the shear is defined from the orthogonal combination of the diagonal elements and from the antidiagonal ones

$$\gamma(\theta) \equiv \begin{pmatrix} \frac{1}{2}\left(\frac{\partial^2\psi}{\partial\theta_1^2} - \frac{\partial^2\psi}{\partial\theta_2^2}\right) \\ \frac{\partial^2\psi}{\partial\theta_1\partial\theta_2}\end{pmatrix} \equiv |\gamma| \begin{pmatrix}\cos(2\phi) \\ \sin(2\phi)\end{pmatrix} \tag{2.30}$$

The Jacobian matrix can be expressed then as a function of the convergence and the shear as follows

$$\mathcal{A}_{ij} \equiv \frac{\partial \beta_i}{\partial \theta_j} = \frac{\partial \left(\theta - \alpha\right)_i}{\partial \theta_j} = \delta_{ij} - \frac{\partial^2 \psi}{\partial \theta_i \partial \theta_j} \tag{2.31}$$

$$\mathcal{A} = \begin{pmatrix} 1-\kappa-\gamma_1 & -\gamma_2 \\ -\gamma_2 & 1-\kappa+\gamma_1 \end{pmatrix} = (1-\kappa)\cdot\mathbb{I} - |\gamma| \cdot \begin{pmatrix} \cos 2\phi & \sin(2\phi) \\ \sin(2\phi) & -\cos(2\phi) \end{pmatrix} \tag{2.32}$$

where the γ_1 and γ_2 represent each of the components of the shear vector and the $\mathbb{I}$ is the identity matrix.

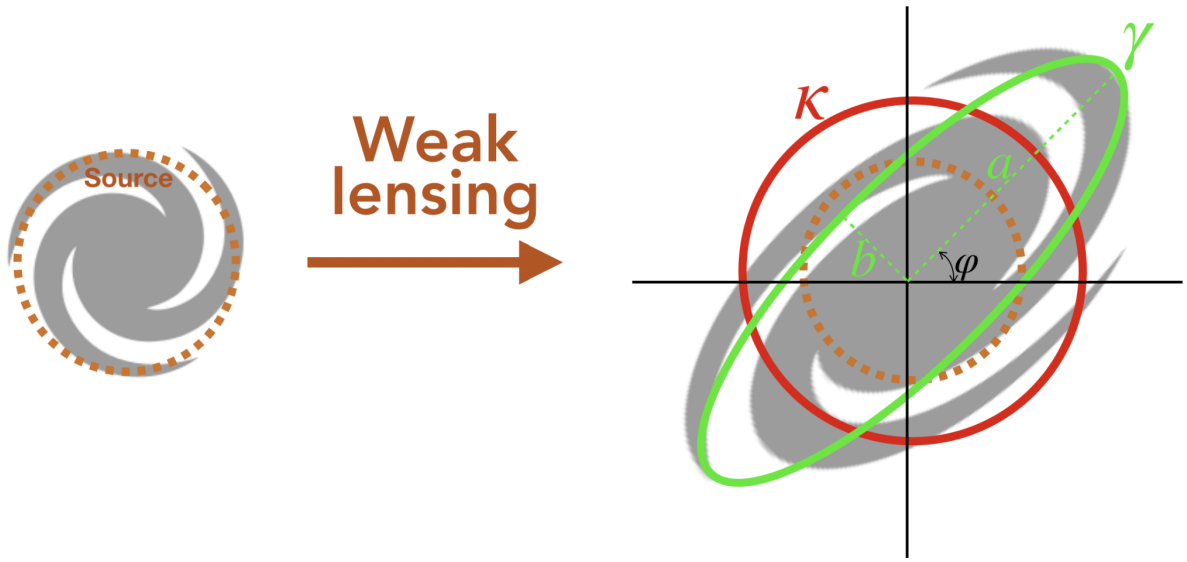

Figure 2.4: Combined effects of convergence and shear. Figure 2.3 from Shuntov 2019 [20].

The shear γ is defined by its modulus $|\gamma|$ and the angle of twisting of the stretched image in comparison to the direction drawn by any of the angles of the system (all of them are actually in the same direction). If the source was circular, its image would get stretched to be an ellipse with semiaxes $(1-\kappa \pm |\gamma|)^{-1}$. Finally the magnification equals the inverse of the determinant of matrix $\mathcal{A}$

$$\mu = \frac{1}{\det \mathcal{A}} = \frac{1}{(1-\kappa)^2 - \gamma^2} \tag{2.33}$$

The reason behind this is the invariance of the surface brightness distribution. A linearization of the lens equation gives the relation $\beta \sim \beta_0 + \mathcal{A}(\theta_0)\cdot(\theta - \theta_0)$ between two points $\{\beta_0, \beta\}$ and $\{\theta_0, \theta\}$ of the source and the lensed image respectively. From these two arguments we get $I^{(\mathrm{im})}(\theta) = I^{(\mathrm{s})}\left(\beta_0 + \mathcal{A}(\theta_0)\cdot(\theta - \theta_0)\right)$. The total flux of both images (the source and the lensed image) are given as integrals over these distributions. Since the distributions are equal, the

difference lies on the surface of integration, which is bigger (due to both magnification and shear) for the lensed image. The ratio among the fluxes, which is the ratio among the surfaces, is the magnification μ. Due to this reasoning, it has the expression shown above.

2.4 Weak Gravitational Lensing: Magnification Bias

The paper by Bartelmann and Schneider from 1999 [21] (BS99) prompts a few statements about the grounds and utility of WGL. Acknowledging that the intrinsic spherical shape of galaxies, individual work with galaxies through weak lensing seems hard and little significant. However, collective effects can throw deeper information with ease; for example an average uniform distribution of the distortion of images, exceeding the threshold of random noise due to random ellipticities of the sources, can give information about the strength of the magnification field.

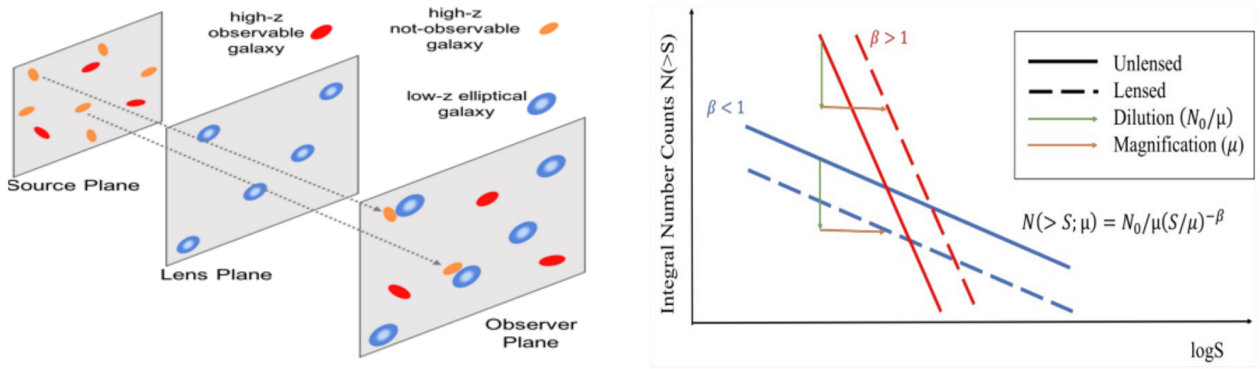

Figure 2.5: (Right) The amount of sources visible after WGL works depends critically on the exponent describing the number of source counts as a function of the flux. The Left panel sketches the amplification effect of WGL in sources of the correct kind. Figure 1 from BON22 compromises both panels

As said before, conservation of surface brightness creates an enhancement of flux due to the effect of magnification on the area of the image (in comparison to the source). But let's not stop there; suppose we have a detector with a threshold of flux below which sources cannot be distinguished. If magnification brings some sources whose intrinsic flux is below that level upwards, we will have an effect in the number of sources of a certain type that we will detect on the sky near to overdensities at cosmological scale (for example a cluster of galaxies).

We will work with the latter fact, as did the papers of Bonavera et al. from 2019 [9] (BON19) and Fernández et al. from 2022 [1] (FER22). The effect that lensing has on the source number counts can be thoroughly explained as in BS99. It can be summarized as

$$n(>S,z) = \frac{1}{\mu} n_0\left(>S/\mu, z\right) \tag{2.34}$$

where n represents the number of source counts of sources at redshift z with flux greater than a threshold S on the visible sky, and n_0 the number of sources that would be seen without magnification at the same redshift but with a threshold of flux modified to be S/μ. We can see two effects, as explained in Bonavera et al. 2022 [22] (BON22). First we see that flux limit is lowered $S \to S/\mu$ (more sources would be seen), and then the number of sources is diluted $\propto \mu^{-1}$, due to some sources exiting the region observed by the stretching of that region of sky.

It is usual to expect a distribution of sources as a function of flux following $n_0\left(>S,z\right) \propto S^{-\beta}$. Where β is referred to as the *source number count slope*. The choice of the type of background source is thereby a major concern, since the overall effect on the number of sources and the amount of statistics therefore available is critical; as shown in the right panel of figure 2.5. This means, in what concerns flux, the number of counts should follow a power law. Now there is also a part of dependence on redshift, with a factor $p_0(z;S)$ entering the proportionality. This is a statistical description of the probability of finding a source at redshift z with flux S.

We can write the factor between the sources that are seen and those that would be seen, with flux surpassing the threshold of detection, as

$$\frac{n}{n_0}\left(>S,z\right) = \mu^{\beta-1}\ \frac{p_0(z;S/\mu)}{p_0(z;S)} \sim_{\text{see text}} \quad \mu^{\beta-1} \tag{2.35}$$

We can neglect the dependency on redshift if we take into account that we will work at a fixed one. In the most realistic case, the redshift assigned to the sources will be bounded and we will assume that the probability of finding sources with a given flux changes slowly with redshift. Moreover, we can neglect the full factor by assuming that $p_0(S\mu) \sim p_0(S)$ for the sources that we are simulating (which fall close below/above the threshold).

We could aim to get rid of redshift from the very beginning, so we perform an integration of equation (2.34) over it

$$n(>S) = A\int \frac{1}{\mu}\left(\frac{S}{\mu}\right)^{-\beta} p_0\left(z;S/\mu\right)\ dz = A\int \mu^{\beta-1} S^{-\beta} p_0\left(z;S/\mu\right)\ dz \tag{2.36}$$

$$n_0(>S) = A\int S^{-\beta} p_0\left(z;S\right)\ dz = AS^{-\beta} \tag{2.37}$$

So that the relation $n(>S)/n_0(>S)$ is easily performed

$$\frac{n}{n_0}(>S) = \int \mu^{\beta-1} p_0\left(z; S/\mu\right)\ dz \sim_{\text{see text}} \quad \mu^{\beta-1} \tag{2.38}$$

For systems with lenses that fall not too much far away, one can neglect the dependency on redshift. Finally the integration over p_0 gives 1.

The bias, which will be named as w_x, in the number of sources can be written as a function of the magnification. This is the typical symbol used for the cross-correlation function, which will be thoroughly described in sections 3.1 and 4.2.

$$w_x(\theta) \equiv \frac{n\left(>S, z; \theta\right) - n_0\left(>S, z; \theta\right)}{n_0\left(>S, z; \theta\right)} = \mu^{\beta-1}(\theta) - 1 \tag{2.39}$$

The expression above is extremely useful when working with the stacking method (described in section 3.2), since sources are all distributed respectively to their separation to the lens on the celestial sphere.

When testing compound profiles, the analytical description of the process can become largely unmanageable. A simple game with the expressions of convergence and shear show us that

$$\begin{gathered} \Sigma \to \Sigma_1 + \Sigma_2 \quad \Rightarrow \quad \psi \to \psi_1 + \psi_2 \quad \Rightarrow \quad \left\{ \begin{array}{l} \gamma \to \gamma_1 + \gamma_2 \\ \kappa \to \kappa_1 + \kappa_2 \end{array} \right\} \\ \Longrightarrow \ \mu = \frac{1}{(1-\kappa)^2 - \gamma^2} \to M(\kappa_1, \kappa_2, \gamma_1, \gamma_2) = \frac{1}{(1-\kappa_1-\kappa_2)^2 - \gamma_1^2 - \gamma_2^2 + 2\gamma_1\gamma_2} \end{gathered} \tag{2.40}$$

which is in general different from any easy function of μ_1 and μ_2. From a physical point of view, however, one can make two natural assumptions -in order of accuracy to the real case- to work out the effect of two analytical dark matter haloes superposed that belong together into the same spatial region:

- As a first approach to the problem one can say that the haloes are different enough so that the parts where one becomes dominant with respect to the other cover the majority of the celestial area around the compound object; which means that except for a *small* annular region, the effect can be parameterised as one magnification profile (from the inner object) a transition region and another magnification profile. Since the transition is thought to be *smooth*, no greater problem should arise. Mathematically, equation (2.41) is

a good description, where $\theta_{\rm ch}$ refers to the angular separation where the dominant profile changes.

$$\mu(\theta) = \mu_{\rm inn}(\theta)\Theta(\theta_{\rm ch} - \theta) + \mu_{\rm out}(\theta)\Theta(\theta - \theta_{\rm ch}) \tag{2.41}$$

- The more accurate approach would require that, since magnification is[35] is always above 1, the product $\mu_1\mu_2$ behaves similarly to the magnification function of eq. (2.41). This is, the region where the profile 1 is less dominant, $\mu_2 \gg \mu_1$ or $\mu_2/\mu_1 \gg 1$ and vice versa.

[35]Supposing that demagnification does not occur in the region of interest $[\theta_{\rm min}, \theta_{\rm max}]$ where out data sample falls.

3 Previous Works, Motivation and Framework

In order to fully understand the work developed with the simulation, it is important to be familiar with the concepts of cross-correlation and stacking. Their usefulness is thoroughly explained in the papers featured in the following subsections respectively. Physical properties of the sources and profiles used in those papers, although the former are not a central issue in the current work, are to be explained afterwards in the methodology, section 4.

3.1 González-Nuevo et al. 2014: Cross-Correlation Indicates (Weak) Lensing Phenomena

The **Cross-Correlation function** (abbreviated as CCF) is defined as the probability of finding two sources of populations[36] A and B separated an infinitesimal distance, scaled by the probability of the random case. There are several statistical estimators to reproduce the CCF, each thought for a different purpose, to work with. This is further explained in section 4.2.

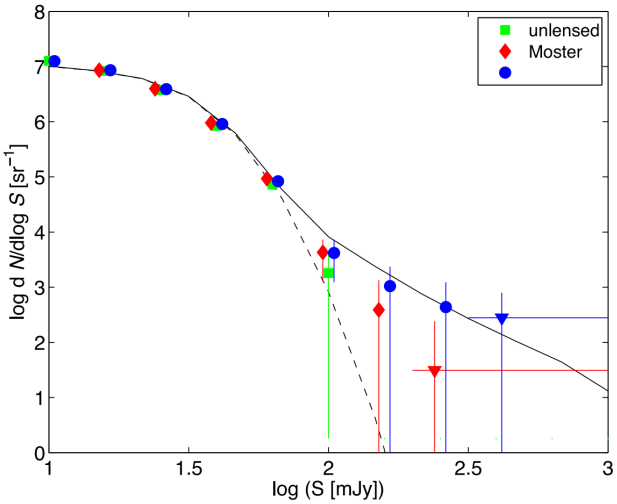

Figure 3.1: The number of counts function, which is proportional to the CCF, tracks the effect of WGL in the high flux region. Figure 14 of GN14.

González-Nuevo et al. 2014 [23] (GN14) showed that the CCF between sources of lens population and background population, see figure 3.1, track the effect of WGL in the high flux region, where few sources should be expected if the lensing effect was not working. The steepness of the number of counts respective to the flux helps enhance the effect.

3.2 Bonavera et al. 2019: Magnification Bias through Stacking

Traditional Cross-Correlation is calculated extensively with dependence on both the location of the lens and the location of the sources. However, it will be sometimes useful to work irrespective to the location of the lenses; this means, scaling everything to their position. The stacking technique relies on a principle basic from photography: an area -e.g. in our case this

[36] e.g. Deflectors and background sources (for example SMGs)

is the stacked area of several arcmin-sized regions of the celestial sphere- is represented by a number (or group of numbers). The idea is no different from what is done in astrophotography for some particular purposes such as photometry. The difference relies on us changing the (colour scale in figure 3.2) scale of the numbers associated to the pixels from a measure of the energy deposition to a measure of the number of sources seen at a particular position on the celestial sphere.

In BON19 the stacking method was used to characterise the weak lensing region of similar[37] lenses, which proved capable of producing a readout of the mass and concentration[38] of the dark matter overdensity associated to, in this case, QSOs. Obviously this has some risks when it comes to the reliability of the readout that any study of this kind produces. Notably, there is no physical requirement for every dark matter halo to be similar to any other; although one would naively ask any two galactic or cluster-like objects sharing most astrophysical properties to also share a similar dark matter distribution. Some other warnings to take into account are the apparent lack of knowledge about the real mass of the deflector, unless one makes use of a catalogue[39] that measures it by any other method; and the variability of the magnification function with the redshift of both populations.

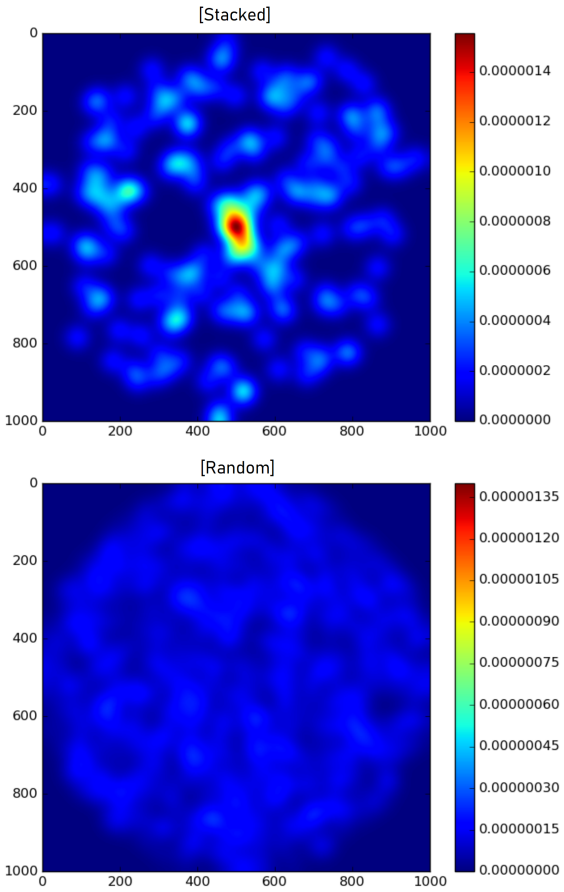

Figure 3.2: Filtered (with $\sigma = 2.4$ arcsec) and normalised amount of sources detected (upper panel). Filtered (idem) and normalised random case (simulated, bottom panel). 1000 pixels are used, with a 0.1 arcsecs per pixel, which covers a circular region of 50 arcsec in radius. Figure 2 from BON19.

In figure 3.2 the map of source counts after stacking is performed with the data of BON19 is shown. The same scale is used so that the comparison is completely clear: the notorious overdensity of sources visible in the centre is clear. Some randomness can be appreciated in the outer ($\theta > 10$ arcsec) region. Two main ideas can be driven out of this and without having to check the

[37]Some notes to be considered as limitations of the work and its results are given at the end of the paragraph.
[38]This parameter is linked to the type of profile used. In section 4.3 this and some other parameters related are described.
[39]The paper described in the next subsection covers the good agreement of a magnification-bias reconstructed mass and the mass measured in some catalogues.

CCF graph (figure 3.3), which shows it as well, nevertheless. First, the region closest to strong lensing can be well characterised by stacking. Second, and most important to the present work, we would like to know if an arbitrary amount of sources is able to blur the inhomogeneities at the central (outer in figure 3.2) weak lensing region.

Figure 3.3 shows the calculated CCF with the available data and stacking method. The aim of the upper panel is to show the improvement in the shaping of the CCF in the weak lensing region compared to the traditional[40] way of computing, relying in extensively computing the values of the estimator associated for every pair of sources. In the bottom panel the result of having applied a weak lensing approximation in the magnification function breaks at < 10 arcsec. This is due to the beginning of the strong lensing region. Still, no blow up of the data is perceived, but rather is a plateau; the function used for the fitting is also smoothed at that region. This raises another issue that we aim to answer, whether if an analytical solution can be given to work with the strong lensing region.

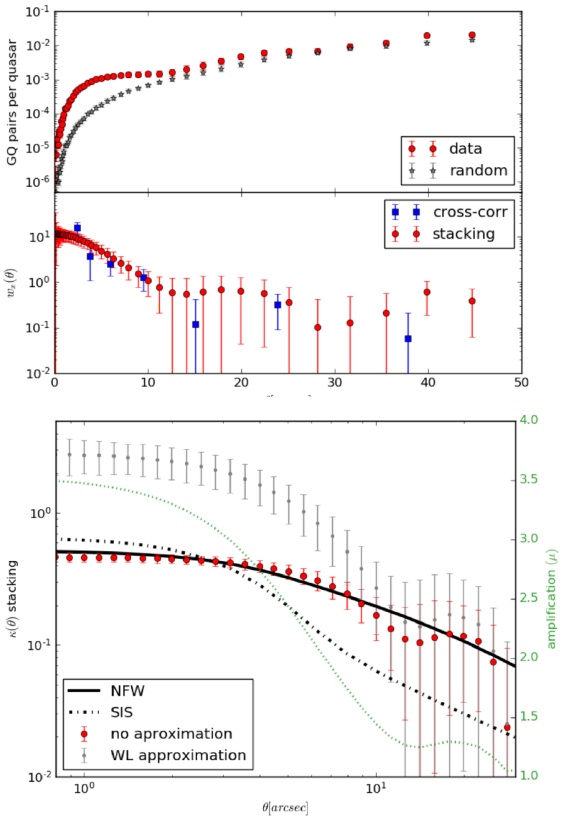

Figure 3.3: In the weak lensing region the CCF calculated by the stacking method gives a thoroughly detailed profile. Statistical fluctuations of the data series at larger distances spoils a good tracking in that region. Figures 4 and 7 bottom of BON19.

In the following subsection the ability of the current method to calculate the mass and concentration of the dark matter distributions is explored. BON19 does also estimate some values in this direction. They found[41] a combined estimation of $M_{200c} = 1.0^{+0.4}_{-0.2} \times 10^{14}\ M_\odot$ and $C = 3.5^{+0.5}_{-0.3}\ M_\odot$.

3.3 Fernández et al. 2022: The Right Choice of Profile

Although we tend to relate dark matter overdensities with the presence of bayonic matter (e.g. galaxies), these two types of gravitationally bound collectives are different things; and

[40] To get a clearer understanding of this, go to section 4.2, where this figure is referred to explain the difference between the Landy-Szalay and Davis-Peebles estimators when calculating the CCF.

[41] M_{200c} and C are described in section 4.3.

particularly from the former we know so little from a fundamental point of view. Clusters of Galaxies present a dark matter distribution, that is apt to be studied through weak lensing and stacking. In FER22 the magnification bias induced by these structures upon submillimetre galaxies (SMGs) has been evaluated. They test as well the hypothesis of a Brightest Central Galaxy (BCG) associated with a halo of itself that would produce a enhancement of the CCF towards lower distances ($\lesssim$ 10 arcsec). The choice we make of the dark matter profile for the mass distribution has a direct effect on the CCF as well. The main two profiles that are used in most of the literature are the Navarro-Frenk-White (NFW) and the Singular Isothermal Sphere (SIS), which are fully described in section 4.3.

		Bin 1	Bin 2	Bin 3	Bin 4	Bin 5	Total
SIS + NFW	$M_{\rm SIS}[10^{13}\ M_\odot]$	0.5	0.6	0.6	0.6	1.0	0.5
	$M_{\rm NFW}[10^{13}\ M_\odot]$	4.9	5.3	10.1	14.0	51.5	5.5
	C	0.94	0.30	1.17	0.65	0.56	1.84
Outer ($\lesssim$ 100 kpc)	$M_{\rm NFW}[10^{13}\ M_\odot]$	5.8	7.9	11.2	27.4	51.5	7.1
	C	0.74	0.39	1.00	1.74	0.56	1.72
Inner ($\gtrsim$ 100 kpc)	$M_{\rm NFW}[10^{13}\ M_\odot]$	3.8	2.3	7.2	1.0	1.0	4.1
	C	3.63	6.83	3.81	11.91	14.8	4.17
Inner + Outer	$M[10^{13}\ M_\odot]$	9.6	10.2	18.4	28.4	52.5	11.2
From catalogue	$\langle R \rangle$	14.6	20.9	31.4	50.4	91.4	20.0
	$\langle M_{200} \rangle\ [10^{13}\ M_\odot]$	7	11	18	32	64	11
	$\langle z \rangle$	0.38	0.39	0.37	0.32	0.24	0.38
	scale [kpc/$arcsec$]	5.42	5.51	5.33	4.85	3.96	5.42

Table 3.1: Results from FER22, labelled as table 2 in that paper. Upper row shows the fit of the CCFs with SIS (BCG) and NFW (general halo) profiles. The following three rows show the fit under a double NFW. Last row shows the available data from catalogues on several parameters.

Working with well formed clusters heavily restricts the overall number of lenses available, since only in recent stages of the universe have these objects had the time to get formed. In any case, more than 8000 targets (lenses) have been used, accounting for an average of $3-4$ detected attached background galaxies each. The amount of statistics is enough to produce a solid analysis and lenses could be divided in richness bins, following the hypothesis of greater richness means greater overall halo mass. The distribution of redshifts in each bin varies accordingly to the fact that greater structures were formed later in time, as depicted in figure 1 from FER22. Table 3.1 provides the measured masses and concentrations derived for the different richness bins, regions and mass density profiles. Additionally, the last row gathers the available information from catalogues on the measured mass, richness and redshift of the clusters. That figure should be regarded as a great summary of the work developed by FER22.

An interesting lecture driven from these results is the importance of the profile chosen to describe the dark matter halo responsible for the lensing effect. In figure 3.5 the CCF of the second bin of richness is shown, with a SIS+NFW fit at the right han side representing the BCG and general halo region respectively. At the right-hand side a double NFW profile was chosen. Although the NFW profile presents the disadvantage of an extra free parameter, the concentration, it was able to produce a much better combined mass estimation, in close accordance to the data available from the catalogues. In addition, the relevance of the BCG with respect to the richness group is also important, as can be fast checked in figure 3.4, as well as in table 3.1. Bins 1 and 4 were chosen to draw the comparison since bin 5 had poor statistics (few cluster-galaxy couples), big uncertainties and a variability that forced a fit by hand of the parameters. However the tendency of mass share of the BCG becoming smaller as richness increases is solid.

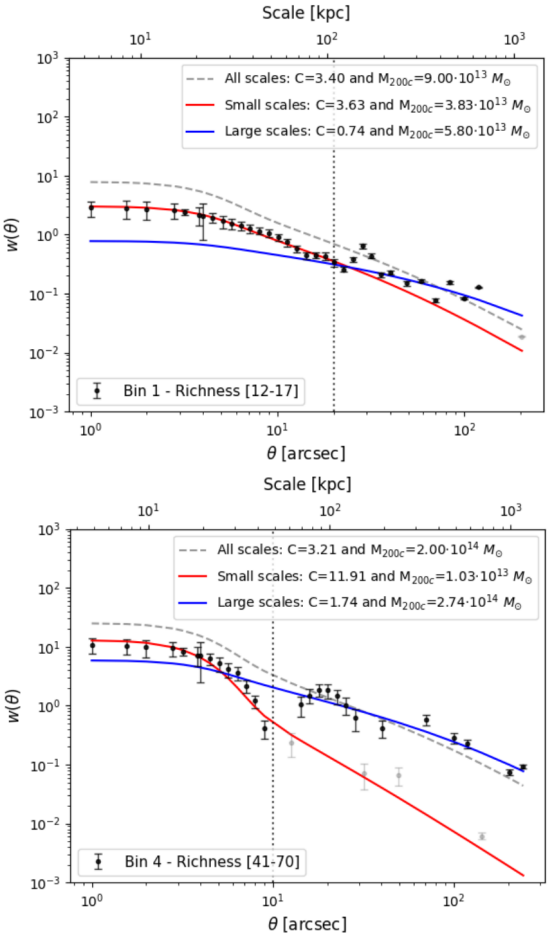

Figure 3.4: Bins 1 and 4 of richness from figure 5 of FER22. The inner BCG associated halo has a greater share of the total reproduced mass (up to the general halo) for lower richness. The readout vales for the mass can be read as well in table 3.1.

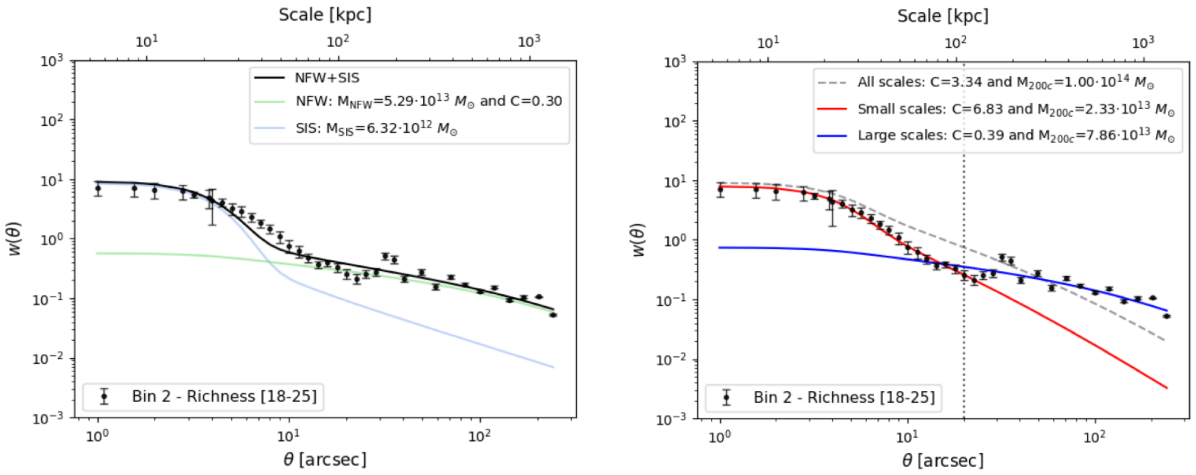

Figure 3.5: Plots of the CCF in the second bin of richness. At the left, for a fit with a combination of a SIS (BCG) and a NFW(general halo) profiles; at the right for two NFW profiles. The subplots belong to the figures 4 and 5 of FER22.

The perceptible lack of signal in their observed CCFs at $\sim$ 10 and $\sim$ 25 arcsec covers a whole part of the discussion section in the work of FER22. They realised that at all bins of redshift -particularly manifest in the fourth bin of redshift in the above figures- this feature was detectable, prompting of it being a non-richness dependent issue. They drew comparison to other works in which galaxies and clusters are reviewed and found that it was a common anomaly in all of them at the same angular scales.

Regarding the present work, the main idea to work with in our simulator and driven from the reviewed work is the reproducibility of the double-deck shape of the BCG-cluster halo terms in the CCF. The overall effect in terms of mass of each part is an input variable in any case, and something that is expected to work smoothly. However, our main concern is whether the double shape is distinguishable.

4 Methodology

The papers which we worked with in the previous section carry an extensive and thorough preparation and selection of the sources used. The aim of the current one is to provide the most important features of these choices, comment the expected variability of the CCFs with some of them or the suitability of certain type of sources. The cross-contamination in redshift is addressed in this part.

Once the sources have been well described, and an outline of the tests on the parameters that are going to be undertaken in our simulator is given, we will introduce the statistical estimators (the Landy-Szalay and Davis-Peebles ones we named when we reviewed the work of BON19) that build the CCF from the available data. At the end of that section the relation between the magnification bias and the distribution calculated from the estimators will be drawn.

We have left the dark matter density profiles to the end because they have some direct implications for the toy model that is to be explained afterwards in section 5. This section, although being theoretical to some extent, also presents useful figures which account for the differences between the two main profiles used, the Navarro-Frenk-White (NFW) and the Singular Isothermal Sphere (SIS).

4.1 Sources: Redshift Distribution and Selection

The redshift distribution of the sources, specially the lenses, is quite critical in modifying the angular distance that enters into the mathematical expression of the magnification and convergence; therefore a wide width of the distribution of the sources (e.g. parameterised by a normal distribution), this is, a big standard deviation, can produce a lack of reliability in the results. This has to be treated carefully.

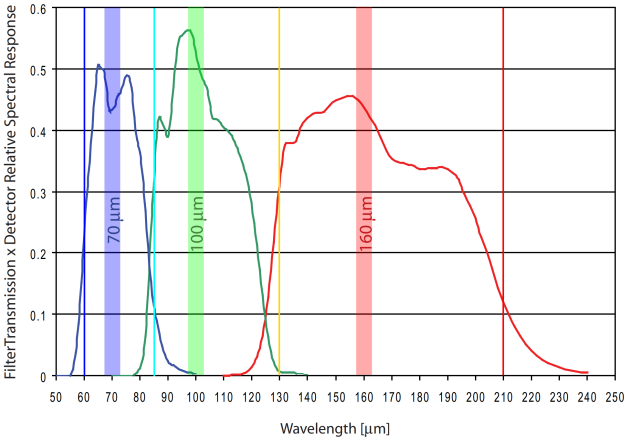

Figure 4.1: Bands from the PACS instrument, figure 6 from [24], including wavelengths in the range ~ 50 to ~ 200 µm. Referred papers work with data in the range $\sim$ 100 to $\sim$ 500 µm, where at $200 - 500$ µm enter the sources from SPIRE.

Apart from this, an extensive methodology has been developed to remove possible cross-contamination of sources, which should com-

promise with the type of background galaxies matching a steep source number of counts function with respect of flux (figure 2.5). This is quite well described in GN14, although almost all the referred papers above cover the issue.

To cover the selection procedure of the sources GN14 provide a thorough explanation, following the lines from Lapi et al. 2011 [25] (LAP11). Photometric bands are important in case we want to distinguish sources of different kinds, with spectral energy distributions peaking at different zones. Particularly submillimetre galaxies (SMGs) are expected at the infrared (near microwave) range, while many foreground sources are to be seen in the optical range. Apart from that, they have a steep slope of the source number counts with respect to flux $\beta > 3$, being an optimal sample for magnification bias studies, as commented back in section 2.4. The papers we have talked about worked with data from the Herschel-ATLAS data from the Herschel space observatory [26]. PACS [24] and SPIRE [27] are two of the three science instruments from the telescope, observing from 100 μm to 500 μm. Therefore, sources detected through these instruments are hardly misidentified with those with SED peaking in the optical. In figure 4.1 one can check the wavelength bands from the PACS instrument.

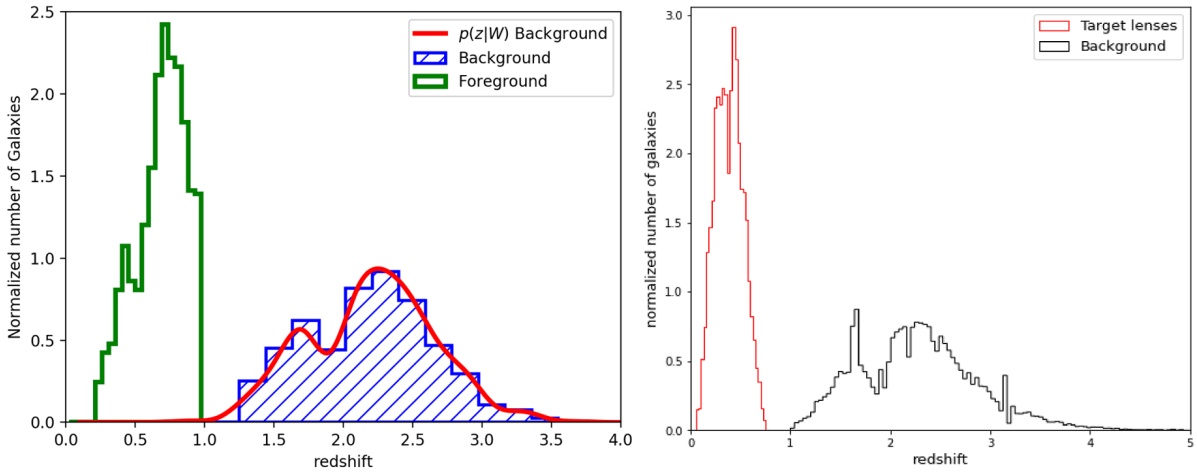

Figure 4.2: Redshift distributions of both background and foreground sources from BON19, figure 1 (left), and FER22, figure 1 top (right).

For the most recent data, used by BON19 and FER22, a 4σ detection is implicit at 250 μm (from SPIRE), with a threshold flux of detection of 29 mJy. In both works[42] a 3σ a detection limit was also applied to sources at 350 μm, thought to increase robustness and reliability. Sometimes a redshift limit in background sources is applied, BON19 uses the range $z_{\rm bkg} \in [1.2, 4]$ and FER22 impose a photometric lower limit, $z_{\rm bkg} > 1$. One can easily check

[42]Nevertheless, these criteria were already applied in the earliest papers in the field that we refer to, both LAP11 and GN14. The flux detection limit was slightly higher in those occasions, though.

that the distribution functions of both background samples (those of BON19 and FER22) smoothly (or almost) meet a normalized number of counts of 0 when $z \to 1$ (see the high redshift distributions -background samples- of figure 4.2).

When it comes to the prodecure to select foreground sources the addressed papers naturally take different approaches. Particularly BON19 aimed to study QSOs as hosts to halos the size of cluster ones whereas FER22 did not put any other restriction on the astrophysical detectable object that is attached to a cluster size dark matter halo than being detected as an actual cluster (from an astrophysical point of view). As a consequence, the catalogues used may differ. Indeed, although both use data from the SDSS (Sloan Digital Sky Survey), BON19 applied a specific target selection method[43], departing from the sources already used in Bianchini et al. 2019 [29]. They put a hard cutoff in redshift -in order to further avoid cross contamination-, limiting foreground sources to $z_{\text{fore}} \in [0.2, 1.0]$, which can be easily seen (at least for the upper limit) in the right panel of figure 4.2. For their part, FER22 opted to work with the catalogue of Wen et al. 2012 [30]. As explained in the article, it is made up of 132684 clusters with photometric redshifts in the range $z_{\text{photo}} \in [0.05, 0.8)$. Sources with greater masses ($> 10^{14}\ M_{\odot}$) tend to live at lower redshifts ($z_{\text{Big Clusters}} \lesssim 0.42$). These typically correspond to the ones we talked about in section 3.3 as belonging to bins of greater richness.

Not only are redshift limits applied in order to avoid cross-contamination, but since magnification functions depend on the angular diameter distance of the samples, particularly at $z \lesssim 1$ the wide of the range of redshifts chosen is critical. Having a limited range of redshifts for the samples could increase significance in comparison to an unrestricted case. At any rate, this enters as one of the features that is going to be studied with our simulator.

4.2 Cross-Correlation Estimators

References above have made use of mainly two estimators to compute the CCF, the one of Davis-Peebles (DP), eq. (4.1), and the one of Landy-Szalay (LS), eq. (4.2). We refer to Davis & Peebles 1983 [31] and Landy & Szalay 1993 [32] to further information about the statistical properties of both estimators. Concerning the DP estimator, the reference paper by Davis and Peebles uses a different notation, due to some sources not having changed (DR instead of RR). We have used however the notation introduced in BON19 and FER22, which makes sense as we only have one set of variable data: the random background sources distribution. Note that

[43] They refer to a detailed procedure explained in Ross et al. 2012 [28].

stacking fixes the location of all foreground sources into one place in our map.

$$w_x(\theta) = \frac{DD(\theta) - RR(\theta)}{RR(\theta)} = \frac{DD(\theta)}{RR(\theta)} - 1 \tag{4.1}$$

The way we have built up the magnification bias according to our variable parameter, the relative location of background sources on the celestial sphere with respect to the deflector, makes the DP estimator (4.1) refer to physically the same as did equation (2.39): both $DD(\theta)$ and $n(>S, z; \theta)$ are the number of counts in the real case, when magnification makes its effect; then $RR(\theta)$ and $n_0(>S, z; \theta)$ are the number of sources that would appear if magnification did not exist. On the other hand, we have the LS estimator

$$w_x(\theta) = \frac{D_1D_2(\theta) - D_1R_2(\theta) - R_1D_2(\theta) + R_1R_2(\theta)}{R_1R_2(\theta)} \tag{4.2}$$

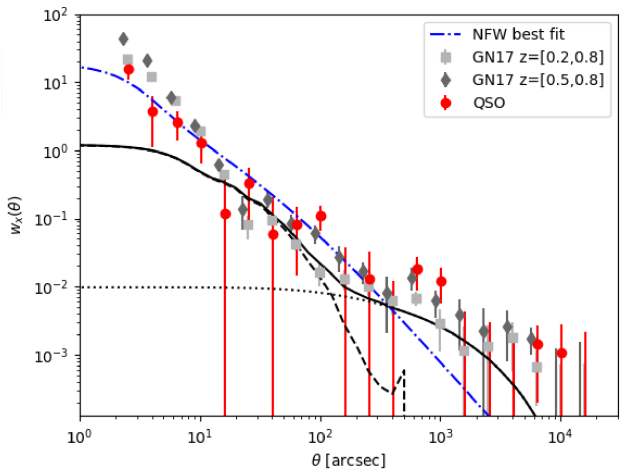

Figure 4.3: The double halo regime, observable at larger separations ($\theta > 100 - 1000$ arcsec) is only well outlined using the LS estimator. Figure 5 of BON19.

which needs both samples (background and foreground, e.g. 1 and 2 respectively) varying. It is not suitable in the current stacking case.

Apart from the appropriateness of using one estimator or the other depending on whether we resort to stacking, the choice also depends on what one wants to measure. For example, if we revisit the results from BON19, one can easily check that one estimator (DP) is more suitable than the other one (LS) at a certain range of distances between the lensed objects and the deflector(s). However, at higher distances only the LS estimator is able to reproduce the double-halo pattern that is shown in figure 4.3, taken from BON19. This feature is also analysed in GN14, figure 6, or in González-Nuevo et al. 2017 [14] (GN17), figures 2 and 4.

As for our simulator, the Davis-Peebles estimator is the one to be used, since the stacking method is one of the things to be tested in the various aspects that have already been commented.

4.3 Dark Matter Profiles

The nature of dark matter is still largely unknown; even so, FER22 succeded in realising that a Navarro-Frenk-White model describing the halo of the BCG works better than a Singular Isothermal Sphere profile. Differences between profiles in the magnification function and the CCF are sought, since they will help to further reveal properties of dark matter. In the present subsection we describe both profiles -NFW and SIS- to be tested, the theoretical building of their magnification functions, some particular parameters that enter their mathematical expressions (concentration and scale radius for the NFW and Einstein radius and the particles[44] velocity of dispersion for the SIS) and the shape of their CCF.

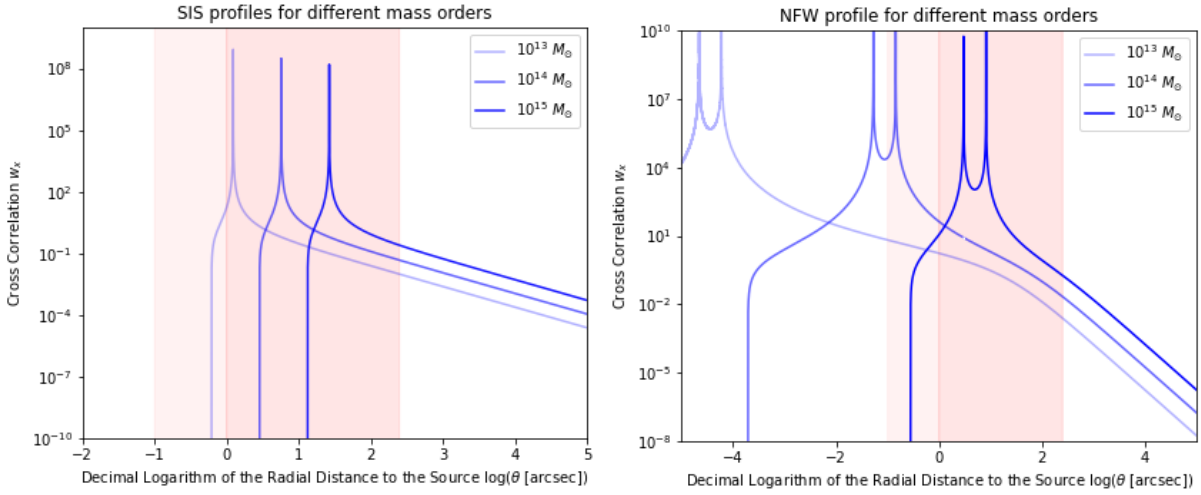

Figure 4.4: The CCF calculated from equation (2.39) after magnification takes the forms (4.5) and (4.8) for the SIS (left) and NFW (right) profiles. Masses were given in the range 10^{13} to 10^{15} $M_\odot$ as references. The red shaded region represents the typical field we are going to work with afterwards. BON19 and FER22 stacked sources in circular regions of radius 100 and 250 arcsec respectively.

In figure 4.4, where the CCFs of our dark matter profiles are presented, we have chosen 3 orders of mass as a reference. 10^{13} $M_\odot$ serves as a good example of a **thick** loner **galaxy** -associated to a perceptible concentration of dark matter attached to it-, although the main reason behind its choice is that it could work well to depict the effect of a BCG. 10^{14} $M_\odot$ is the typical intermediate case; nevertheless, 11×10^{13} $M_\odot$ or 1.1×10^{14} $M_\odot$ was the average value found for[45] the total M_{200} from catalogue and calculated value in the work of FER22 (see the last column in table 3.1). Therefore, that intermediate case would work pefectly well to describe a **typical medium size cluster of galaxies**. Finally, 10^{15} $M_\odot$ is the upper bound

[44] In this context *particles* would refer to galaxies or stars moving freely -in a theoretical way-.

[45] For a more extended explanation of some of the parameters used -e.g. M_{200} or r_{200}- we refer to the third subsection of appendix A, where the concept of virial mass is described following Sparke & Gallagher 2007 [33].

example of a **massive cluster**. Only few of them get to this mass order, and they would be recorded into the bin 5 from FER22. To give a nearby exmaple, the Virgo cluster would be characterised for a binding virial mass of this order. As discussed in general for objects from the fifth bin from FER22, these can only appear in the low redshift universe $z_{\rm fore} \to 0$, due to the time it takes these structures get formed. Concerning our simulation, the magnification profiles will be dependent on a series of variables, and so will the theoretical CCFs following equation (2.39). The two profiles being treated have dependency on several parameters

$$\mu_{\rm SIS} \equiv \mu(\theta, M_{200c}, z_d, z_s, \Omega_{\rm m}, \Omega_\Lambda, H_0) \ , \quad \mu_{\rm NFW} \equiv \mu(\theta, M_{200c}, z_d, z_s, C, \Omega_{\rm m}, \Omega_\Lambda, H_0) \tag{4.3}$$

Singular Isothermal Sphere (SIS)

This profile[46] is regarded as a typical example when studying the lensing effect theoretically since it departs from the simplification that all galaxies or stars within the halo should have constant velocities all throughout the halo. In this case the surface-mass density behaves as[47] $\Sigma \propto r^{-1} \propto \theta^{-1}$. Into the proportional factors enters the velocity of dispersion σ_v of the components that build it. The convergence can be written, in such case, as

$$\kappa(\theta) = \frac{\theta_E}{2\theta} \ , \qquad \rho_{\rm SIS} = \frac{1}{2\pi G}\left(\frac{\sigma_v}{r}\right)^2 \tag{4.4}$$

Thanks to that definition the convergence varies with the mass of the deflector. The shear and magnification are obtained as

$$\gamma = -\frac{\theta_E}{2\theta}\begin{pmatrix}\cos(2\phi)\\ \sin(2\phi)\end{pmatrix} \ , \quad \mu = \frac{1}{1-\theta_E/\theta} \tag{4.5}$$

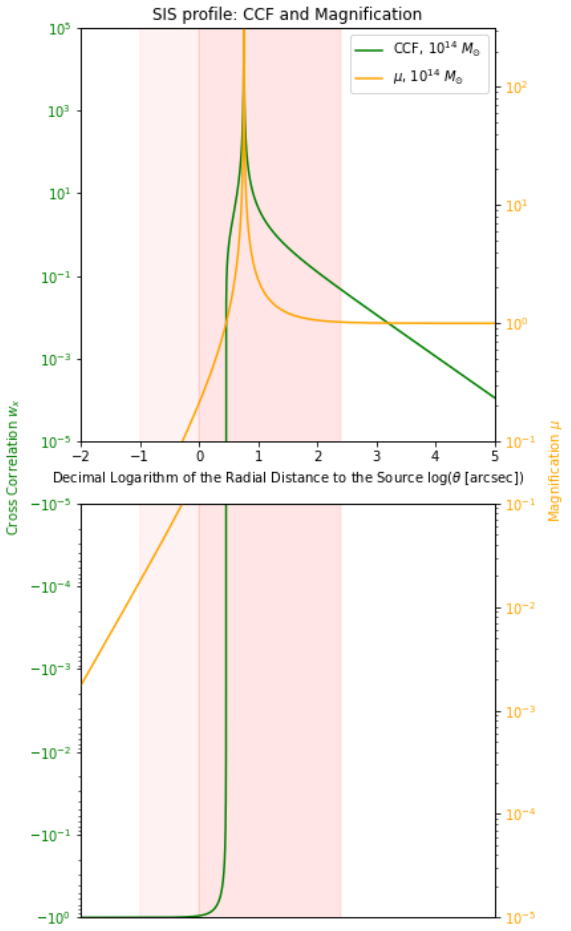

Figure 4.5: CCF (green) and magnification (yellow) functions for the intermediate case of 10^{14} $M_\odot$. The demagnification region can be appreciated towards the left.

Although the SIS profile is regarded as unphysical due to its singularity at $\theta = 0$, as well the fact that the integration of the density function up to infinity does not return a finite mass.

[46] An extended explanation can be found in section 3.1.5 of BS99.

[47] Here we call $b \equiv r$, to be consistent with the notation we use for the NFW profile.

However, since we can write the convergence (and from it the magnification and CCF) as a function of a given mass, we can introduce it as a parameter.

The identification of the SIS profile as a good description for the shape of the dark matter distribution in a galaxy or cluster sized object would be easy if we find the characteristic sharp demagnification drop at the left-hand side of the CCF function, as can be seen in figure 4.5. So far, FER22 used the good fit of the double NFW profile (see again table 3.1 and 3.5) to return the mass order of the foreground sources that catalogues provided, in comparison to the rather bad fit of the SIS+NFW profile. However, looking at the left panel of figure 4.4, one can easily realise that the sharp fall in the CCF should be noticed even for objects containing only $\sim 10^{13}\ M_\odot$ at $r < r_{\rho=200\rho_c}$ -thick galaxies to give an example-.

Navarro-Frenk-White Profile (NFW)

The density profile of the Navarro-Frenk-White profile was developed from N-body simulations by Navarro, Frenk and White as presented in their paper of 1997 [34]. Their model is a density profile with two[48] free parameters (concentration C and scale radius r_s) and is scaled by the critical density of the universe at the redshift the object is found. In equation (4.6) the density function for the NFW profile is shown. It can be fully described[49] by the mass and the convergence.

$$\rho_{\rm NFW}(r; r_s, \rho_s) = \frac{\delta_c\ \rho_{\rm crit}(z)}{(r/r_s)\left(1 + r/r_s\right)^2}\ , \quad \begin{cases} \delta_c = \frac{200}{3}\frac{C^3}{\ln(1+C) - C/(1+C)} \\ \rho_{\rm crit}(z) = \frac{3H^2(z)}{8\pi G} \end{cases} \tag{4.6}$$

The convergence is then found to be

$$\kappa_{\rm NFW}(\theta) = \frac{2r_s\delta_c\ \rho_{\rm crit}(z)}{\Sigma_{\rm crit}} f(\theta/\theta_s)\ , \quad f(x) = \begin{cases} \frac{1}{x^2-1} + \frac{\operatorname{arccosh}(1/x)}{(1-x^2)^{3/2}} & \text{for } x < 1 \\ 1/3 & \text{for } x = 1 \\ \frac{1}{x^2-1} - \frac{\arccos(1/x)}{(x^2-1)^{3/2}} & \text{for } x > 1 \end{cases} \tag{4.7}$$

The critical density is calculated from equation (2.22), the scale angle is obtained as $\theta_s \equiv r_s/D_d$. A fast way to get to the magnification is writing it as

$$\mu(\theta) = \frac{1}{1 - \bar{\kappa}(\theta)} \frac{1}{1 + \bar{\kappa}(\theta) - 2\kappa(\theta)} \tag{4.8}$$

[48] In appendix A, results by Mandelbaum et al. 2008 [35] show how weak lensing prefers some relation between C and M_{200} (alternatively M and r_s as explained in that appendix as well).

[49] r_s is usually taken as a compound parameter since the virial mass is preferred over it. Further discussion on these parameters is contained in appendix A.

where $\bar{\kappa}$ is the mean of κ. It can be expressed as

$$\bar{\kappa}_{\rm NFW}(\theta) = \kappa_{\rm NFW}(\theta)\frac{h(\theta/\theta_s)}{f(\theta/\theta_s)} \ , \quad h(x) = \begin{cases} \frac{2}{x^2}\left(\frac{\operatorname{arccosh}(1/x)}{(1-x^2)^{1/2}} + \log\left(\frac{x}{2}\right)\right) & \text{for } x < 1 \\ 2\left(1 - \log\left(2\right)\right) & \text{for } x = 1 \\ \frac{2}{x^2}\left(\frac{\arccos(1/x)}{(x^2-1)^{1/2}} + \log\left(\frac{x}{2}\right)\right) & \text{for } x > 1 \end{cases} \tag{4.9}$$

One big difference between both profiles is the double divergence-peak in the caustic region of the NFW profile, caused by the zeroes in the denominator of the two factors in the magnification equation (4.8). Concerning the steep fall in the CCF in the demagnification region, it is no different from that of the SIS case, but it happens at much shorter distances. One would expect that a greater resolution, which would be achieved if the CCF had sensitivity in the light-red shaded region -see again figure 4.4-, makes the demagnification region noticeable. Moreover, there is no physical requirement for it to be otherwise. Still, BCGs or smaller galaxies within the cluster[50] could spoil the event. For this reason, the effect of a change in the scale of pixels (e.g. 1 px = 1 arcsec to 1 px = 0.1 arcsec) may have on the good fit of the theoretical CCF to the observed (simulated) data will be inspected. In the future, the stacking working region, marked as the red shaded regions in the above figures, will be named ROI (for region of interest). It does not mean that CCF cannot be studied at greater distance or it is less interesting, indeed GN14, GN17 and BON19 address at some point the second halo model seen at arcmin-order distances, where extreme weak lensing occurs. In any case, one of the conclusions of BON19 was that stacking works well in the weak lensing region where μ is not extremely close to 1, so we will limit the work to that region.

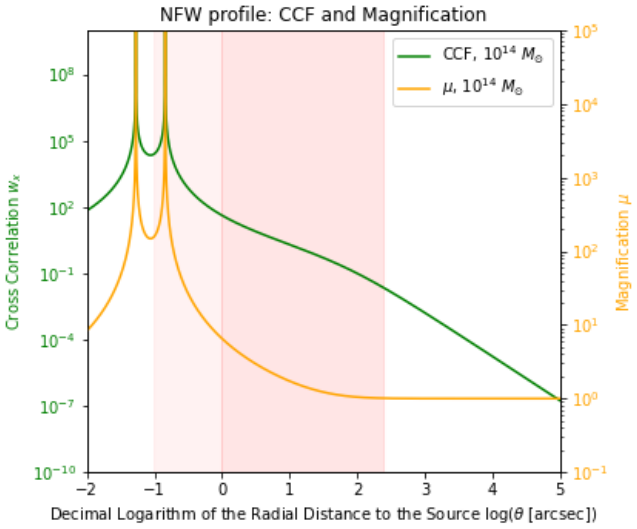

Figure 4.6: CCF (green) and magnification (yellow) functions for the intermediate case of 10^{14} $M_\odot$.

When it comes to one halo model being preferred over the other one, clearly FER22 showed that the NFW profile for the inner term (hypothesised as the BCG) returned overall values of mass and concentration in accordance to preexisting data from catalogue. For that reason, our main focus when we tackle double deck CCFs in section 6 will be through the simulation of

[50]Note that we are talking about clusters since only the 10^{15} $M_\odot$ case would produce a demagnification fall in that region.

double NFW profiles. In section 5 though, where we put the simulator into test, both profiles will be used.

Apart from the CCF, in figures 4.5 and 4.6 the magnification function was drawn in order to show that in the ROI μ is not asymptotically 1 yet -extreme weak lensing would happen at $\gtrsim 100-1000$ arcsec in the figures above-. *Weak lensing*, understood as the region where observed fluxes do no more than double intrinsic fluxes, occurs in the centre of the ROI. In addition, *strong lensing*, understood as μ factors well above 2, should also be appreciated at lower separations; especially with more massive deflectors. In general, risking not to be extremely accurate, one can draw a relation between the caustic region in the CCF and magnification profiles and the strong lensing effect. Despite this, source counting is an inefficient method to reproduce, from observational data, the caustics in the CCF and μ. This can be seen before performing any simulation, and its nature is purely statistical

$$w_{x,\,\mathrm{Stack}} = \frac{DD(\theta)}{RR(\theta)} - 1 \leq \frac{N(\theta)}{RR(\theta)} - 1 \tag{4.10}$$

As will be seen with our simulation and has already been shown in the bottom panel of figure 3.2, the $RR(\theta)$ distribution is highly isotropic with θ. In case $N(\theta)$ -the total number of sources simulated in the area $\theta \pm \delta\theta$- and $RR(\theta)$ are proportional one to each other[51], then the observed CCF plateaus at

$$w_{x,\,\mathrm{Plateau}} = \frac{N(\theta)}{RR(\theta)} - 1 = \frac{1}{c} - 1 \tag{4.11}$$

where we have named c the proportionality constant. When we introduce the function that assigns random fluxes to the simulated sources, that constant will represent the average number of sources above a certain detection flux S_{lim}. In the real world, however, we have no access to the total number of sources. Simulated functions for the flux as that one we have mentioned do only reproduce the knowledge of the -limited- background sources we have.

Indeed, when we conduct the very preliminary results in our CCF-simulator in the Toy Model section, we will have chosen some values for the flux limits in the flux simulator function. However, from a physical point of view, we cannot know how many background-type sources with fluxes below the detection limit exist. **Namely, $N(\theta)$ is completely unknown to us**. The only thing we can do is guessing the range of intrinsic fluxes that should be given to our

[51] This occurs when the amount of data available is big enough, so that statistical fluctuations are negligible. The size of the annular regions we use to count the sources is also important in this respect.

simulated sample of sources so that the (observed) simulated CCF resembles the (observed) real one. Comparing with the total number of sources observed in other studies (e.g. FER22) for given deflector masses -knowing the richness bin in which we are performing our study- and concentrations is a way to do so. When we study the behaviour of the plateau with our simulation, we aim to show that it is independent of the number of sources simulated, following the hypothesis that it only depends on the type of sources used.

The fact that the plateau will strongly depend on the properties of the sources used as background sample is not a trivial issue, though. Particularly, the function that will be used to simulate the intrinsic flux of those sources has to be bounded from above and below. The upper limits are somewhat easier to set: it is enough to know the maximum flux received from a non magnified background source of that type. It will be set all throughout the work at 100 Jy. The lower limit is, on the other hand, somewhat harder to define.

To give an example, the paper from Papovich et al. from 2007 [36] (PAP07) worked to study the infrared properties of high-redshift galaxies, which match -or could match- the type of background sources we use. They used photometric bands and therefrom calculated fluxes from the *Spitzer Space Telescope*. Although some bands are somewhat different from those used by the PACS and SPIRE instruments -at least in their peak values-, at 70 μm -shared by PACS (see figure 4.1)- show average flux densities between 0.88 and 1.5 mJy. That is, sources at even 0.1 mJy (or 10^{-4} Jy) should be considered to produce a comprehensive analysis with a realistic simulation of background sources. This would have the effect of changing the constant c in equation (4.11) for a function of the intrinsic flux of the SMGs, $c(S)$. We refer to section 5.2 for the very first analysis along that line, where we show the evolution of the plateau limit of the observed CCFs with respect to the lower limit of the flux generator. When it comes to assess the distribution of fluxes, the generator is assumed to produce reliable proportions at the simulated ranges of fluxes.

The acknowledgement that the plateau of the CCFs should be addressed could be driven as well from something else. The bottom panel of figure 3.3 and figures 3.5 and 3.4 already show a plateau at low θ, and we know that it is a strong lensing region according to what BON19 concluded in respect to the bad fit of the weak lensing approximated CCF (grey dots in the first figure of those mentioned). Neither do we see the caustics in the CCFs they used to fit the data trend. In their case, for the combination of masses and profiles used, the caustics fall outside the angular scale covered by the data. With our simulator, we will check the existence

of that plateau through a piecewise function -built up from experimental knowledge- and then we are going to perfom a smoothing once the plateau is set.

5 Simulator Development and Toy Model

The programming language of *phython* will be used from this point onwards -it was also used to create self-made figures such as 2.1 or those of section 4.3-. Some libraries of functions were provided by the supervisors -some of those and self-developed functions will be presented in appendix B- to perform some calculations like the magnification function or the radial analysis before computing the observed[52] CCF. All throughout this section and the following one, the number of sources used will play a major role. Unless the opposite is said, when we say that 10^X sources have been simulated, we refer to that number of sources being given a random intrinsic flux -which can be or not enough to surpass the detection limit either before or after the magnification is applied-; sometimes it will be useful to represent a certain number of sources being represented in the maps of counts (i.e. passing the detection limit after being magnified, as in figure 5.14), but if that is the case, it will be explicitly commented.

This section is divided into two parts. In the first part we aim to see that the different parts of the magnification functions can be seen in a map of counts where sources with enough flux are plotted. The steps that have been followed in those representations are the ones detailed in the following list:

(i) **One thousand** sources were distributed randomly (e.g. a pair of random coordinates were given) in a plot.

(ii) **Each** of those sources **was assigned a random flux**, first distributed from a normal distribution averaged in 30 mJy (the flux detection limit), and then following a distribution that resembles the flux distribution[53] of SMGs at 350 μm.

(iii) If a source surpasses the flux limit of detection, it is shown in those plots where non magnified sources are represented (e.g. figure 5.2 as blue dots).

(iv) We apply the magnification function to the intrinsic fluxes, those with resulting fluxes surpassing that limit are shown in the corresponding plots (e.g. NFW-magnified sources as yellow dots and SIS-magnified sources as pink dots in figures 5.1, 5.3 and 5.7).

- The foreground source is always the same at this point. Namely, out of the physical properties that enter afterwards as variables of the magnification functions, the

[52]For the remaining sections, ***observed CCF(s)*** refers to CCFs simulated by us; while if any CCF from previous papers appears, it will be referred to as ***observed CCF(s) from [reference]***.

[53]Code 1 was used to produce some random fluxes in the first part of the Toy Model and always from then onwards.

mass[54], redshift[55], concentration -if working with the NFW profile- and cosmological parameters are set fixed.

- Note that since the simulator works with the stacking technique, the position of the foreground source is irrelevant.

The availability of options and studies to undergo in this first part can be huge. We have restricted ourselves to what might be essential to understand well all the work that is done with the CCFs in section 5.2 and beyond, which is the main interest of this work. So, as a summary, we have shown figures that help to understand the effect of magnification functions in the maps of counts, that is, the visual introduction to the effect of **magnification bias**. In this first part the three mass cases introduced at the beginning of section 4.3 will be treated independently. We remind that 10^{13} $M_\odot$ is a mass order related to **thick galaxies**, what would be expected as well for a BCG in a cluster and its attached halo. 10^{14} $M_\odot$ is a **central value**, giving an idea of the CCF and magnification produced by an **average cluster**. Finally, 10^{15} $M_\odot$ is a perfect value to set an **upper limit**, a mass order expected for **thick clusters** at $z_{\text{fore}} \sim 0$. Each case will be profoundly studied and results regarding the description of each zone of the magnification profiles (e.g. strong lensing, weak lensing and -if applicable- demagnification) will be obtained. Meaningful representations accounting for the effect of magnification with respect to the random -non magnified- case will be shown.

Once this first stage is clear and thoroughly exploited, we will move on to the general model of the simulator, which is focused on the observed cross-correlation functions (CCFs) and the information that can be obtained from them. CCFs are built from maps of counts that, at this point, will be replaced by matrices of counts, where pixels accounting for an area on the celestial sphere around the deflectors are represented by the elements of the matrix. Indeed, this photographic experimental technique is vastly used by observational astronomers[56]. Our idea is similar to that one, although what we record is not photons or deposited energy in a camera but number counts.

In the following lines we are going to explain the methodology step by step for creating an observed CCF, as well as some ideas of how the ones we obtain are going to be fitted by a

[54]See the discussion in the paragraph following this enumeration about the masses used. It was already introduced at the beginning of the previous subsection, though.

[55]There is a unit in section 5.2 dedicated to explaining the effect of distributions of redshift applied to the sources -both background and foreground-. The effect of slightly variable masses of the deflectors is considered in section 6.1 once we are with complex profiles results.

[56]For example, when measuring photometric fluxes from stars or transient events, the recorded light in each pixel -which depends on the exposure time- is represented by a number, and the whole field by a matrix.

theoretical model:

(i) A map of pixels is created. The radial scale is set up between 0 and 250 arcsec, with a matrix of size $n = 500$ px $\times$ $n = 500$ px in the stardard case, where 1 px = 1 arcsec.

- Magnification is calculated at the centre of each pixel and that mean value is given to each of the n^2 pixels. It is done in this way so that magnification has to be calculated only once. The reason behind this is the fact that computation time becomes intractable[57] if magnification is calculated in the particular position of each source. A copy of the magnification map is saved.
- The minimum θ value for each map of size $n \times n$ is $500/2n$, with 500 being the side of the squared 500 arcsec $\times$ 500 arcsec fixed region analysed. We are not going to change the size of the celestial sphere region. This means that any change in the size of the matrix of pixels will only change the size of each pixel. Following this, a map of 500-side pixels has θ_{min} -or resolution- of 0.5 arcsec, but a map of 5000-side pixels has a resolution of 0.05 arcsec. This difference is of major relevance since, as seen in figure 4.4, the left-hand side of the ROI could get to cover the demagnification fall of the CCF if we performed the simulation with the smallest possible resolution.

(ii) Random position of sources was calculated and assigned for each of the 10^6 simulated sources -unless another amount is specified at some point-, an then they were given a random flux from the *realistic*[58] distribution. Unless the opposite is said, sources are going to be described by a minimum flux level of 10 mJy. The upper limit will always be fixed at 100 Jy. Functions can be consulted in the appendix B. For the generation of random fluxes we refer to code 1. Then for the creation of the maps of counts codes 3, 4 and 5 served to that end depending on what was intended to be studied.

- A source with an intrinsic flux overcoming the detection limit is assigned as a count (e.g. +1) in a new map called *random*. From this map the counts $RR(\theta)$ will be obtained.
- If the intrinsic flux of the source, multiplied by the magnification calculated at the pixel of the source overcomes the detection limit, a count (e.g. +1) is added to a new map called *magnified*. From this map of counts $DD(\theta)$ will be obtained.

[57] Particularised magnifications are calculated in the unit about the effect of redshift in section 5.2. Also in section 6.1, when some variability over the mass of the deflectors is considered, magnification will have to be calculated for each source in particular.

[58] Check the flux functions in appendix B.

(iii) Optionally, a Gaussian smoothing can be applied to the maps to account for the uncertainty in the location of the sources. This aims to reproduce the maps of figure 3.2. It is also useful in order to eliminate possible zeroes in $DD(\theta)$ when the DP estimator is computed. Once the smoothing is introduced in the unit dedicated to it in section 5.2, it will be used in the rest of the calculations. Particularly in the whole of section 6.

(iv) A Jackknife analysis will be performed in annular regions calculated with a logarithmic scale. Each of the points in the observed simulated CCF trends has as θ coordinate the mean value of each ring.

(v) The CCF is computed with the Davis-Peebles estimator (DP)

(vi) The fit is performed with a theoretical CCF. The virial mass parameter will be loosened all throughout the second subsection, since it is common to both profiles (SIS and NFW) and is assessed by BON19 and FER22 regarding the dark matter profiles. The concentration C parameter will be left set at 4.0 -as it is[59] an average value within the binned analysis by FER22- unless the contrary is said. Particularly, at the end of this section a mass and concentration distribution will be allowed for the deflectors, and a common $[M, C]$ curve_fit analysis will be performed. Regarding the algorithm for the fit, both the *curve_fit* function from the *scipy.stats* library and a self-made least squares method were used, we refer to codes 8, 9, 10, 11, 12 and 13. Note that:

- If the raw CCF calculated from the theoretical profiles is used (figure 4.4), the caustic region cannot be used to perform the fit.
- If the piecewise or the smoothed piecewise CCFs are used instead, a global fit can be carried out.

Firstly, a computation of the observed CCFs for the three mass cases and the two profiles will be made. Also, related features as the change of tendency in the CCFs as a result of the plateau region and the discussion held at the end of section 4.3 about the effect of the range of fluxes simulated will be shown and studied. Finally, the more complex theoretical fits of the piecewise function and the smoothed CCFs will be conducted. Apart from the detailed steps explained above, appendix B shows some of the code lines an functions used. We refer to them for a deeper understanding of the computing methodology used.

[59]Beyond these references that we use all throughout this work, White's paper from 2001 [37] comments that 5.0 is a reference value for the NFW concentration of a cluster halo.

5.1 Toy Model (I): Magnification and Source Counts

The magnification theoretical profiles and the effect they have in me maps of counts will be presented in a growing-mass order. Some different features and figures will be added and commented in each case, but figures 5.1, 5.3 and 5.7 are central in the structure and are a common start point in all of them. In all those figures, the dotted panels (at the right) represent the sources that get magnified[60] by each profile. Empty pink dots represent sources magnified by the SIS profile alone. Filled yellow dots represent sources magnified by the NFW profile alone. Dots with those two colours represent sources magnified by both profiles. In the panels at the left the magnification function is presented for both profiles in the ROI.

Thick Galaxy or BCG: 10^{13} $M_{\odot}$

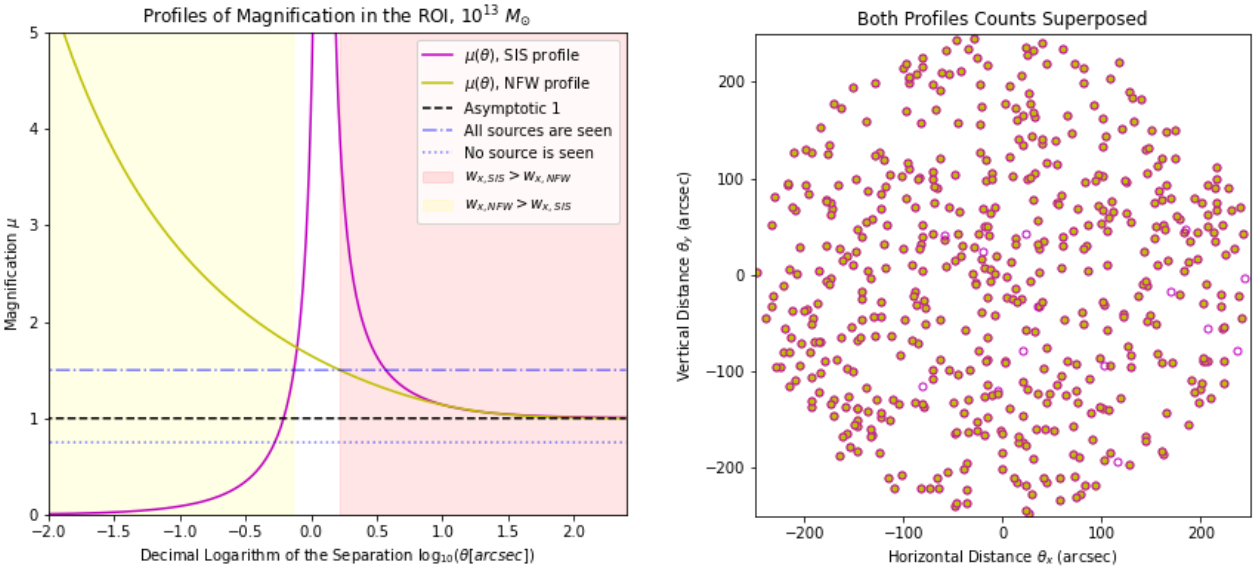

Figure 5.1: Magnification profiles for a source of mass 10^{13} $M_{\odot}$ (left). Shaded regions represent the parts in which one profile effectively magnifies more sources than the other. Horizontal lines represent the magnification that separates regions where all sources are seen, some are seen (normal weak lensing) and none is seen. At the right, the map of 1000 sources randomly distributed with the distance (or separation) from the deflector. Empty pink dots represent source that are effectively magnified above the detection limit by the SIS profile but not the NFW profile -there are a few of them-. Yellow filled dots represent the opposite -non distinguishable in this map-. Combined dots of both colours represent sources effectively magnified by both profiles.

Both the SIS profile and the NFW profile show the same behaviour above ~ 4 arcsec. Though as seen in the right panel of figure 5.1, where we have simulated a thousand sources and intrinsic fluxes ranging between 20 mJy and 40 mJy, seemingly the SIS magnification is slightly above

[60] In this context *magnified* is an abbreviated form to say *effective magnified above the flux detection limit,* 30 *mJy.* This value is chosen in accordance to the latest flux detection limits commented in BON19 and FER22.

the NFW one: there are some sources that are not magnified enough by the NFW profile but they are by the SIS profile (empty pink dots). This would be quite natural if it happened, according to what we can see in the left panel of the figure, in between ~ 2 and ~ 10 arcsec. There, the SIS profile goes well above the NFW, falling bellow the blue dashed-dotted line that represents the limit between the strong[61] and weak lensing regions. However, as seen in the yuxtaposed panel, the trend is quite general at all distances. It could be well explained by the fact that the distribution of sources is radial with distance. Annular regions at greater $\theta \pm \delta\theta$ have larger areas, and therefore, more sources. Even if the difference between μ_{SIS} and μ_{NFW} is not that big at greater θ, the greater amount of sources overall can amplify the effect.

Regarding demagnification, the effect could be seen for any source falling bellow ~ 0.5 to ~ 0.7 arcsec. However, there is little chance of this happening in a region ($\theta < 0.7$ arcsec) the size of one ~ 130000th of the total region. In other words, one should display ~ 130000 sources to have a non negligible probability of seeing a filled yellow dot alone: a source magnified above 30 mJy by the NFW profile but suppressed by the SIS.

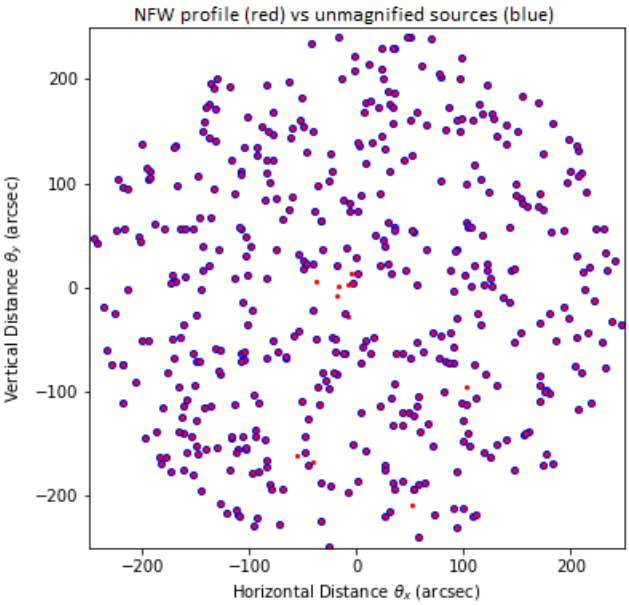

Figure 5.2: Sources overcoming the detection limit without having been magnified (blue dots) and after magnification is applied (red dots). There is a consistent overconcentration of sources towards the central region.

Another interesting feature to comment here is the quite important concentration of figures towards the centre of the figure. The effect of magnification is responsible for this, and happens equally for both profiles, as can be seen in figure 5.2, where we have simulated sources with random intrinsic fluxes overcoming the detection limit (blue dots) and magnified sources with total fluxes surpassing it (red dots). However, some rogue red dots can be found in further regions, which is somewhat expectable. Sources are given a random flux between 20 and 40 mJy, so any of it which comes close enough from below to the limit value of 30 mJy in outer regions, can jump above just with a tiny magnification increase. Indeed, the intrinsic flux of sources being magnified in the region $\theta > 10$ arcsec was tested with the simulator. The results consistently showed it between 28 and

[61] This is not extremely accurate but has to be understood as a way to define the region where all sources with intrinsic fluxes within certain boundaries are magnified above the detection limit and the standard region where some sources are effectively magnified and others do not.

30 mJy.

Average Cluster: $10^{14}\ M_{\odot}$

Results in the intermediate mass case are in general similar to what was seen in the lower mass case. The displacement of the magnification profiles towards the right, though, should allow to sight randomly some full yellow dot at the centre of the right panel of figure 5.3. With 10000 random distributed sources it should happen that at least one falls in the demagnification region of the SIS profile. That number of sources is, nevertheless, hard to represent in a way the figure is easy to understand.

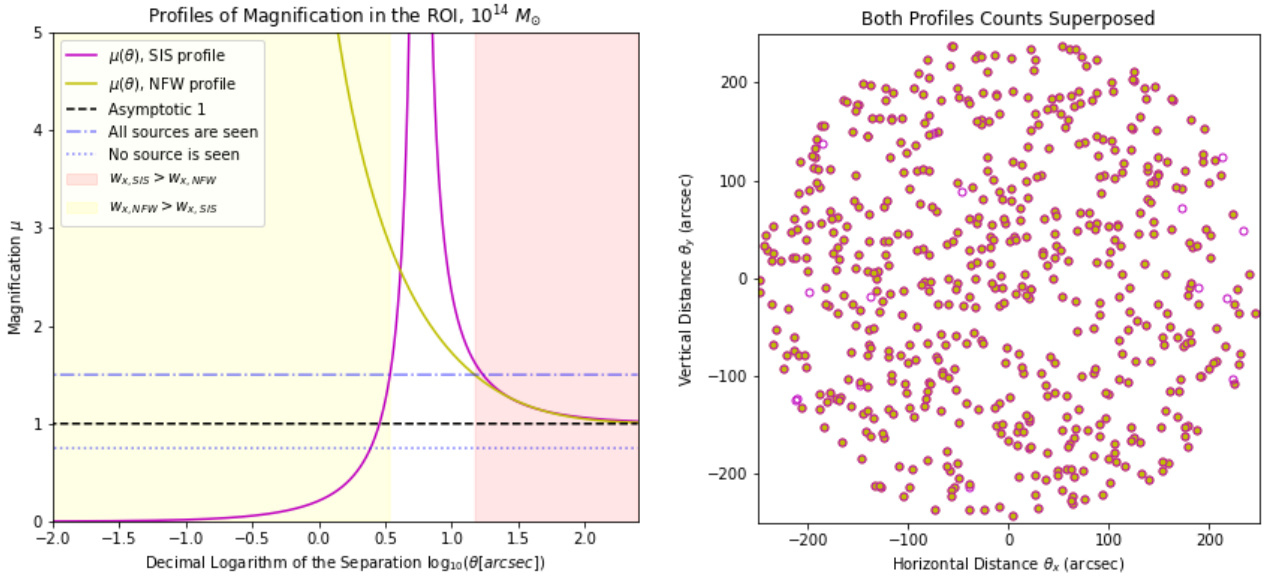

Figure 5.3: Same representation as in figure 5.1 but with a mass for the deflector of $10^{14}\ M_{\odot}$.

Another interesting change from what happened in the $10^{13}\ M_{\odot}$ case has to do with the move of the right hand tails of the magnification functions towards the right as well. In this case, both profiles pass from the *strong lensing* regime to the *weak lensing* one quite at the same time: the profiles cross the blue dash and dotted horizontal line at close θs, and overall at a greater θ than they did in the previous case. This translates to the right-hand side panel in the form of empty pink dots falling at greater distances from the centre.

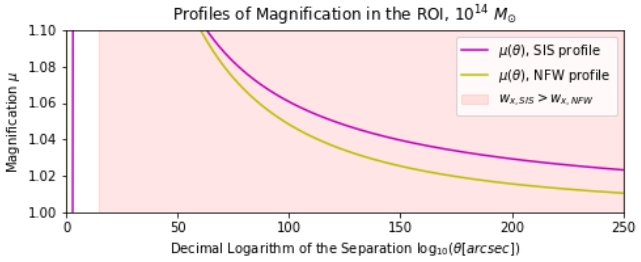

Figure 5.4: Linear representation of the left panel of figure 5.3 zooming in the $1.0-1.1$ range of magnification.

Following the last few lines of the last paragraph talking about figure 5.2 it would be wise to ask whether the sources that get magnified only by the SIS profile at greater distances do

so because their intrinsic fluxes are close to the 30 mJy limit. Indeed, what is found is in this line. The lowest intrinsic flux obtained from only-SIS magnified sources after several iterations at $\theta > 200$ arcsec is 29.4091, for which the difference between the magnification of both profiles needs to be, at much, of only ~ 0.02. Obviously, this would be something hard to see from the magnification profiles in the left panel alone. To help with that, figure 5.4 represents in a linear scale the magnification profiles with distance, allowing the magnification levels between 1.0 and 1.1. It appears clear there that the difference between the SIS profile and the NFW profile above ~ 70 arcsec can be enough to produce in the SIS-magnified case a jump of the flux over 30 mJy.

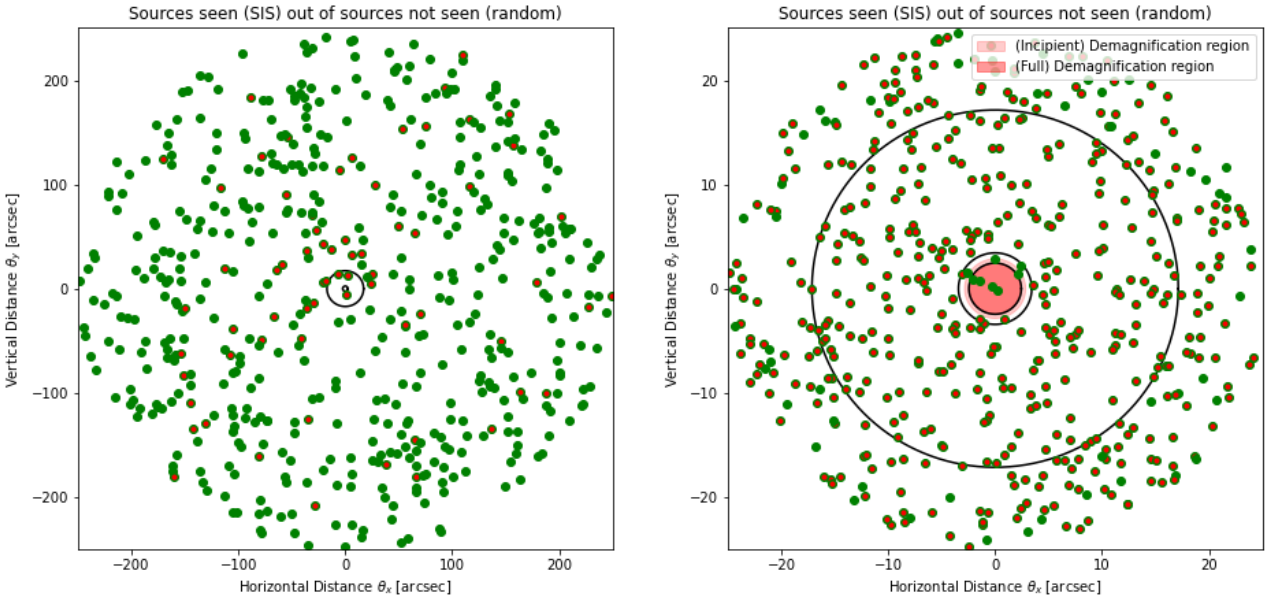

Figure 5.5: 1000 sources distributed along a circular region of radius 250 arcsec (left) and 25 arcsec (right). Red shaded regions at the right panel represent the full demagnification region. Concentric circumferences divide the region in 4 areas, from inner to outer: (i) full magnification, (ii) inner weak lensing area, (iii) strong lensing area and (iv) general weak lensing.

What happens with the demagnification region is also important and has to be addressed in detail. When we simulated 1000 sources in the circular region of radius 250 arcsec, it was hard to see one source that fell in the inner ~ 2.5 arcsec. If we chose to distribute the 1000 sources in a circular region of radius 25 arcsec instead, to keep the statistics and proportionality in the original ROI (250 arcsec) we should have simulated a total of 100000 (10^5) sources. Indeed this is not such a great number when we perform the analysis of the CCF, since there the computations run acceptably fast up to 10^7 or 10^8 sources. Just to give an idea of the relevance of these simulations, FER22 used ~ 20000 background sources. This is enough to allow for some sources randomly falling in the demagnification region, provided the SIS profile was an accurate

description of the dark matter profile of the deflectors. Figure 5.5 shows the importance of the number of sources used in order to fully appreciate every region of the magnification function. In the left panel 1000 sources were distributed randomly in a circular area of radius 250 arcsec, 25 arcsec in the right panel. Green dots represent sources with intrinsic fluxes below the limit at 30 mJy; from those, red dots represent the ones which, thanks to the magnification provided by the SIS profile, overcome the limit. Figure 5.5 is quite useful not only to see the demagnification region, but as well the overall shape of magnification at larger scales. The strong lensing region and the close weak lensing one following it cause the greater number of sources brought above the detection limit. The left panel represents this quite well; there the circumferences of the right panel are also ploted, in order to give a view of the small size of the strong lensing and demagnification regions.

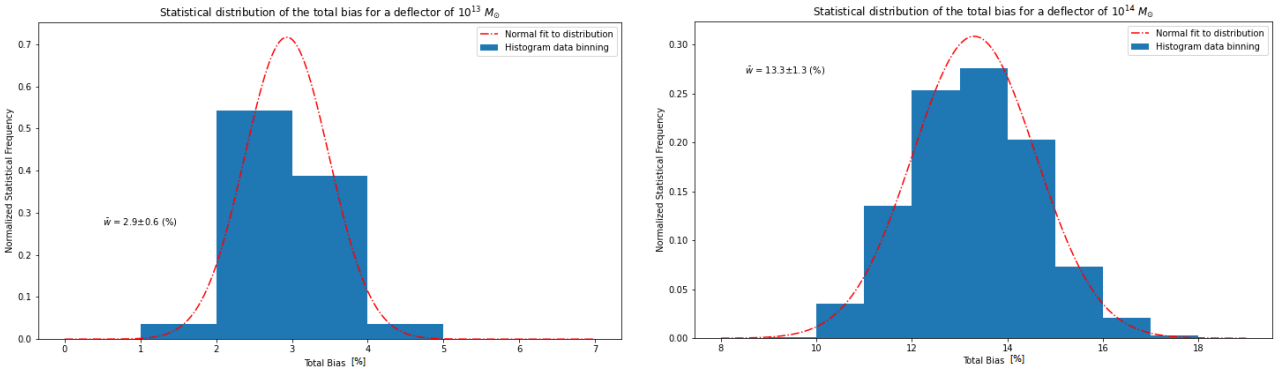

Figure 5.6: Average bias calculated for the last two mass cases after 1000 iterations of the algorithm.

Overall, the 10^{14} $M_\odot$ case magnifies more sources than the 10^{13} $M_\odot$; which is quite natural since strong lensing covers a wider region in that case. To give a quantity of the overall increase -should be thought as an averaged magnification bias or CCF- figure 5.6 is ploted. Both panels represent the distribution of average magnification bias obtained from the simulated data. The values are computed following the Davis-Peebles estimator but as an average over the total RR and DD data. This means no radial analysis is performed, but sources are counted as they are ploted in each case. Before finally closing our example of 10^{14} $M_\odot$, a note should be given on its relevance as the model to rely on. The foreground sources studied as deflectors by BON19 and FER22 appeared in this mass range. From catalogue the masses of the latter ranged between 0.7 to 6.4 in orders of 10^{14} $M_\odot$ for the total mass terms. Outer halo terms represented up to an 80% of the mass. Moreover, BON19 found results in agreement with this; an estimation of $M_{200} = 1.0^{+0.4}_{-0.2} \times 10^{14}$ $M_\odot$ when constraining mass and concentration parameters altogether using the NFW profile as a ruler.

Massive Clusters: $10^{15}\ M_{\odot}$

Figure 5.7 presents greater differences from the previous cases. In this extreme case, which aims to be an upper limit of the mass of clusters we will find, a SIS profile would cause a demagnification region observable in the inner region of the map. In the right panel of the figure we have plotted the two circumferences that were before displayed in the right panel of figure 5.4, adapted to the magnification profiles in this one case. From 100 arcsec onwards the behaviour is quite comparable to those observed in figures 5.1 and 5.3, though.

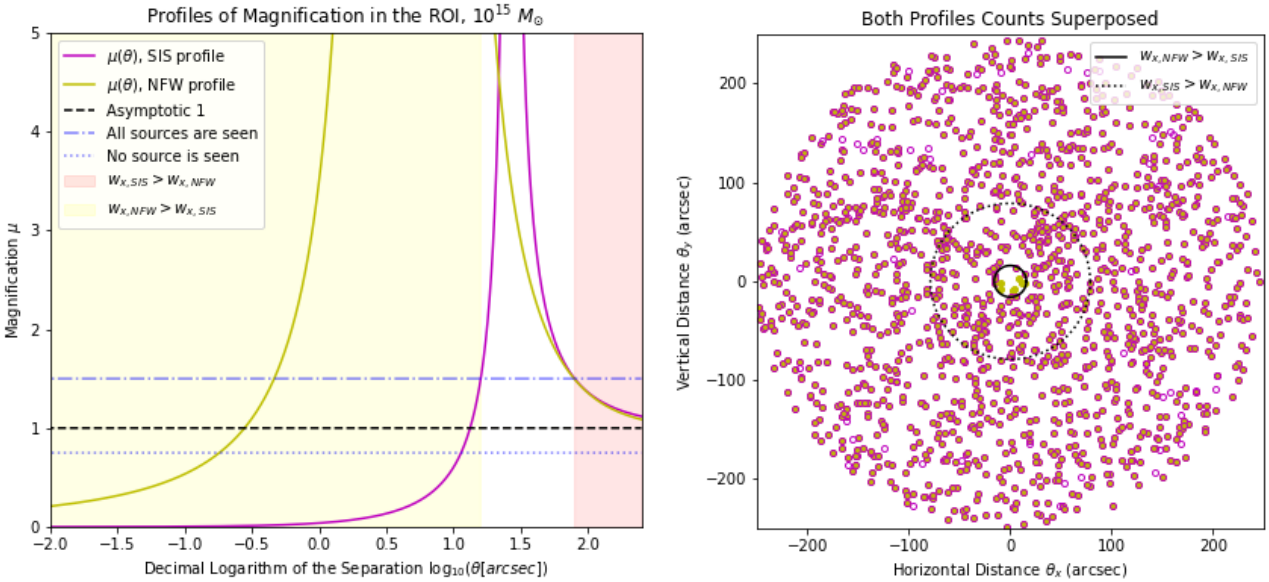

Figure 5.7: Same representation as in figure 5.1 but with a mass for the deflector of $10^{15}\ M_{\odot}$. Additionally, in the right panel, the rings of the right panel of figure 5.4 were incorporated in the right panel of this figure.

Regarding the left panel this is the first time that the NFW profile shows its demagnification part within the ROI. For this reason additional plots will be made similar to that of figure 5.5 so that, if possible, some -complete- absence of sources be seen. Possibly, it may be necessary that the amplified region gets much closer to the origin than in the previous case. This can be asserted just by comparing the separations (θ) at which the $10^{15}\ M_{\odot}$ NFW and the $10^{14}\ M_{\odot}$ SIS profiles cross the limit level for no source can be seen. Certainly, the ~ 0.2 arcsec requires the region of area $\sim \pi \cdot 0.2^2$ arcsec^2 to be big enough as to contain a few simulated sources.

If the simulator is able to produce enough sources in that region, it comes as obvious that staring at the magnification/CCF profiles (alike the left panels of figures 5.1, 5.3 or 5.7) or the maps of source counts (the right panels of those figures) is essentially the same. Again, this will only work well when the amount of sources that are simulated in each region of the magnification profiles is big enough. To keep in mind some numbers and an idea of the amount

of sources that would be needed to have at least 100 sources in the circular π arcsec^2 area -which means a radius of 1 arcsec-, since it represents a 1.6×10^{-6} fraction of the total area, 6.25×10^6 would be the number. This means that if we work with between 10^6 and 10^7 sources in our simulator, every region of the profiles -in the 10^{15} $M_\odot$ case- should be available for our CCF to keep track of it.

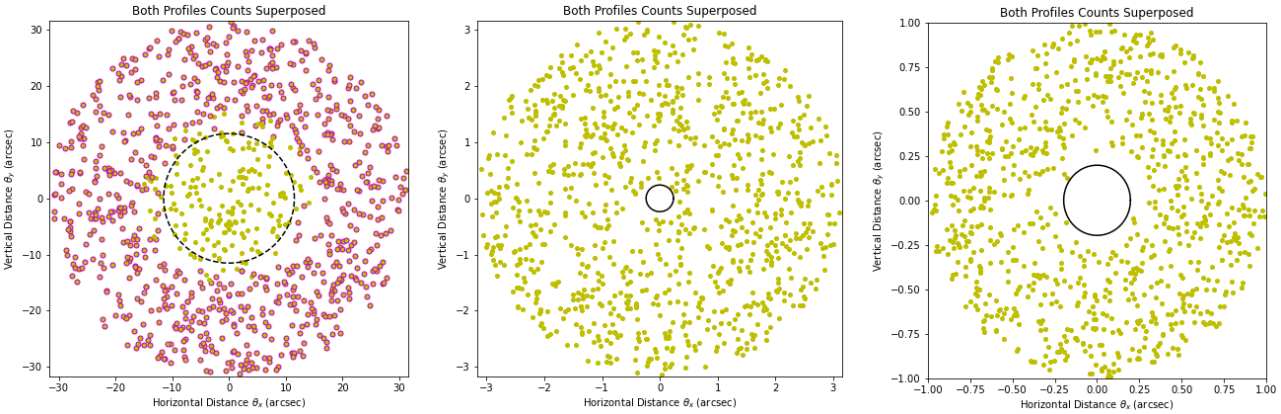

Figure 5.8: From left to right panels are distributed being maps of size $\{\log\theta_x \times \log\theta_y\} = \{(1.5, 1.5), (0.5, 0.5), (0.0, 0.0)\}$. 1000 sources were simulated in each case. In the left panel the dashed circumference represents the external limit to the area in which no source would be seen if the profile chosen was the SIS. In the central and right panels, the circumferences represent the limit to the area in which no source would be seen regardless of the chosen profile.

As a way to see this clear, we have performed an extra plot (figure 5.9) in which we show the number of sources needed in a circular area of radius 250 arcsec so as to produce at least 100 sources in the circular area placed inside a circumference of radius $\theta_{\rm inn}$. Note that $\theta_{\rm inn}$ is defined to be the region where demagnification causes a total absence of sources; however, we had simulated in figure 5.8 100 sources in areas at θ greater than $\theta_{\rm inn}$. For that reason, figure 5.9 will see greater values for the number of sources, in the $\theta_{\rm inn}$ interval of $[0.01, 1.0]$ arcsec, than those commented above. Therefore, one should see the number of sources from the black solid line as an upper limit.

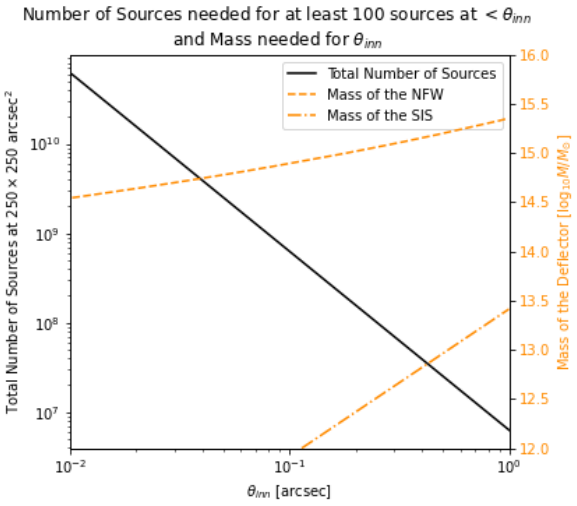

Figure 5.9: The black line represents the number of sources that is needed to have at least 100 sources simulated in the region below $\theta_{\rm inn}$. The orange lines represent the mass needed to take each profile to that $\theta_{\rm inn}$.

In this figure we have also computed the mass needed to produce a $\theta_{\rm inn}$ at those values. One conclusion that can be obtained from it is that the NFW profile would *move* to the right in the

plots of the magnification function faster with growing masses. This means that it would be possible that a seen cluster of $\sim 2-3\times10^{15}\ M_\odot$ had a greater demagnification region. Notably, before having reached a mass of $10^{16}\ M_\odot$ the NFW profile would show its inner demagnification region at ~ 10 arcsec (not shown in the figure). This is an important result for the heaviest clusters. It will be seen that $\theta_{\rm inn}$ is less relevant than the precision available on the location of sources and whether if the map of counts that will be used gets to separate sources that lay short distances apart. Particularly the magnitude order change from 0.5 arcsec resolution to 0.05 arcsec should play the major role in the identification of demagnification regions.

5.2 Toy Model (II): Cross-Correlation Functions

The cross-correlation function (CCF) is used as the observable that talks us into the existence of a magnification bias. Through it we aim to obtain information about parameters of the various models used; particularly the dark matter profiles presented in section 4.3. In the following lines we are going to explain the display of the map of counts and the fit with the theoretical CCFs.

As a first attempt to reproduce the fits performed in BON19 and FER22, we show figure 5.10, where upper panels represent NFW profiles and bottom panels SIS profiles of distributed dark matter in the halo, ordered from left to right in ascending value of mass. 10^6 sources were simulated in each case, with no smoothing applied on the map of counts. One aspect that should be left clear is that no algorithm is applied to separate the caustic region, which cannot be fitted to any theoretical model of CCF so far, from the weak lensing regions. Indeed, the plateau we had introduced when reviewing the work of BON19 is what we see in the $10^{15}\ M_\odot$ cases -possibly the SIS $10^{14}\ M_\odot$ one as well, but we lack resolution in the caustic region to assert this-. This means that some difference can be perceived between the trend of the observed CCF (black dots) and the theoretical fits in the strong lensing region. Apart from that, the $10^{14}\ M_\odot$ and $10^{15}\ M_\odot$ panels in the SIS case allow us to perform a fit of the inner weak lensing-demagnification region. Therefore, the total reproduced mass and its model was computed as the averaged -weighed taking into account uncertainties- value obtained from the upper and lower fits. In general, the readout of the mass can sometimes diverge from the input value.

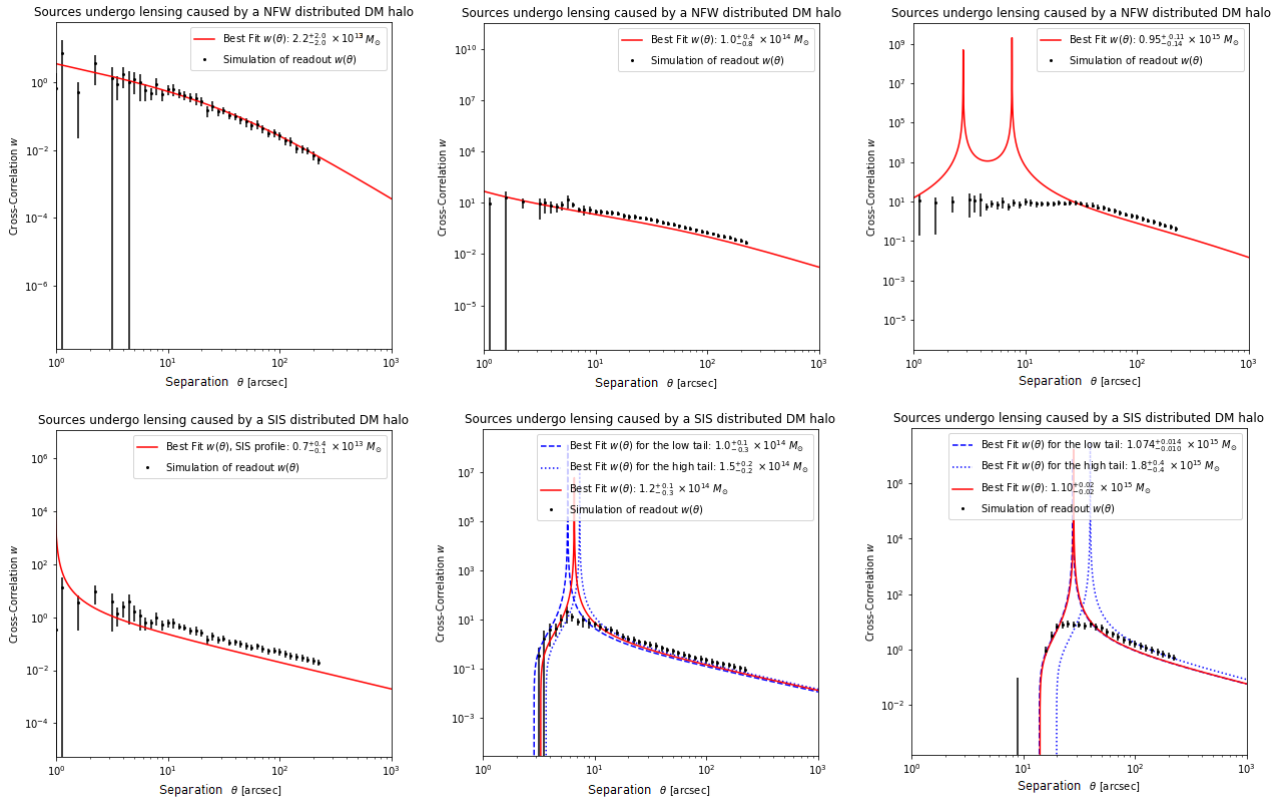

Figure 5.10: From left to right plots in ascending value of the mass of the deflector. Upper panels then represent NFW profiles while bottom panels represent SIS profiles. The fit through the theoretical CCFs is there performed at the right-hand side of the caustic (red line) and, when possible, at the left-hand side (blue-dotted line). Since we have used a 0.5 arcsec resolution, only the bigger mass SIS profiles show the demagnification region clearly.

Improving the Fit: Piecewise and Smoothed CCFs

The doubtful good fit to every point of the observed CCF data in some of the shown cases -namely the 10^{13} $M_\odot$ for the SIS case and the 10^{14} $M_\odot$ and 10^{15} $M_\odot$ for the NFW case- prompts us to create a solid algorithm to know where the separation of the different regions of the observed CCF happens, so that points *foreigner*[62] to each region are removed. Figure 5.11 shows how a differentiated analysis reproduces well the observed data. It was computed manually and, of course, our lin-

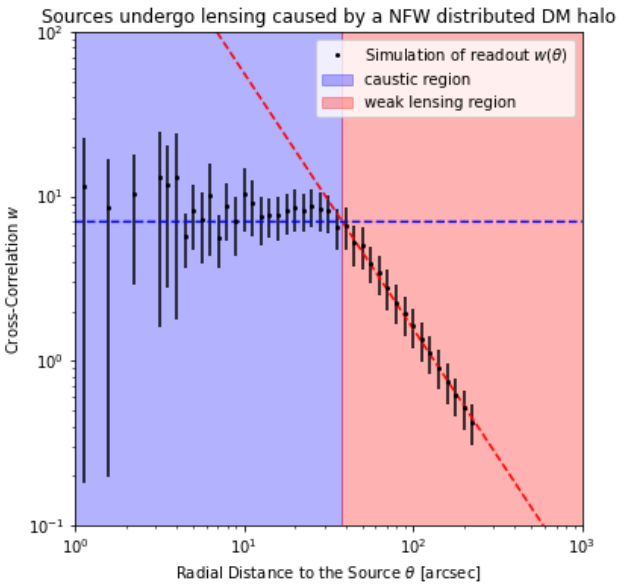

Figure 5.11: By-hand division of the observed CCF between the strong lensing and weak lensing regions in the 10^{15} $M_\odot$ NFW case.

[62]To be understood not as points that differ significantly from the trend but spoilers to the fit with the theoretical model because they fall in the plateau or have huge uncertainties.

ear[63] fit in the weak lensing region works well only coincidentally. Indeed, the 10^{13} $M_\odot$ and 10^{14} $M_\odot$ cases with NFW profile (upper-left panels of figure 5.10) show tendencies that can hardly be approximated by a linear order. Anyway, the theoretical CCF can be fitted in the weak lensing region, so we only need to solve the strong lensing issue.

Firstly, we will address the development of a piecewise function which combines a plateau in the strong lensing region with the theoretical CCFs in the weak lensing parts. To that end, it is necessary to have measured the value of $c \equiv c(S)$ from eq. (4.11) and assessed whether it evolves with the number of sources simulated. Once we know that the plateau remains mostly unaffected by the number of sources, the impact of the lower bound of the distributed intrinsic fluxes will be evaluated. The scope of that impact is yet unknown to us, and we have little clue of how much the plateau may change for lower limits of the flux generator. The result of that study will depend much on the shape of the distribution of sources the generator provides. The only thing we can guess so far is that the height of the plateau will rise -allowing us to see a greater portion of the theoretical CCF- with lower values of the lower bound. It would be something natural that less sources were simulated with intrinsic fluxes above 30 mJy, so that the average value of $\langle RR(\theta)\rangle$ would go down rendering a greater value of $N/\langle RR(\theta)\rangle$.

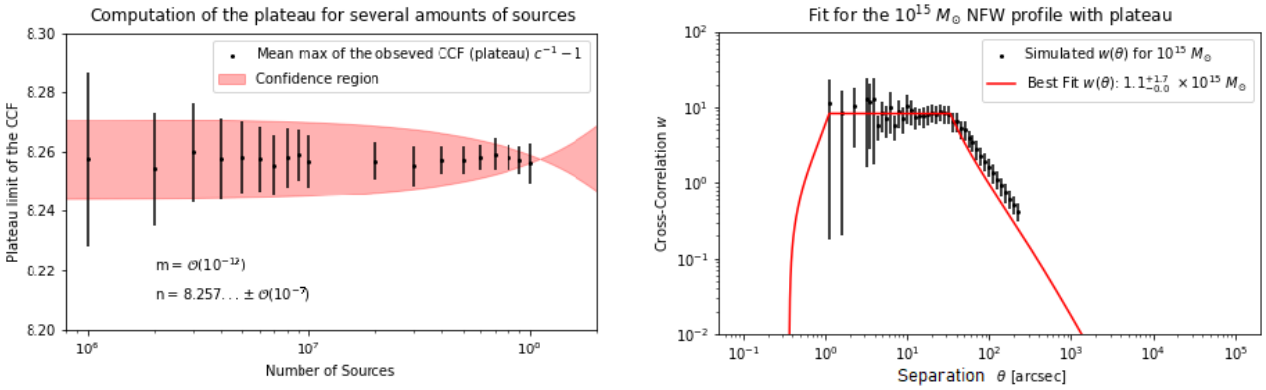

Figure 5.12: Left panel shows the value of the CCF at the plateau; directly calculated as indicated in eq. (4.11). The confidence region was calculated by performing a linear lift with the extreme values (e.g. data + uncertainties) of the trend. The right panel shows the result of applying a piecewise fit for the observed CCF of the 10^{15} $M_\odot$ NFW case (upper right panel in figure 5.10).

Having studied the behaviour of $N/\langle RR(\theta)\rangle - 1$ for different values of N we prove that $c \equiv c(S)$ is a constant that can only depend on the type of sources used and their intrinsic fluxes, as expected. The results are shown in the left panel of figure 5.12, pointing to the flux distribution for the background sources as the main cause behind the plateau behaviour shown. A linear

[63]The fit is linear in a logarithmic scale.

fit was attempted in order to exclude any possible evolution with the number of sources. The fit results include a first order dependency of order 10^{-12}, in comparison to an average value for the CCF value in the plateau of 8.257... with an uncertainty heavily suppressed as well $\sim \mathcal{O}(10^{-7})$.

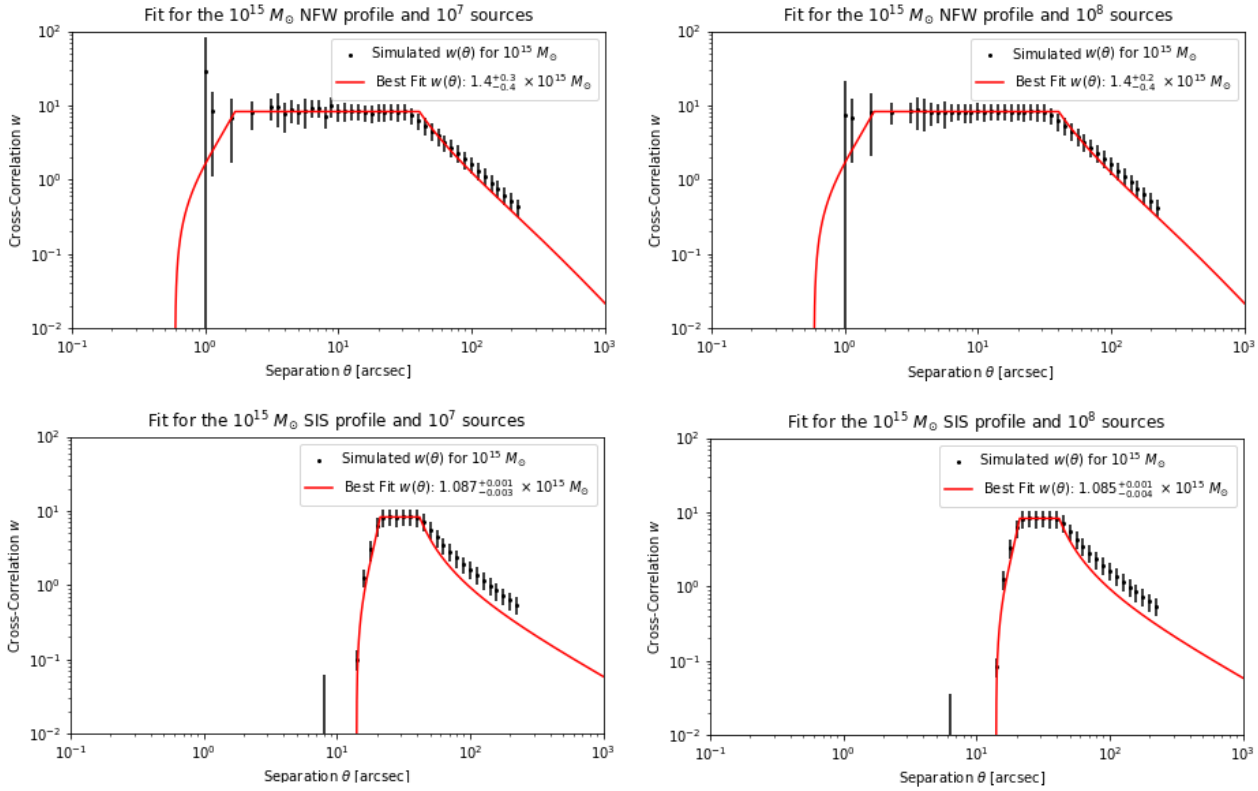

Figure 5.13: In the most massive cases the fit was performed for a greater number of sources (the panels at the left 10^7 sources and the panels at the right 10^8 sources). The plateau becomes less variable as the availability of sources increases. Linking to the results brought along with figure 5.12, the plateau remains constant at the same level; proving once again what was discussed above.

When the theoretical CCF is modified as a piecewise function that accounts for a plateau at a set[64] value of $w = 8.257$, a complete fit can be performed over the whole observed CCF trend. Unfortunately, the readout of the mass is not better than the one obtained by a fit of the by-hand chosen data that *belong*[65] to the weak lensing region, as shown in the upper right panel of figure 5.10. The modified theoretical CCF with the plateau gives back a value of $1.1 \times 10^{15}\ M_\odot$ when only the data trend is considered, the limits there presented $[\lesssim 1.1, 2.8]$ are obtained when the fit is performed with the extreme values of the uncertainty associated to each point of the observed CCF; all those values were obtained by performing a least squares

[64] We chose that value since it was the one obtained after the fit of the trend of the left panel.

[65] It should be reminded that the elements of the data trend that were classified as belonging to the weak lensing region did not follow any set or conventional algorithm for their choice.

method between the data trend and mass-spaced models of the theoretical CCF. When the *curve_fit* function from the catalogue of *scipy.optimize* is tried instead, it is able to provide a readout of the best fitting mass -which is a huge improvement in comparison to what we were able to do in the previous cases- and the uncertainty obtained for that parameter is surprisingly small, $\sim \mathcal{O}(10^{-5})$ in units of $10^{15}\ M_{\odot}$.

Fluctuations in the plateau region should be associated with anisotropies in small angular regions, as can be seen in the right panel of figure 5.12. It should be natural, though, that a greater number of sources resulted in a reduction of the variability due to the availability of more statistics to work with. Conversely, it is possible that a small number of sources helps fluctuations to grow.

The lower limit of flux used in the flux generator affects critically the CCF when one approaches the caustic region. It can be easily seen in figure 5.14, where the observed CCF tries to come closer to the theoretical function (in dashed lines). Notably no major difference between the observed CCFs is perceived at $\gtrsim 3$ arcsec. Figure 5.14 was simulated by changing the lower bound of the flux simulator[66] from 10 mJy to $\sim$ 5, 1, 0.5 and 0.1 mJy. The maps generator programme was run until 10^6 sources had surpassed the flux detection limit in the magnified case, which meant long computational times for the most extreme minimums of the flux generator ($10^{-4.0}$ and $10^{-3.3}$ Jy). According to the relation observed in infrared galaxies in PAP07, the fact that the observed average fluxes in that paper in 160 μm lie around $1-5$ mJy come to confirm that observed CCFs can easily exceed order 10^1 (as in the bottom panel of figure 3.4). Now, the number of simulated sources becomes critical, since only the $\log(S_{\text{lower bound}}) = -2.0, -2.3$ and -3.0 cases adjust well with the theoretical CCF + plateau, while the other two cases fail to get well fitted. Particularly, when performed until 10^4 and 10^5 magnified sources were simulated -see figure C.1 in appendix C- the fit got completely

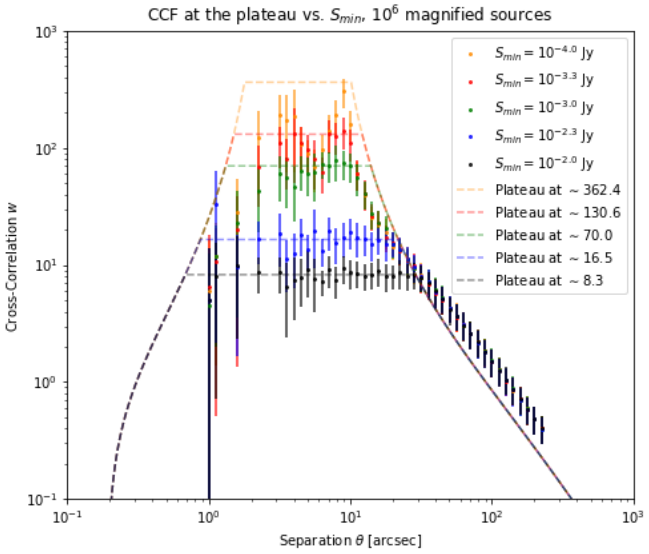

Figure 5.14: A $10^{15}\ M_{\odot}$ NFW profile was simulated, assigning background sources random fluxes from the flux generator but changing each time the lower bound. Coloured observed CCFs and their tendencies go from the standard (black) 10^{-2} Jy to (orange) 10^{-4} Jy in logarithmic steps.

[66] In the plot, these values of flux are expressed as powers of 10 in Jy.

lost due to the huge variability of the observed CCF in the plateau region. That would work as well as a hint of real observed CCFs failing to produce a solid readout of parameters at $\lesssim 1$ arcsec separations.

Numerical proof that $N/\langle RR(\theta)\rangle$ is a function of the minimum flux can be seen in figure 5.15. In the left panel of the figure the computation of $N/\langle RR\rangle - 1$ as a function of S_{min} is shown. Since we have no idea of how that function would behave, no analytical fit was tried; what is more, if a polynomial was to be tested, one of grade three or more would be needed to fit the data properly. In the right panel we have shown the (linear) normalised[67] number of background galaxies simulated with respect to the intrinsic flux given.

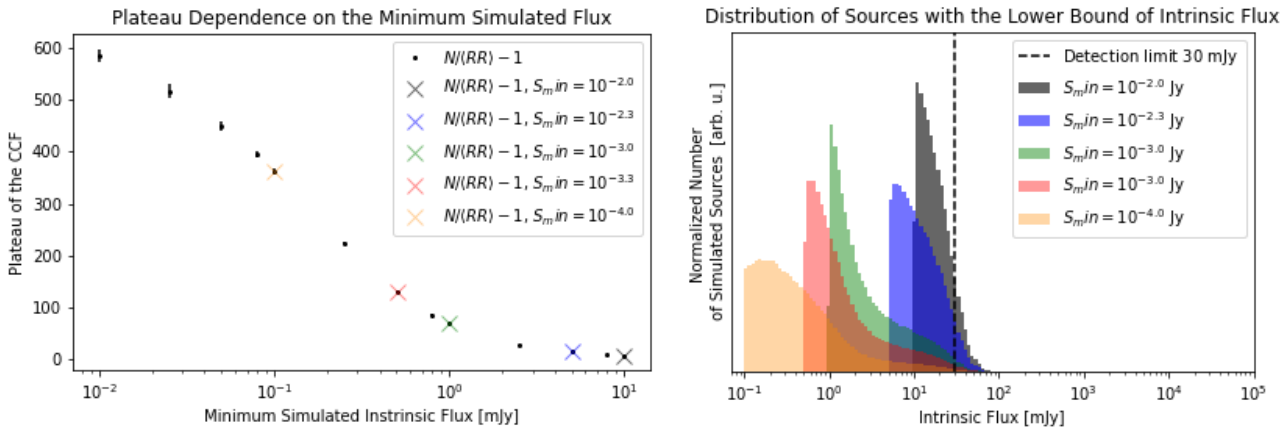

Figure 5.15: In the left panel the mean value of $N/\langle RR\rangle$ -1 is plotted against the minimum flux input into the flux generator function. At the right, the distribution of background sources with respect to the assigned intrinsic fluxes for five cases of the minimum flux.

The flux generator affecting the observed CCFs at any part other than the plateau was not considered. From figure 5.14, though, we see that the weak lensing region (i.e. $\theta \gtrsim 3$ arcsec) does not suffer any change of behaviour respective to the intrinsic flux distribution. Taking into account this, we can give a good description of the behaviour of $N/\langle RR\rangle$ either by saying that it is a function of the minimum value input in the flux generator -generally speaking of the intrinsic flux distribution-, or at least any other dependence has not been perceived.

Summarising our thorough analysis of this piecewise function, a nice conclusion is that we have gained a comprehensive way to fit the observed CCF data trends that is applicable anywhere. Similarly, the algorithm separates, according to numerical criteria, the regions of weak lensing from[68] strong lensing. From this point onwards, it will be useful to keep working with the

[67] We have omitted the y-scale since us choosing a logarithmic x-scale with a logarithmic-spaced binning makes the y-scale blow up to a meaningless scale.

[68] We remind again that *weak* or *strong lensing*, in this context, refers to the value of the magnification function in that angular separation.

piecewise function since we are able to perform complete fits with the theoretical + plateau CCFs; moreover, if any complex system is simulated, much clarity will be gained with these functions, since no divergence will spoil the fit at different angular regions. For example, if a BCG of $\sim 10^{13}\ M_\odot$ produced an increase of the magnification in the $10 - 100$ arcsec region, resulting in a $\gtrsim 1$ rise in the value of w, over a general halo profile of $\sim 10^{14.5}\ M_\odot$, it would be much harder to see if the theoretical fit of the general halo was left loosened and blew up in a caustic region. Also, regarding the plateau, as long as $w(\theta) \lesssim w_{\text{plateau}}$ at the θ range represented, we are safe to distinguish well double haloes.

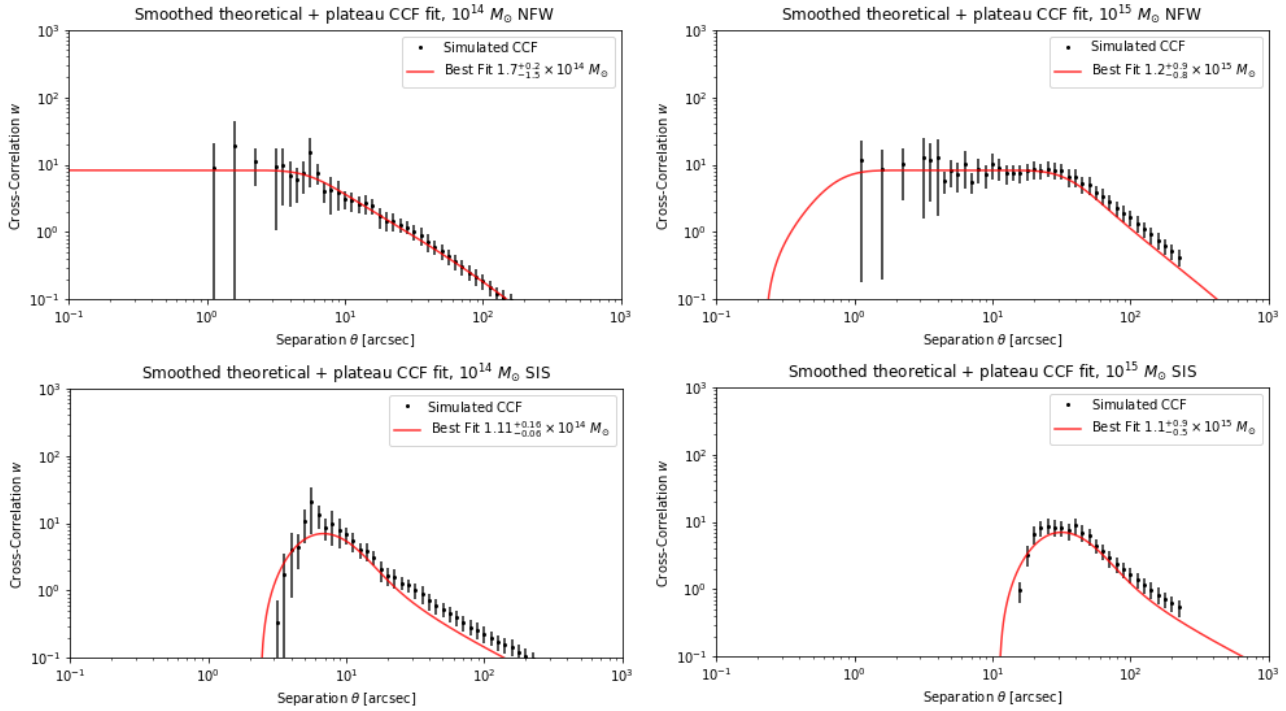

Figure 5.16: A smoothing was performed over the theoretical CCF + plateau for the $10^{14}\ M_\odot$ and $10^{15}\ M_\odot$ cases for both profiles. The σ of the smoothing was chosen in accordance to the one used in the maps of counts as it is explained afterwards ($\sigma = 2.4$ arcsec).

As an improvement to the piecewise function developed, and commented in the previous paragraphs, a smoothed version of it could be helpful since our work with pixelated maps of counts and our later smoothing ($\sigma = 2.4$ arcsec) of it (see figure 5.18 and the discussion around) would have the effect of smoothing the observed CCF. To give the idea of how it would be useful for a highly representative and well-fitted example, the upper right panel in figure 5.13 shows a smooth transition from the weak lensing part of the CCF to the plateau. Obviously, this improvement will be of little use if the available statistics to build up the observed CCFs are scarce and create variability and fluctuations along the trend. Furthermore, being realistic with respect to the results obtained so far, it seems like a second order improvement of the fit.

Anyway, in some situations (e.g. figure 5.19) the smooth will help to improve the readout of the mass parameter. The results obtained give back reasonable values when the fit is performed with *curve_fit*, whereas the self-made[69] least squares algorithm fails to produce a competitive readout.

Uncertainties, Resolution and Maps of Counts

Regarding the management of uncertainties, it is possible that some do not come from statistics and the methods used in the analysis, but the detectors themselves. Positional uncertainties in the location of the background sources might cause fluctuations and changes along the observed CCFs with respect with the theoretical models. From our perspective, we have to clarify that what we are testing is not a fluctuation in the θ of the background source that has implications on the value the magnification function $\mu \equiv \mu(\theta)$ takes, but a change of pixel in the map of counts due to a mistaken read of the location by the detector.

This is the way that errors could rise in the real case, so we performed some studies in order to calculate the effect of several random perturbations $\theta_{\text{map}} \to \theta_{\text{map}} + \delta\theta$; with $\delta\theta \sim \mathcal{N}(0, \sigma)$. Several levels of uncertainty were taken, from a slight one of $\sigma = 2$ arcsec and a huge one of $\sigma = 10$ arcsec. Remember that in the current maps of counts the size each pixel covers is 1 arcsec of the celestial sphere around the deflector.

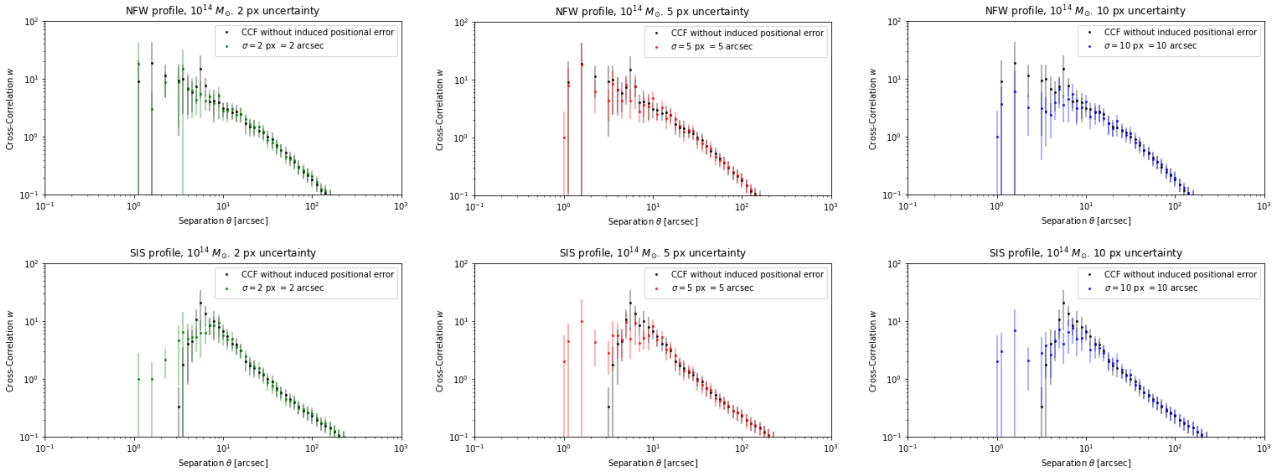

Figure 5.17: 10^{14} $M_\odot$ dark matter profiles distributed as NFW (upper row) and SIS (bottom row). The black trend is the simulated CCF shown in the central plots from figure 5.10. Green, red and blue trends represent induced positional errors distributed as $\delta\theta \sim \mathcal{N}(0, \sigma)$ with $\sigma = \{2, 5, 10\}$ arcsec respectively.

From figure 5.17 we learn that the NFW profile suffers little along the whole trend for the $2-5$

[69] Codes 10 or 11.

arcsec induced errors. This is a good feature since the smoothing -in line[70] with BON19 and FER22- that is to be used will be carrying a 2.4 arcsec Gaussian filter. When demagnification regions are involved -the SIS profiles show the feature- the positional errors move the observed CCF to much higher values, possibly due to the fact that the strong lensing region is so close in a linear angular separation scale (from 1 to 3 arcsec the bottom panels in figure 5.17 move sharply from demagnificaiton to strong lensing -caustic region-) that some sources lying within the caustic move to inner pixels causing an increase in the map of observed magnified sources. Indeed, this is nothing but a proof that uncertainties work like a smoothing, or can be taken into account by performing one over the observed maps of counts. The extreme cases of ~ 10 arcsec positional errors show greater divergences, although in the $\theta > 10$ arcsec region the effect is still unnoticed; possibly due to the fact that greater amounts of simulated sources in those annular regions result in a balance between those moved to greater separations and those moved to smaller separations, i.e. $\delta N(\theta_{\text{inner}} \to \theta_{\text{outer}}) \approx \delta N(\theta_{\text{outer}} \to \theta_{\text{inner}})$. It could be as well explained by the fact that the magnification function is much more smooth in the weak lensing region.

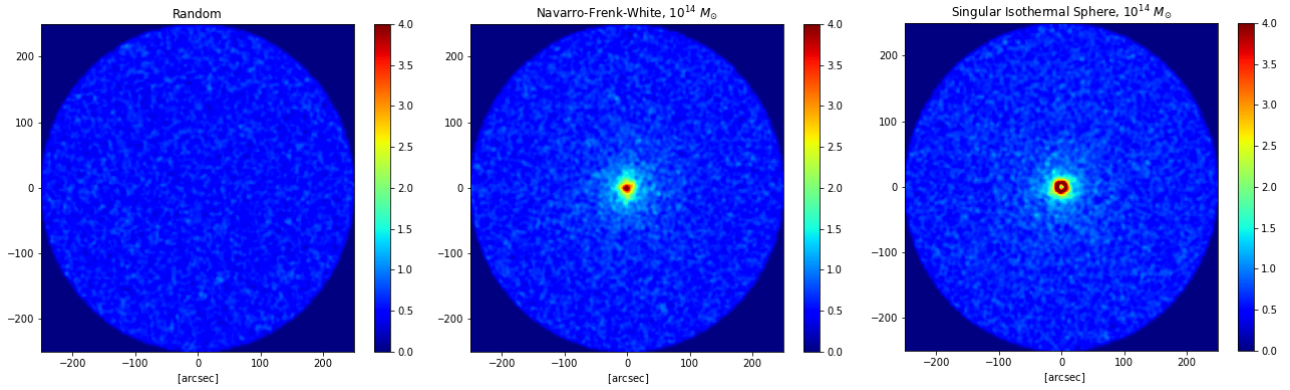

Figure 5.18: Maps of counts after a smoothing (not normalised) has been performed, with $\sigma = 2.4$ arcsec, following the values used in BON19 and FER22. A deflector mass of 10^{14} $M_\odot$ has been chosen for the representation, allowing some demagnification to be seen at the centre of the SIS profile (right panel).

BON19 and FER22 chose a 2.4 arcsec Gaussian filter in order to account for uncertainties in the location of the background sources. The location of the centre of the clusters was known with $\sigma_{\text{pos}} \lesssim 0.1$ arcsec (see FER22 for a more detailed discussion), which led the SMGs to be responsible for all the assumed uncertainties. The choice of that value followed from the results by Bourne et al. 2016 [38] which compares to previous work by Smith et al. 2011 [39] estimating a $\sigma_{\text{pos}} = 2.40 \pm 0.09$ arcsec for SPIRE objects. Maddox et al. 2018 [40] found 2.4 arcsec to be the positional accuracy for the faintest sources detected with the reviewed photometric bands

[70] See figure 3.2.

from PACS and SPIRE at section 4.1.

The result of having applied the smoothing on the maps of counts is figure 5.18, where the three maps (random, NFW magnified and SIS magnified respectively from left to right) are presented for a deflector of mass[71] 10^{14} $M_{\odot}$. The demagnification region of the SIS profile can be seen for this mass, although greater masses[72] make it easier. The scale of the data should be modified in each case since the number of sources that can overcome the threshold varies with changing masses of the deflector. The colour scale can be also varied so that the total number of pixels sum up 1; this is, normalising the map as done in figure 3.2. Figure 5.19 shows the fit of the observed CCF arising from maps in figure 5.18 with a smoothed theoretical CCF+plateau.

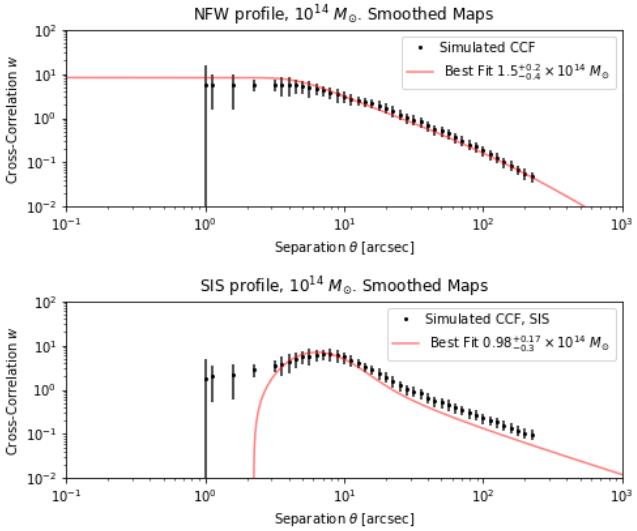

Figure 5.19: Smoothed fit with plateau of the observed CCFs calculated with the data from figure 5.18.

Choosing a greater resolution would work well to improve the resolution of the profile at smaller angular scales. Particularly it could be a useful tool to test the behaviour of the NFW profile in the demagnification region. Performing all the computations again for a map of pixels of size 0.1 × 0.1 arcsec^2 -keeping the window of 250 × 250 arcsec^2- takes more computational time (due to them being 100 times bigger than those figures). For that reason, we have chosen to test the simulation in pixels of size 0.1 × 0.1 arcsec^2 just for the NFW profile with a mass of 10^{15} $M_{\odot}$, to look at the resolution at < 1 arcsec.

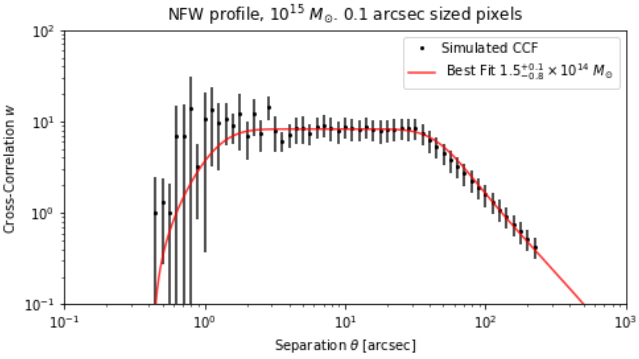

Figure 5.20: Smoothed fit with plateau of the observed CCF calculated with a magnification function from a NFW profile of 10^{15} $M_{\odot}$. The resolution (pixel size) is 0.1 arcsec, allowing us to see the demagnification region in the observed CCF at < 1 arcsec.

The observed CCF and its theoretical fit are shown in figure 5.20. We see that with this

[71] The mass only affects the magnified maps -central and right plots-.

[72] See figure C.2 in appendix C, where 10^{15} $M_{\odot}$ profiles generating maps of counts similar to figure 5.18 were displayed.

smaller resolution, the demagnification region can be perceived. Apart from that, the general trend that we had already seen of smaller angular distances producing greater fluctuations in the CCF is still present in this figure. Notably, whereas before the < 5 arcsec region presented huge uncertainties and fluctuations, now we have to go well below 1 arcsec to see them. One can conclude that uncertainties in our simulator are triggered by the amount of pixels belonging to the annular regions that each point in the observed data trend represents. With more pixels entering each ring at greater angular distances, uncertainties diminish until they reach a stable point in the right-hand side of the trend.

We have not spent too much time on describing figure 5.18, but there is a rather evident difference with respect to the maps of counts observed by BON19 (upper panel in figure 3.2) and FER22 (right panels in figures 6.10 and 6.11). Overdensities in the our map of magnified counts are centred in the inner 100-round arcsec, while in the plots from BON19 they had a greater size and in FER22 the scattered overdensities reached greater concentrations of sources, i.e. scattered regions reached similar densities to that at the centre of the cluster (the map). Note as well how the colour scale chosen by FER22 -the same as ours- in their figure makes it easy to draw the comparison to the present work.

The Effect of Distributions: z_f, z_b, M_{200} and C

Calculating the magnification function for each pair of background and foreground sources with their respective redshifts z_b and z_f (z_s and z_d if following the notation from section 2.2) carries a huge computational effort (programmes 4 and 3 with the $Gz = True$ take many more minutes to execute than the latter with $Gz = False$ -using therefore maps of magnification instead of calculating the magnification for each pair-). Moreover, doing so would be of little use, since we know that the greatest variability of the magnification functions is at typically low angular separations. For that reason, we have been using the average measured (respectively) redshifts from the samples used in FER22 for every background and foreground source. What is more, unless the opposite is explicitly said, for the rest of the project magnification maps calculated at average redshift will be used.

Now we are testing the variability of the CCFs with distributions of redshift for the sources. The first thing we need is a function to distribute the sources with redshift in an analytical way (or described by a *python* function) that resembles the distribution followed by the sources FER22 used. We can see from figure 5.21 that two normal distributions serve quite well to produce analytical distribution functions. The mean and standard deviations were the ones

obtained from the real samples and, as can be seen in the bottom panel, the sample and the simulated distributions resemble to one another. Knowing this, we can use the normal distributions used for the fit as generators of redshifts for our sources.

In figure 5.22 the results are shown and it can be seen how distributing sources with redshift implies little variation with respect to the other cases -we should focus the most in the upper panels with the red trends, where we have not applied the Gaussian filter on the maps of counts-. We can therefore assume that the average value of each sample is enough to produce reliable readouts for our purposes. Of course, this all depends on where we put our request of CCFs being well reconstructed. At the end of the day, if the simulator is unable to return parameters within certain limits[73] asking for a realistic distribution of redshift-distributed sources is useless: it will not affect the readout significantly. Above 10 arcsec it seems that the observed CCFs are quite similar to the original ones from figure 5.10. The 10^{14} $M_\odot$ case for the SIS profile with the Gaussian filter applied (blue trend) shows a difference with respect to the non filtered CCF. For its similitude with the bottom panel of figure 5.19, we have to assume that it is due to the Gaussian filter itself. For the rest of the cases the CCFs behave quite similarly.

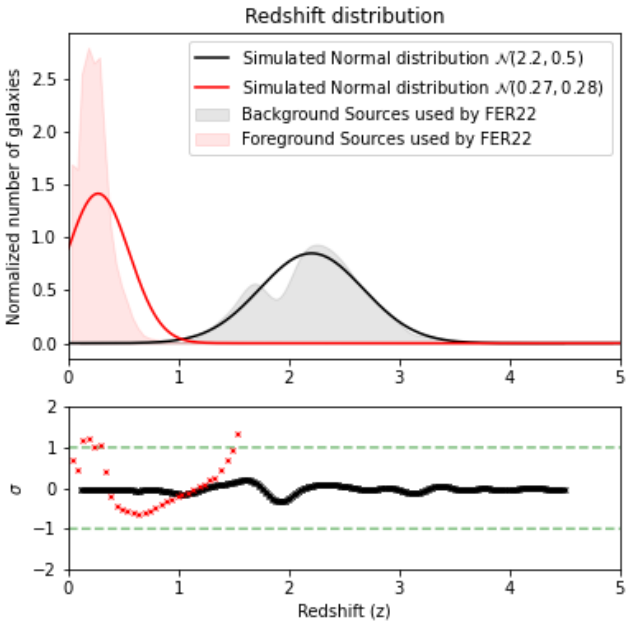

Figure 5.21: The upper panel shows as shaded regions the histograms with bins of width 0.1 and 0.5 in redshift for foreground (red) and background (grey) samples. Solid lines represent the normal distributions thought to be used as generators of random redshifted sources. In the bottom panel, the deviation (in σ) of the data sample from the simulated distributions.

The last test constitutes the most physically accurate simulation of a real work with stacking to obtain information about virial mass and concentration, while still working with single profiles. Note that our interest in the following results section is not in performing complicated and time-consuming computations to obtain results from a physically accurate distribution of sources in terms of redshift, virial mass or concentration distributions. Instead, there we are testing double-profile simulations trying to get close to the work by FER22. Now, however,

[73] e.g. the same value for the mass and concentration as the ones that were introduced to create the magnification function with just few divergences in the last decimal positions

our last toy model test consists in a comprehensive variation of every single parameter: z_f, z_b, M_{200} and C. Take as a reference code 4.

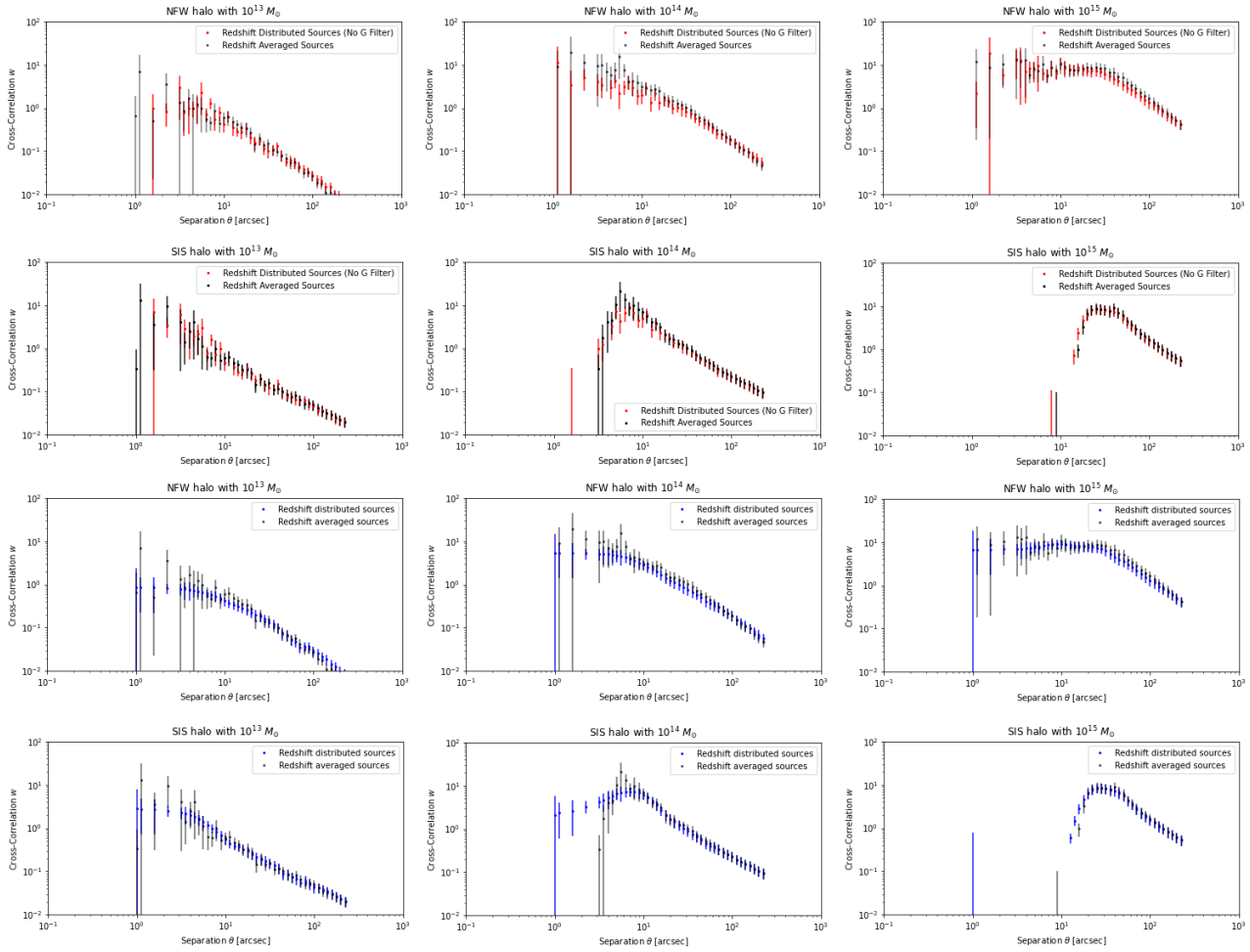

Figure 5.22: Same plots as in figure 5.10 but omitting the fits to theoretical CCFs to make the figure look clear. Red trend represents the sources that were simulated with a distributed redshift according to the Gaussian functions from figure 5.21, without a Gaussian filter applied to the maps of counts. Blue trend represents the same as the red trend but with a Gaussian filter applied. Grey trend is the same one as in figure 5.10.

The variation in the virial mass and concentration cannot be followed from any previous work since FER22 used a bins of richness to perform a kind of tomographic analysis on their samples of foreground sources -and therefore background sources since the latter were attached to each of the ones from the foreground sample-. We define our distribution of sources with respect to both virial mass and concentration as normal distributions centred in $\bar{M}_{200} = 10^{14}\ M_\odot$ and $\bar{C} = 4.0$ respectively. As standard deviations we have chosen half the mean values ($\sigma_{M_{200}} = 5 \times 10^{13}\ M_\odot$ and $\sigma_C = 2.0$). If we look at table 3.1, our choice would be a mixture of the concentration expected for the inner halo terms of the intermediate bins (2 and 3) and an overall virial mass that accounts for the total contribution of the two parts, in the total mass range of the three first bins.

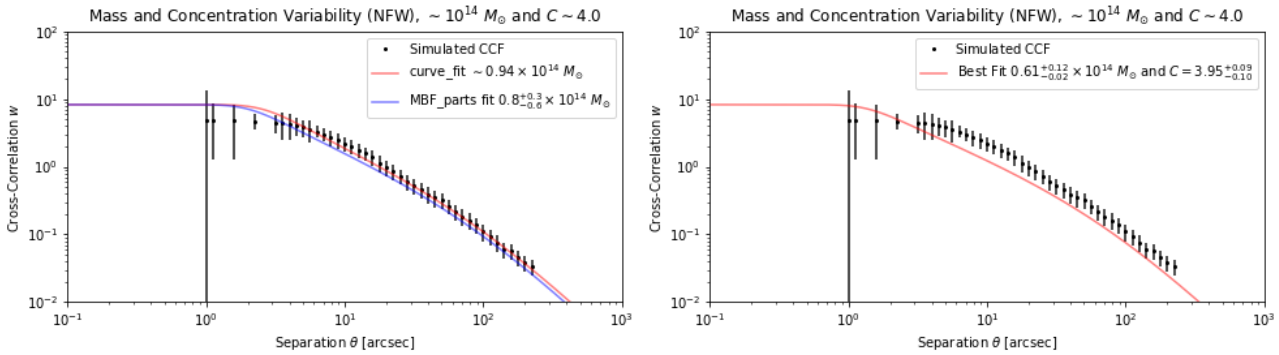

Figure 5.23: In the left panel, the fit with fixed concentration at $C = 4.0$. Both methods to determine the virial mass (codes 10 in blue and 12 in red) were used. Note that the *curve_fit* based test does not return acceptable levels of uncertainty, so we just indicated the fiducial value. In the right panel, the multivariable analysis on both M_{200} and C; check the work with uncertainties in the text.

In figure 5.23 we see the results of this simulation. We performed three different fits[74] on the obtained CCF. In the upper panel we fitted with only mass-varying theoretical CCFs, we refer to codes 10 and 12. The *curve_fit* based code was unable to produce appropriate uncertainties for us to put in the figure, so we indicated only the fiducial value. By eye, though, the *curve_fit* analysis seems the one that adjusts best the data trend. Only a *curve_fit* based algorithm was able to produce a multivariable analysis on M_{200} and C. Uncertainties were obtained not from the fitting function but averaging the mean values obtained from the algorithm when the bounds in the fit (line 12 in code 13) were changed by taking them from a preexisting array of bounds.

[74] A self-made least-squares method based on code 10 was tried for the multivariable analysis on M_{200} and C, but results were completely unsatisfactory.

6 Results

Now that the robustness of our simulator has been thoroughly explored, we can start performing tests of physical interest. Those tests are going to be related to the work already undergone by FER22, but taking things a step further. To give some examples, in the first subsection we are going to test the characterisation of double profiles -accounting for a BCG and a general halo-, the observed CCF trend that our simulator offers, and how it adapts to the results by FER22.

In the second subsection we will explore the gaps and hills observed by FER22 in their richness-divided analysis by changing the CCF double compound profile for an inner profile that remains unchanged -chosen following the work of FER22- and a sequence of SIS profiles at greater angular scale. Apart from that, we will recover the discussion initiated in the previous section when we saw that the simulated maps of counts presented some differences with respect to those observed by FER22.

6.1 Profile Characterisation

This simulator will prove to be useful if it helps to determine mass, concentration and some other properties of the dark matter haloes attached to cosmological deflectors. The first step into that path is checking the differentiation between the shapes of NFW and SIS profiles. To that end, we have performed simulations at the three masses commented in previous sections.

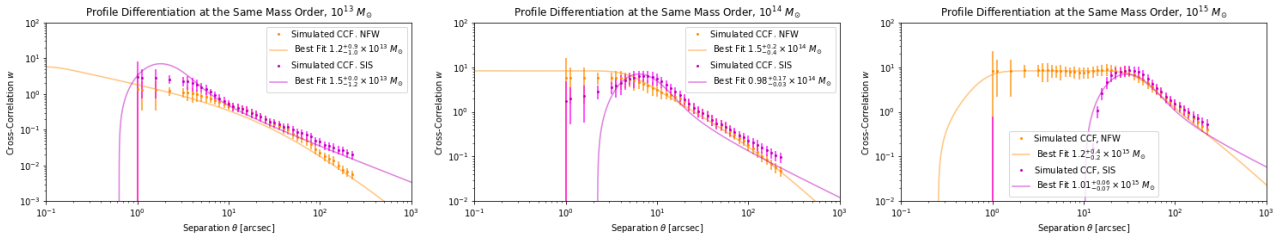

Figure 6.1: Combined plots for both profiles (NFW and SIS) at the three mass orders. Smoothed profiles at low mass regimes $\lesssim 10^{14}\ M_\odot$ are quite similar to each other, while at $10^{15}\ M_\odot$ the difference is much more clear due to the wide range of the SIS demagnification region.

It could happen that with not a large amount of data (to give an idea, around 10^5 magnified sources surpassed the detection limit) the two profiles get confused both in shape and returned values of target parameters. Certainly, it is the shape of the profiles what enables us to distinguish one from another, so good statistics would be needed in order to assess a type of profile

for each of them. Regarding the mass value obtained with the fitting functions[75], a wide initial range of values (10^{11} to 10^{17} $M_\odot$) was allowed; but the programme effectively returned good readouts in accordance to the input mass orders in each case. The nominal result (either NFW or SIS) on the type of profile could not be performed through the *curve_fit* method, so we used our self-made least-squares algorithm. Consistently, it chose the input type of profile as the best fitting one. Seemingly the developed programme is capable to tell more than an outcome of parameters that match -within their uncertainty range- the input values. Note, in any case, that the 10^{14} $M_\odot$ NFW profile fit falls short to include the input value in the returned band of uncertainty for the virial mass parameter.

Outcome of Parameters

Once we have a system to differentiate different profiles developed, is time to test the simulator on its ability to characterise compound profiles. This was the main objective of the work of FER22. To that end, a battery of **simulated**[76] CCFs is needed. To adapt and compare results to the previous work by FER22 and since we have spent quite a long time considering the effect of different virial masses, we are using the results for the aforementioned parameters from table 3.1 (they can also be seen in the FER22 columns in tables C.1 and C.2). There is another reason for using those values. Even if they were somewhat[77] mistaken with respect to the *real*[78] ones, they are well suited to produce a *double deck* in the shape of the simulated CCFs. This corresponds to two profiles getting one region of dominance each in the same range of angular separations. For the rest of the work, unless said otherwise, we are using 10^6 **magnified** sources. Obviously translating into a much greater number of total simulated sources $\sim \mathcal{O}(10^7)$.

To build up the magnification maps, two options have been considered; they are explained at the end of section 2.4. However, our work is typically with the cross-correlation functions. We need to know if there is any theoretical requirement to build the CCF from a compound magnification profile. The theoretical function is still $w_x = \mu^{\beta-1} - 1$, only now μ is not an analytical function but a composition of two different magnification functions following the indications on (2.41) -**case A**- or the following paragraph -**case B**-. From a physical point of view is the latter that makes more sense. We should think of two haloes separated in the

[75] Codes 10 and 11.

[76] Now that we are directly comparing results from FER22 with our simulations there is a need to distinguish the origin of the shown CCFs. Apart from indicating that appropriately in the plots to be shown, **observed CCF(s)** will refer to theirs while **simulated CCF(s)** to ours.

[77] FER22 acknowledges that the obtained values from their fits are not in complete agreement with mass-richness nor mass-concentration expected relations (fourth paragraph of their section 5.1.1).

[78] If the NFW profile was a good approximation to the physical mass distribution of dark matter.

direction of the line of sight enough so as to think magnification $S_{\rm intr} \to S_{\rm obs} = \mu \cdot S_{\rm intr}$ as two independent processes $S_{\rm intr} \to S_{\rm H1} = \mu_1 \cdot S_{\rm intr} \to S_{\rm obs} = \mu_2 \cdot S_{\rm H1} = \mu_1 \cdot \mu_2 \cdot S_{\rm intr} \equiv \mu_{\rm TOT} \cdot S_{\rm intr}$. This is what was explained there in section 2.4, but how does that translate into the CCF? Well, the answer is just introducing $\mu_{\rm TOT}$ into $w_x = \mu^{\beta-1} - 1$. Luckily, there is no need of making any further simplification or working any mathematical derivation. By knowing that magnification and CCF can be written each of them as a function of the other is enough. When we restore parameters (in this little example let's suppose we treat a compound of two NFW profiles, one for the BCG term and the other for the cluster halo) from the simulated CCF, we will do

$$\{M_{\rm in,\ C_{in},\ M_{out},\ M_{out}}\} = {\rm Fit}\,(w_{\rm obs}, w_{\rm teo}) \tag{6.1}$$

with

$$w_{\rm teo} = \mu^{\beta-1} - 1 = (\mu_{\rm in} \cdot \mu_{\rm out})^{\beta-1} - 1 = (\mu\,(w_{\rm in}) \cdot \mu\,(w_{\rm out}))^{\beta-1} - 1 \tag{6.2}$$

and

$$w_{\rm out} \equiv\ w\,(M_{\rm out}, C_{\rm out}) \quad , \qquad w_{\rm in} \equiv\ w\,(M_{\rm in}, C_{\rm in}) \tag{6.3}$$

where $\mu(w)$ is the inverse function of $w(\mu)$, which is fortunately just the inversion of an exponential and therefore analytical as $\mu(w) = (w+1)^{1/(\beta-1)}$. The functions used to perform the fit commented in equation (6.1) can be found in appendix B, they are codes 14 and 15.

To get started we plot in figure 6.2 the results of having introduced the obtained values for the virial masses and concentrations in the second bin of FER22 (see table 3.1), namely $M_{\rm in} = 2.3 \times 10^{13}\ M_\odot$, $C_{\rm in} = 6.83$, $M_{\rm out} = 7.9 \times 10^{13}\ M_\odot$ and $C_{\rm out} = 0.39$. We chose this bin since we can see in the left panel of figure 3.5 that it is the case where the parameters create two well differentiated regions, the inner clearly dominated by the BCG halo term and the outer by the cluster halo. The colours of the fits in the following figures were chosen so that they matched the colours chosen by FER22, so that comparisons are easier to draw. For the fit of case A we have not only performed the one detailed above -which is a fit for the compound theoretical CCF- (the solid lines in the upper panel of figure 6.2) but also to each dominance region independently (with code 13).

The general halo fit does not change much if the local fit is chosen in the upper panel -actually it can be seen by eye-. The virial mass varies from $\sim 18.20 \times 10^{13}\ M_\odot$ (local) to $\sim 16.90 \times 10^{13}\ M_\odot$ (general fit) and the concentration from ~ 0.46 (local) to ~ 0.42 (general fit). It is the BCG term that suffers greater variations, indeed both parameters change conversely to one another. Concentration is related, for the range of values we work with, to the slope of the fitting curve -being clearly steeper the general fit BCG profile-; while the virial mass would pull the whole profile to the right (as mentioned above in the Toy Model section). For those reasons, the local fit (dashed red trend) returns $M_{200} \sim 6.92 \times 10^{13}\ M_\odot$ and $C \sim 3.83$ against a global fit that offers $M_{200} \sim 1.18 \times 10^{13}\ M_\odot$ and $C \sim 6.82$. The distinction of the regions was estimated beforehand with a function built up to that end (code 16) that returns the limiting angular separation between them. In the bottom panel, the simulated CCF used data which underwent a magnification function following case B. Note that we have not tried a local analysis of each part there since the shape of the trend does not allow for an easy identification by eye, even if the limiting angular separation was decided with the algorithm prepared for it. Note as well that either choosing the case A or B produces quite different effects on the shape of the simulated CCF, with the case A (being the magnitude calculated as the maximum of the inner and outer functions) showing a non-smooth continuity at $\theta \sim 20$ arcsec, matching the angular separation marked with a dashed vertical line in the right panel of figure 3.5. Testing the presence of such non-differentiable shapes tells us about how dark matter haloes are embedded into one another, and whether the dominance of the BCG halo region is relevant or not.

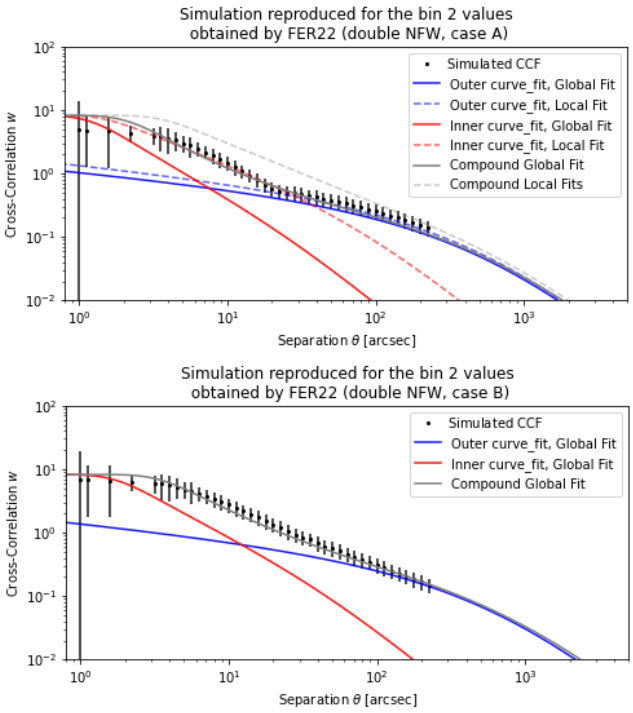

Figure 6.2: The simulated CCF calculated following equation (2.41) (case A, upper panel), and following the product of the individual magnifications (case B, bottom panel). The solid red (blue) tendency is the theoretical CCF for the inner (outer) halo term, calculated with the parameters returned from the global fit. In the upper panel local fits were also calculated.

Figure 6.3 shows the results of having performed a fit on the simulated CCF for the two types of compound profile that FER22 treated, we chose to represent the case with the product

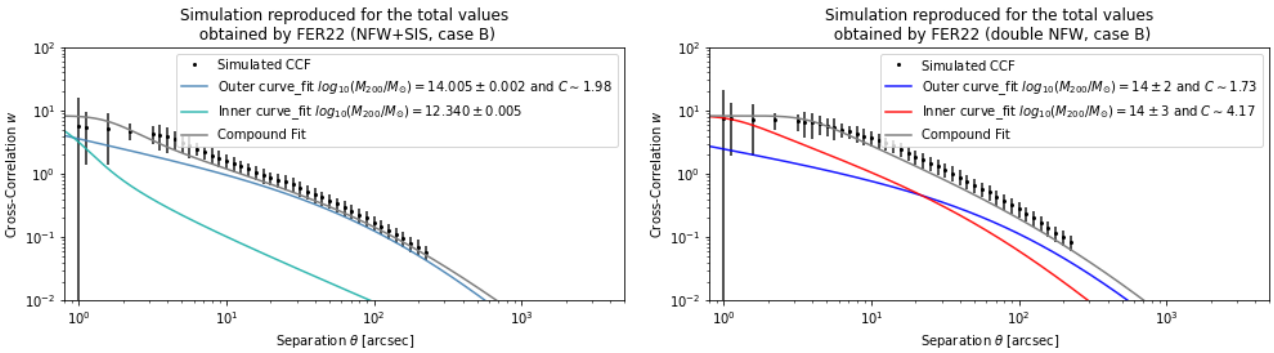

Figure 6.3: Simulated CCF and performed fit for the SIS+NFW (left panel) and double NFW (right panel) profiles. The input parameters were the ones that can be found in the last column of table 3.1 -from the *total* case, which is a result of having used all the available data altogether regardless of richness divisions-.

magnification since it is the most realistic from a physical point of view[79]. Before discussing the uncertainties, we stop to see that the obtained values after the regression were in the expected order of magnitude. In the NFW + SIS case the fitting algorithm (based on *curve_fit*) provides an estimation of the BCG mass somewhat shorter to the input value ($\sim 0.2 \times 10^{13}\ M_\odot$ vs. $0.5 \times 10^{13}\ M_\odot$ as input), while it gives out an overestimation of the cluster halo mass ($\sim 10^{14}\ M_\odot$ vs $5.5 \times 10^{13}\ M_\odot$ as input). When it comes to the concentration, the fit does not change much the input value. In fact, for all the results we have obtained, the concentration did not vary much with respect to the input. The fitting algorithm did not provide satisfactory uncertainty levels for that parameter, so they were not included in the figures.

The latter is a good link to start covering the issue of uncertainties. First of all, it is not easy to estimate together cluster masses in units of $M_\odot$ -accounting for values of order $\sim 10^{14}$- and concentrations of order $\sim 10^0 - 10^1$. Naturally, the *curve_fit* algorithm finds struggle managing such unalike numbers, so we chose to work with the decimal logarithm of the virial masses, which give out reasonable numbers -as they belong to $\sim (1, 100)$-. We tried before working in units of $10^{13}\ M_\odot$, which would be similar numbers in the range $\sim (0.1 - 1000)$, but the algorithm failed to return any other value than the ones introduced for every input. Figures C.4, C.5, C.6 and C.7 in appendix C present the results for the fit performed with all the inputs available from the results of FER22. Results of the fits from the referred figures are written in tables 6.1 and 6.2. Those are presented without the uncertainties since they can be seen already in the figures. As we said, we are working with case B to calculate the magnification; therefore, results for case A are left for the appendix, in tables C.1 and C.2. As can be checked,

[79] Although as we can see in some of the plots by FER22, their observed CCF -**we refer to the bare data, only having computed the CCF, but nothing else**- does show quite of a sharp border between two tendencies. In the second bin of richness (figure 3.5) the effect is more visible.

the results are no better than the ones in the tables right below. Our simulator was able to keep the outcome parameters within close range to the inputs, so that the growth trend in the mass of the cluster halo is tracked, as well as all other results obtained by FER22, naturally. However, some differences can be noticed, as for example in the mass of the cluster haloes in the second, third and fourth bins for the double NFW profile. There, the outcome mass for the deflector doubles the input mass.

	Parameters	Bin 1		Bin 2		Bin 3	
	$[M] \equiv 10^{13}\ M_\odot$	FER22	Out B	FER22	Out B	FER22	Out B
SIS + NFW	$M_{\rm SIS}$	0.5	0.5	0.6	0.6	0.6	0.6
	$M_{\rm NFW}$	4.9	7.9	5.3	17.4	10.1	19.9
	C	0.94	0.95	0.30	0.33	1.17	0.81
Outer	$M_{\rm NFW}$	5.8	10.3	7.9	16.1	11.2	24.1
	C	0.74	0.86	0.39	0.39	1.00	0.90
Inner	$M_{\rm NFW}$	3.8	1.2	2.3	2.4	7.2	2.6
	C	3.63	6.51	6.83	6.83	3.81	6.82
Inner + Outer	$M_{\rm TOT}$	9.6	11.5	10.2	18.5	18.4	26.8

Table 6.1: Output values from our fitting algorithm after having introduced FER22 results, accounting for bins from 1 to 3.

	Parameters	Bin 4		Bin 5		Total	
	$[M] \equiv 10^{13}\ M_\odot$	FER22	Out B	FER22	Out B	FER22	Out B
SIS + NFW	$M_{\rm SIS}$	0.6	1.5	1.0	0.7	0.5	0.2
	$M_{\rm NFW}$	14.0	14.2	51.5	78.7	5.5	10.1
	C	0.65	0.35	0.56	0.30	1.84	1.98
Outer	$M_{\rm NFW}$	27.4	39.5	51.5	47.1	7.1	8.5
	C	1.74	1.64	0.56	0.56	1.72	1.73
Inner	$M_{\rm NFW}$	1.0	0.4	1.0	0.9	4.1	4.9
	C	11.91	11.86	14.8	14.79	4.17	4.17
Inner + Outer	$M_{\rm TOT}$	28.4	39.9	52.5	48.0	11.2	13.4

Table 6.2: Output values from our fitting algorithm after having introduced FER22 results, bins 4, 5 and the totals.

That some figures do not get a perfect fit by eye does not need to mean anything. To give an example, figure 6.4 shows the result of having performed a fit for the simulated CCF with the inputs of the fifth bin of richness where, at the left, we have let the algorithm go alone with the sole hint of the inputs we had introduced. At the right, we modified the seeds of the fit algorithm so that we observed the best adjustment of the theoretical function (grey solid line) to the data. The parameters introduced can be seen in the fist row of table 6.3, and the outcome provided by the algorithm in the second one. Naturally, the logarithmic scale hides

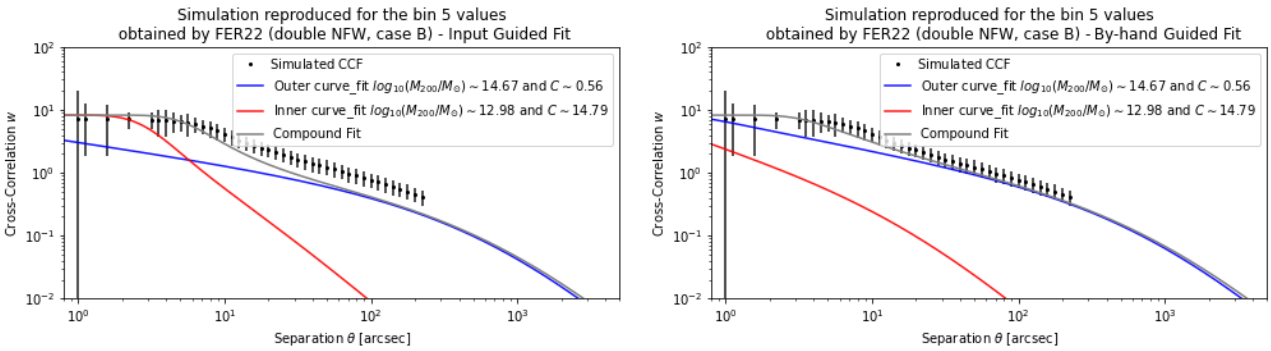

Figure 6.4: The left panel shows the outcome given when we put the input parameters as seed. In the right panel, we forced the seed parameters so that, by eye, the grey trend (the overall fit) resembled the most the simulated CCF. All the needed parameters are shown in table 6.3

from our view that a perceptible deviation at the rightest part of the trend can be much smaller than a (by eye) negligible deviation at low θ. Table 6.3 shows the total accumulated deviation of the fit from the simulated CCF in the linear and logarithmic cases. In the bottom rows the mean deviation is presented (mean deviation by data point of the trend). Note that the guided fit (right columns) obtains smaller deviations, which means that some degeneracy would be expected in the plane of the best fitting parameters.

	Guided by FER22				Guided by Hand			
	$M_{\rm in}$	$C_{\rm in}$	$M_{\rm out}$	$C_{\rm out}$	$M_{\rm in}$	$C_{\rm in}$	$M_{\rm out}$	$C_{\rm out}$
Input	1.0	14.8	51.5	0.56	2.51	6.80	467.7	0.64
Output	1.0	14.79	46.8	0.56	0.5	6.79	89.1	0.64
$\left[\sum_i (\mathrm{Fit}_i - \mathrm{CCF}_i)^2\right]^{1/2}$		16.37				16.07		
$\left[\sum_i \log_{10}^2 (\mathrm{Fit}_i/\mathrm{CCF}_i)\right]^{1/2}$		3.03				2.73		
$\langle \mathrm{CCF} \rangle$			3.17					
$\langle \delta \mathrm{CCF} \rangle$		0.39				0.38		
$\langle \log_{10} \mathrm{ObsCCF} \rangle$			0.34					
$\langle \delta \log_{10} \mathrm{ObsCCF} \rangle$		0.07				0.06		

Table 6.3: Comparison between an input-guided fit and one guided by hand so as to produce the best fitting pattern at all scales by eye. The simulated CCF was produced with the parameters obtained as a result of the work of FER22 for their fifth bin of richness, we used the method B (magnification functions product) to produce the total magnification function.

$10 - 25$ **arcsec Characterisation**

As commented in section 3.3, one important side revelation from the work of FER22 was the consistent -at all richness bins- presence of a lack of signal in their observed CCFs at particular angular scales ($\sim$ 10 and $\sim$ 25 arcsec). With our simulator it is possible to try combinations of magnification functions in order to obtain different shapes in the CCFs. We will now test different combinations that could reproduce a gap in the 10 arcsec region.

A big part of this work was dedicated to explore demagnification regions from different profiles. We saw that SIS profiles had much narrower strong lensing areas, leaving at smaller angular scales perceptible demagnification effects. Particularly, this region mounted up to somewhat above 10 arcsec in the 10^{15} $M_{\odot}$ case. Although the SIS has long been set aside due to a common preference for the NFW profile, it could happen that the right combination of profiles reproduced well the commented lack of signal in the observed CCFs by FER22 at 10 arcsec. There is one aspect to take into account that arises from the present work. When we reviewed the effect of a lower limit in the simulated range of intrinsic fluxes, we discovered that it translated into a plateau effect in the CCFs. A 10^{15} $M_{\odot}$ SIS profile produces a caustic above 10 arcsec, that translates into a plateau in simulated CCFs. However, what we saw at FER22 -in the most extreme cases which where the fourth (bottom panel from figure 3.4) and fifth bins of richness-, is an increment of the CCF that does not get to the maximum of the trend of the CCF. Moreover, in other bins of richness (e.g. the second in figure 3.5) the small *hill* in the CCF after the gap at $\sim$ 10 arcsec is much more subtle. Therefore, as a previous idea, we do not expect that a SIS profile of these characteristics is the physical cause behind the gap, however it can help to shed light on the issue. We have decided to try two cases; in the first case a double SIS profile -which is something relatively new and different from what FER22 did. Notably they assumed that the NFW was the best-fitting model for general haloes-. Then we tried to fit a NFW profile for the inner region, the reason why we did this has to do with what we can see in the left panel of figure 6.5: an inner SIS profile means another demagnification region at the smallest scales which translates into a fall in the CCF.

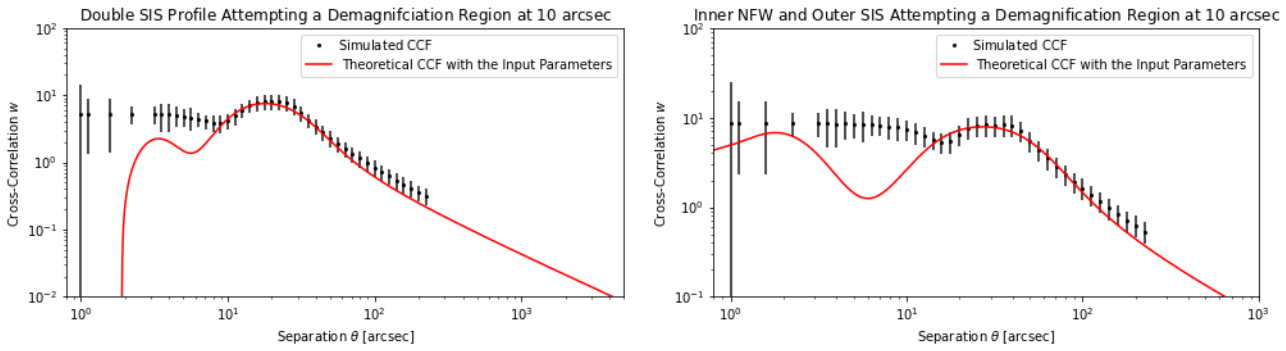

Figure 6.5: Double profiles trying to reproduce the gap of the signal in the observed CCFs by FER22. At the left a $10^{14.7}$ $M_{\odot}$ SIS outer profile and another $10^{13.6}$ $M_{\odot}$ SIS inner profile were simulated. At the right a $10^{15.0}$ $M_{\odot}$ SIS outer profile combined with a $10^{14.2}$ $M_{\odot}$ NFW inner profile with a concentration of 6.0.

Indeed, what we see in the left panel of the figure above is that at the lowest angular scales ($\lesssim$ 10 arcsec) the simulated CCF does not reach such a high value as it does at $\sim 10 - 40$

arcsec. On the other hand, the right panel shows a much stronger signal at lower angular scales and a not so deep gap which goes in accordance with the three lowest bins of richness from FER22. What is more, the outer SIS strong lensing region is no higher than the low angular scale plateau. Apart from all of that, the NFW mass for the inner profile clearly exceeds the upper bounds allowed for a BCG halo; $\sim 10^{14.2}\ M_{\odot}$ is clearly beyond what is expected for an inner thick galaxy and its halo. Without such a big inner mass, we would be back in the left panel case; which is contrary to observations by FER22 where never did the fluctuations at $\gtrsim 10$ arcsec overcome the value of the CCF at low angular scale.

Regarding the comparison between the simulated CCF and the theoretical[80] function we see that at great angular scales ($\gtrsim 10 - 20$ arcsec) the fit is good, so that the simulated CCF behaves independently of statistical effects from the simulation and distribution of sources. At lower angular scales, however, the fit does not work. In order to explain this, the most natural way is saying that rapid fluctuations in the theoretical trend do not translate into macroscopic effects in the simulated CCF. This is possibly due to the effect of both counting sources from maps in annular regions -which means that small averages take place at every data trend point- and the smoothing of the maps of counts. Note as well that the lack of a gap in the lowest angular scales (~ 1 arcsec) in the left panel of figure 6.5 can be partially explained by it. It is quite natural though, if we think of the effect we saw in the SIS smoothed case of $\sim 10^{14}\ M_{\odot}$ in either the middle panel in figure 6.1 or the bottom panel in figure 5.19.

We could say that the above results do not make the satisfactory conclusion we would like them to be. Apart from the issues about a strong lensing regime at great angular scales -which is not what is observed in FER22- and the discrepancies between simulated and theoretical CCFs, we have not discovered a method to reproduce a gap at ~ 25 arcsec. When FER22 tackled the issue of the behaviour of their observed CCF at $\sim 10 - 25$ arcsec, they commented how there was a gap in the CCF also at that angular separation. It is notorious in bin 4 as well, and also in bin 3 where there is a clear lack of one or two points of the CCFs at that angular region. Taking a comprehensive look at all the plots, the general trend seems to be a cyclic-like pattern of variability with little *hills* and *valleys* or gaps in the CCF at radial angular separations $\gtrsim 10$ arcsec and onwards. One idea to cover the issue is the simulation of small galaxies or little clusters within the general halo term at fixed[81] angular scales. The morphology of clusters is rich and through the stacking method any morphological particularity of a certain

[80] We calculated it following (6.2).

[81] At least in each bin of richness and keeping the 10 arcsec gap as a common point.

cluster is lost. Indeed we do not care about the internal structure of clusters as such, but we see their dark matter distribution through the lensing effect on background sources that can fall anywhere at a radial angular scale from the centre of the cluster. However, if a pattern of distances was common for all clusters so that it is no rare to find overdensities of matter at certain separations from the centre of the cluster or the BCG, it could be possible to spot it inferring from observed CCFs.

As a simple test, we have introduced a dark matter profile eccentric[82] to the general halo and the inner halo profiles. The ground level of our simulation are matter distributions for the cluster halo and the BCG. We have chosen two NFW profiles of $10^{13.4}$ $M_\odot$ with $C = 10.0$ (for the BCG) and $10^{15.0}$ $M_\odot$ with $C = 0.30$ (general halo). Additionally, we have introduced[83] a $10^{12.2}$ $M_\odot$ SIS profile at 10, ~ 12.6 ($10^{1.1}$), ~ 15.8 ($10^{1.2}$) and ~ 20.0 ($10^{1.3}$) arcsec. These and any other extra dark matter concentrations at eccentric positions from the cluster halo centre have to be introduced into the radial magnification function and then rotated to produce the revolution magnification maps (one of the codes used to this end is 6).

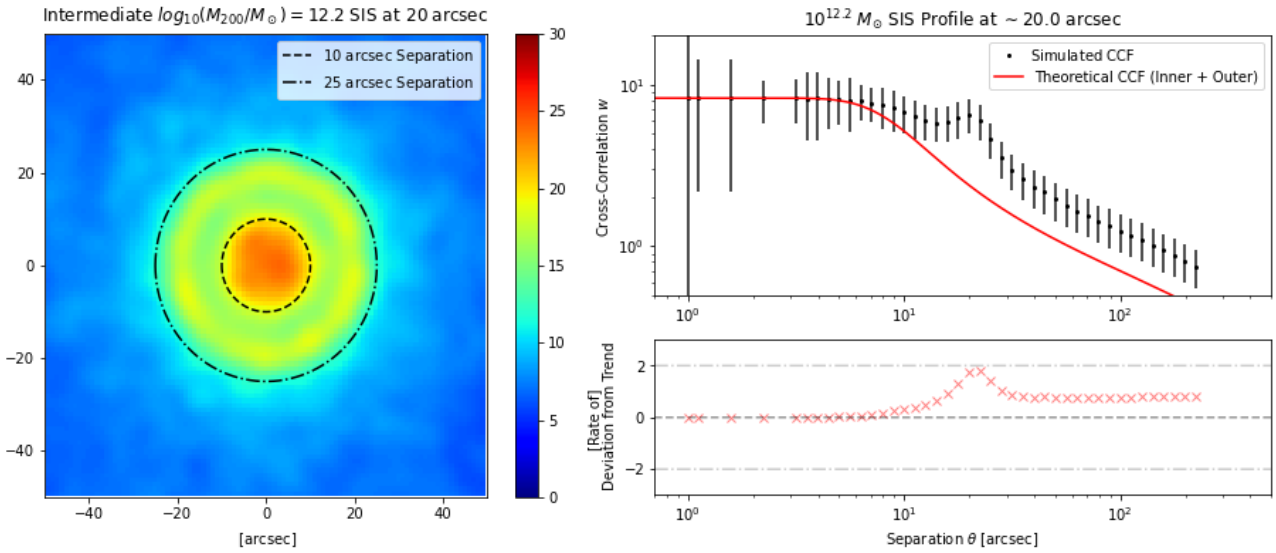

Figure 6.6: Left panel: Simulated map of counts for the case of a $10^{12.2}$ $M_\odot$ SIS third dark matter profile at ~ 20 arcsec. Right panel: Simulated CCF and deviation from the theoretical CCF created by the inner and outer terms alone.

We have seen that the maps of counts themselves shed light on the shape that could be expected in the CCFs. We show in the upper panel in figure 6.6 the map of simulated counts after magnification has taken place when a $10^{12.2}$ $M_\odot$ SIS profile has been put at ~ 20 arcsec.

[82] E.g. not aligned to the centre of the cluster.

[83] If the idea of overdensities of dark matter repeated at certain distances is good, the masses introduced cannot be too large. Particularly, it should not affect the total sum of masses combining the BCG and the cluster halo, so that a limit of $\sim 10^{13}$ $M_\odot$ for additional profiles should be set.

By eye, the election of $10^{12.2}$ $M_\odot$ for the additional profile produces something close to the desired effect in terms of a ring of *over*magnification preceded by a decrease in the number of counts just after 10 arcsec. The resulting CCF can be observed in the bottom panel, where a subplot has been added showing the deviation of the simulated CCF from the theoretical model created by the combination of the inner ($10^{13.4}$ $M_\odot$ NFW with $C = 10.0$) and outer ($10^{15.0}$ $M_\odot$ NFW with $C = 0.30$) profiles. The theoretical model, though, fails to reproduce statistical effects at great angular scales that separate both trends (making the simulated CCF higher than the theoretical model). The great number of simulated sources[84] (10^6 in $\pi \cdot 250$ px^2) was seemingly enough to make the strong lensing region invariable, producing a good fit as can be checked at low angular scales in the bottom right panel.

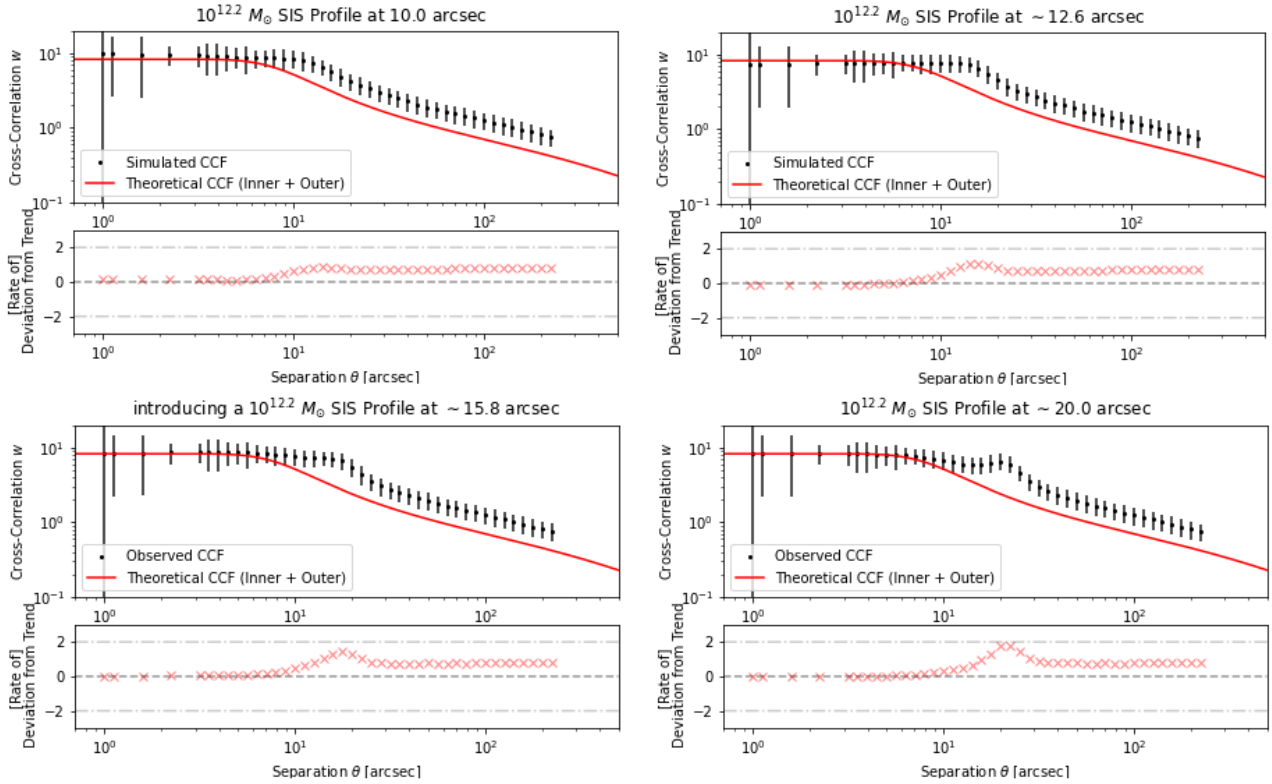

Figure 6.7: From left to right, first the upper row and then the bottom, the four cases for the location of an extra source at 10.0, ∼ 12.6, ∼ 15.8 and ∼ 20.0 arcsec respectively. We added the deviation from the theoretical trend made up by the combination of the inner and outer profiles ($10^{13.4}$ $M_\odot$ NFW with $C = 10.0$ and $10^{15.0}$ $M_\odot$ NFW with $C = 0.30$).

The radial distance we choose to place the extra profile makes an effect on the simulated CCF. To explore it, we show figure 6.7, where the four cases for the location of the SIS profile are displayed ($10^{1.0} \equiv 10$, $10^{1.1} \sim 12.6$, $10^{1.2} \sim 15.8$ and $10^{1.3} \sim 20.0$ arcsec). We can see that

[84]Note that the colour scale in the maps of counts reflects the density of sources per pixel, not per arcsec -this will be important soon when we compare the effect of different pixel scales in our ability to distinguish the gap and subsequent elevation in the CCF-.

as the distance from the centre of the cluster rises, the hill is better seen, although the gap is still imperceptible. The lack of agreement between the simulated trend and the standard theoretical model at great angular scales is always present.

Reflecting on what we knew of low mass SIS profiles, we see that the importance of the pixel scale is a major issue. Indeed, the ability to spot a clear gap depends much on whether the SIS profile gets to be resolved in a way that the $\mu \to 0$ effect is clear. To that end we have tried a similar case to the one above. We have modified the base of our simulation (the mass and concentration of the inner and outer profiles) to adapt to the obtained values by FER22 in its fourth bin of richness. On top of that, we have modified slightly the mass of the introduced SIS profile, to ensure that when the resolution is increased, the gap at $\sim$ 10 arcsec can be observed. With only lowering the pixel scale to 0.5 arcsec/px the presence of a the SIS-due demagnification zone is clear, as can be seen in the right panel in figure 6.8. It should be compared to the left panel in the same figure, where the standard pixel size (1 arcsec/px) has been used. Note that the overall simulated region is the same from a physical point of view (250 round arcsecs); apart from that, an adjustment in the number of simulated sources was undertaken to ensure that the density of sources per pixel is kept (and thereby the colour scale).

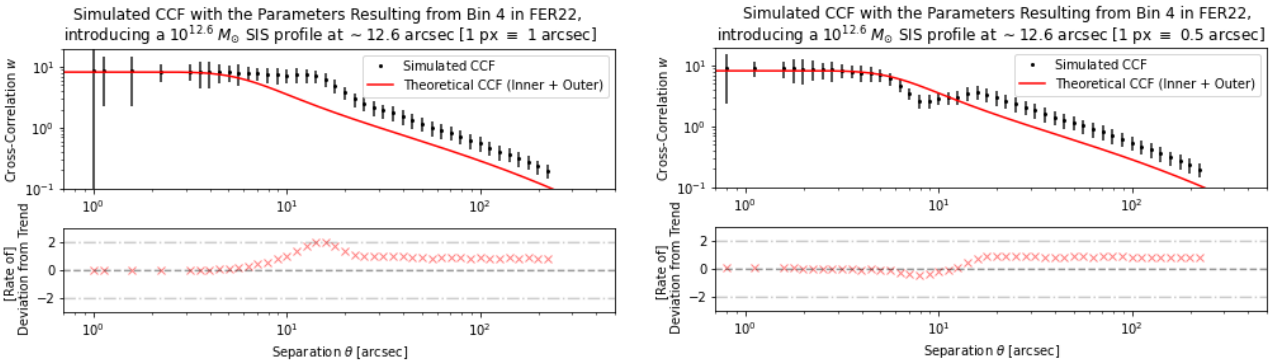

Figure 6.8: Simulated CCF and theoretical model built up from the parameters obtained by FER22 in their fourth bin of richness as inputs for the mass and concentration. In the left panel the case for a pixel size of 1 arcsec/px, at the right for 0.5 arcsec/px.

When the pixel size is not small enough to achieve a good resolution at the closest angular scale around the position the SIS profile has been placed, the gap in the CCF is lost (as can be observed in the left panel). Once the resolution is high enough, the gap becomes clear. From the deviation panels we see that the enhancement in the trend after the gap (check the right panel) is somewhat less obvious, and can be confused with the aforementioned discrepancy between the theoretical model and the simulated CCF at great angular scale. In appendix C the maps of counts (figure C.10) used to create the CCFs in figure 6.8 can be checked.

We have seen that just a single extra SIS profile is not enough to reproduce all of the features that we have seen in the observed CCFs by FER22. However, it serves as a basis for the review that will be made regarding one of the bins of richness that FER22 used to divide their samples of data. The former discussion about pixel scales will become less relevant, since by adapting to their criteria, it will be fixed to the standard case (1 arcsec/px).

6.2 Reviewing Bin 4 of Richness from Fernández et al. 2022 [1]

Finding a gap in the CCF at certain angular distances is a challenge that motivates complex ideas about compound profiles and theoretical functions for the fit. What is presented in the following lines is a new model in which we have tried to *fix* the one used previously -an outer profile and an inner profile- with a composition of profiles replacing the outer one. We decided to keep the inner profile fixed because the behaviour of the observed CCF at low angular scale is quite well described by the model, indeed our region of interest in the current section is at $\theta > 10$ arcsec.

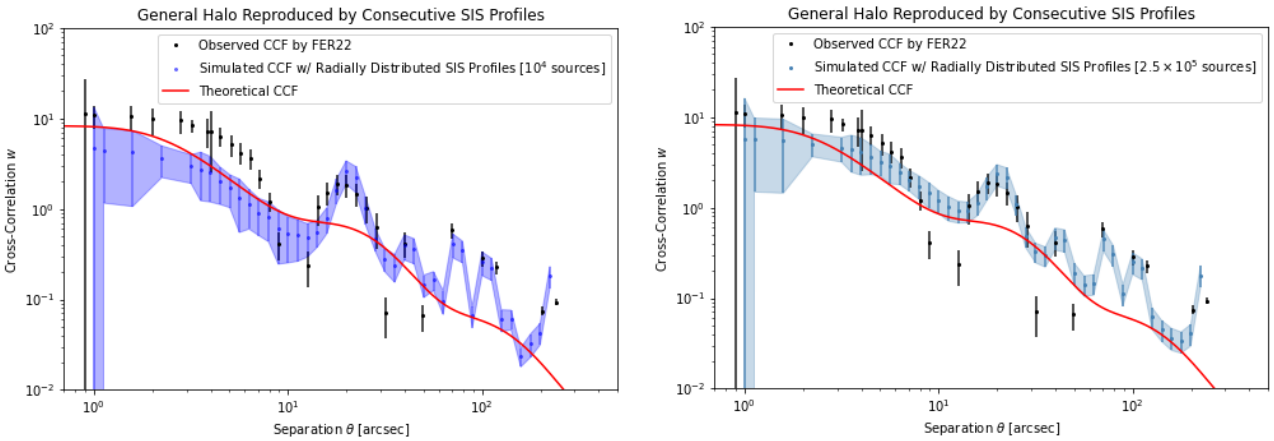

Figure 6.9: In black, the observed CCF by FER22 for their fourth bin of richness. In blue, our simulations with maps of magnification created with a sequence of SIS profiles placed at 20, 40, 70, 100 and 210 arcsec respectively. In the left panel, the result for a simulation with 10^4 sources represented in the map of counts -which is enough to produce a picture that is similar in scattering of dense spots similar to the *Total* bin by FER22. At the right, a simulation with 2.5×10^5 sources, enough to produce a good resemblance to the observed trend by FER22.

We introduced as many SIS profiles as *hills* could be spotted by eye in their measured CCF (black trend in figure 6.9). Code 7 (appendix B) was used to produce the radial magnification function; where a total of **five** SIS profiles were introduced. The virial masses of the profiles were $10^{12.0}$, $10^{11.3}$, $10^{11.5}$, $10^{10.7}$ $M_\odot$; at angular distances of 20, 40, 70, 100 and 210 arcsec respectively. Note that the angular scales make a good resemblance to what is expected for the

typical (possibly somewhat short) separation between galaxies in clusters. The virial masses used also resemble the typical masses expected for mean to big sized galaxies. We can see that an increase in the number of sources simulated (e.g. right panel) only improves the fit a low angular scales ($\lesssim$ 10 arcsec), where the BCG should be located. There, a plateau-like behaviour can be observed at a height of around $\sim$ 8.26 -the function used for distributing sources is described by a lower cut-off at 10 mJy-. We represented as well in a red solid line the theoretical description of the compound profiles, which is much smoother than both the observed (black) and simulated (blue) CCFs.

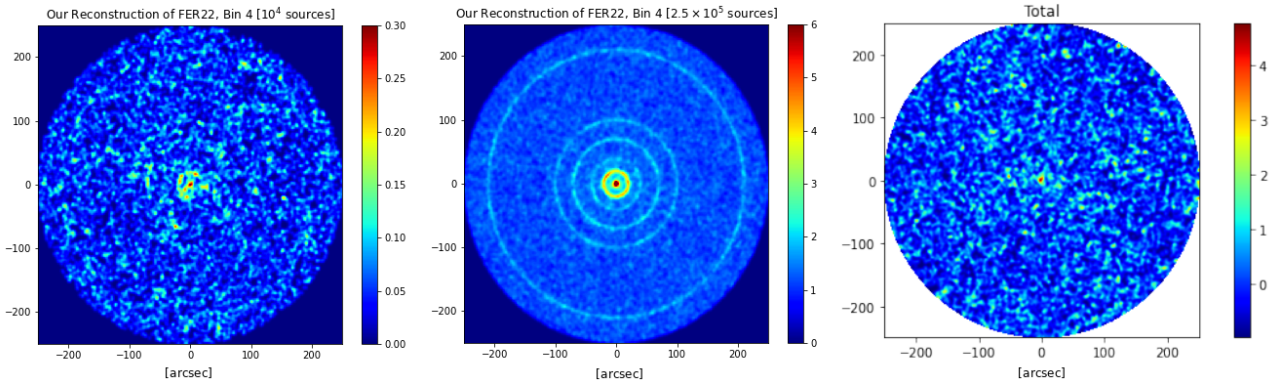

Figure 6.10: Comparison of the simulated maps of counts (10^4 sources at the left and 2.5×10^5 sources in the central panel) with the total case observed by FER22 (right panel here; top panel from figure 2 of the paper). The total case from FER22 is the result of having added up together all the objects from all bins of richness. A visual idea of how scattered overdensities raise naturally with small amounts of sources is what is intented with this representation.

The number of background sources (counts) in the fourth bin of richness is much smaller than 10^4. A test with the same number of sources used by FER22, which is detailed in the first table of their paper, is performed in the left panel in figure 6.11. The results in terms of measured CCF in that case can be observed in figure 6.12 as the green tendency. The central panel in figure 6.10 shows *rings* of overdensity due to the large amount of data. However, according to the simulated CCFs in figure 6.9, that a trend can already be observed in the maps of counts does not need to mean that the absence of it does not translate into a similar shape of the simulated/observed CCF. Indeed, at $\gtrsim$ 10 arcsec both panels in figure 6.9 behave similarly, even though they are built up from perceptibly different maps (the two at the left in figure 6.10 respectively). Note that any of our maps of counts may differ in the colour scale with the ones from FER22, due to they having chosen a normalised map. Even their own maps change the colour scale, not to mean that the number of sources expected in high-concentration pixels change accordingly to it, but due to the effect of the normalisation. For example, from panel 6.10 right to panel 6.11 right their colour scale also changes since there are much more sources

in the first case, so due to the choice of normalisation that scale is lower than that of the latter panel.

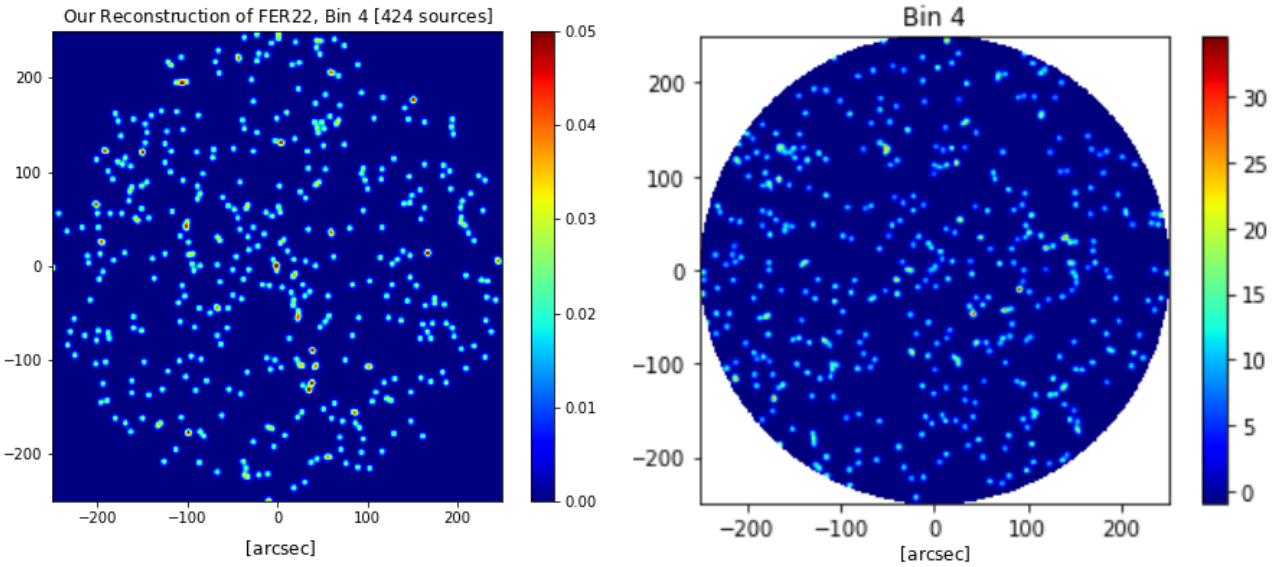

Figure 6.11: Attempt of reproducing the map of counts offered by FER22 (right panel here, bottom panel from figure 3 in that paper) for their fourth bin of richness by simulating the same number of sources as they did (left panel). A total of 424 sources were displayed, and we can see that both maps are quite similar to one another.

The simulated CCF with the same number of sources used by FER22 in their fourth bin of richness produced a fluctuating CCF that is much different from the observed one than when a greater number of sources was displayed. However, the main features (gaps and hills in the tendency) were still seen.

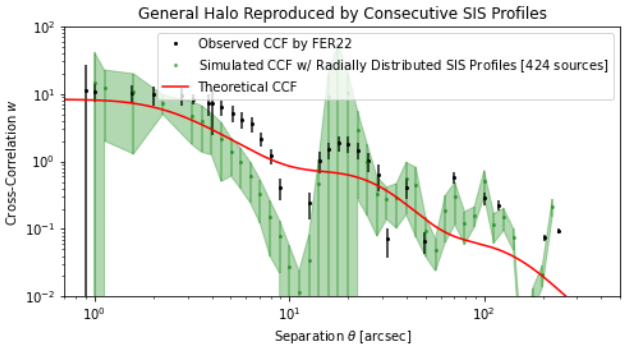

Figure 6.12: Observed CCF of the fourth bin of richness compared to our simulation with the same number of sources used there.

This little study has offered us another view on the reasons behind the pattern of gaps and hills observed and commented in FER22, which is also present in previous works, as they explicitly mentioned in the paper. The results obtained here can point to preferred locations in the concentration of dark matter in clusters from the central BCG, not meaning that every single cluster has concentric shells of dark matter concentration but rather a number of galaxies situated at certain distances.

7 Conclusions

A gathering of the most important ideas derived from the work above is presented below. We address all the knowledge that we have gain through our study, covering essentially sections 5 and 6.

The reduced Toy Model of section 5.1 served to understand how the profile-dependent magnification functions make an effect in the maps of counts of background galaxies situated in the plane of the deflector on the celestial sphere. We were able to differentiate the parts of the magnification function qualitatively by checking the regions where only one type of profile magnified sources (e.g. right panel of figure 5.7). We discovered that the amount of sources simulated per area is an important number to take into account. For instance, in a 10^{14} $M_{\odot}$ SIS-profile simulation the fall due to the demagnification region would be perceived in the observed CCF if $\gtrsim 10^5$ sources were simulated. Note that in later studies (sections 5.2 and 6), 10^6 sources is a standard value in the simulation unless the use of another number of sources is commented.

In the second part of the Toy Model, we learnt that the effect of applying a Gaussian filter to the maps of counts (e.g. figure 5.18) translates into a smoothing of the observed CCFs, which can be then followed with a theoretical fit by just performing a fit over the CCF + plateau functions (e.g. figure 5.19). The discovery of the flat behaviour itself in the strong lensing region -what we have called plateau- is a huge advancement of this work. If a great resolution can be obtained in the future some knowledge about the flux distribution of particular families of sources can be obtained from the plateau of the observed CCFs themselves.

The last test of our simulator had to do with the variability of the CCF if sources are distributed realistically with physical parameters. Namely we tested distributions of redshift (for both samples), virial mass of the deflector and its concentration (when applicable, NFW). Since the outcome of parameters (virial mass and concentration) was in line with previous studies with fixed parameters and the shapes of the simulated CCFs showed no big differences, we could say that working with sources that vary slightly on those parameters is perfectly acceptable. We could say as well that a richness tomography of the foreground sample of clusters is a good tool in order to inspect particularities in each bin. As a downside, we should left clear that the uncertainties returned by our fit programmes were not satisfactory enough so as to say that a precision-level measurement of parameters is possible.

Then, we started with the main issue of the work: simulating compound profiles and seeing how them could serve to understand better the observed CCFs obtained by FER22. As a preliminary result we observed that a hand-made fitting program was able to distinguish between different types of profiles. Then we built up double magnification functions and simulated compound CCFs, learning that a hard angle in the observed CCF prompts the beginning of a region with a sharply different concentration parameter. After testing the simulator several times, we discovered that this parameter is essential when accounting for the slope of the CCF.

Analysing the best model to build the magnification function we discovered that seemingly different results can be obtained if the theoretical model used for the fit is a compound function calculated as indicated in equations (6.2) and (6.3), or we used a local fit with simple profiles for each part. The latter method would require an additional function to separate the general halo term from the BCG term. When a fitting programme was run in order to return parameters such as the virial mass and the concentration, we saw that the choice of the input seed was relevant, leading to different outcomes. This could indicate some level of degeneracy on the parameters. We were estimating four parameters at the time.

The last step in our analysis of compound profiles led us to investigate the ~ 10 and ~ 25 arcsec gaps in the CCF observed by FER22. As a first attempt we tried to reproduce the gap with the demagnification region that a SIS profile for the general halo would impose in the CCF. Our conclusion was that this view is mostly flawed in several ways. Firstly, a SIS profile of $\gtrsim 10^{14}\ M_{\odot}$ creates a strong lensing region at great angular scales that is non-physical. However, we succeeded in finding a drop in the CCF at the wanted scale (~ 10 arcsec). Apart from that, a SIS profile of that size creates a vast regions of demagnification and strong lensing, much different from what we saw at great angular scales ($10 - 200$ arcsec) in FER22. Actually, the results of the paper indicate more of a cyclic pattern that is incompatible with such huge-mass SIS profile. As a more realistic way to tackle the issue, we recovered the inner and outer halo terms by FER22 but included a low-mass SIS magnification profile at the commented angular scale so that somehow a demagnification region was introduced at limited angular scales. We studied different masses and profiles and the result was a much more precise enhancement and gap -although the latter was harder to spot-. Indeed, we observed that the pixel scale was determinant in this case, as low-mass SIS profiles show demagnification in the number of counts only when the pixel size is small enough.

Those results were not satisfactory enough, and still the maps of counts that we observed

prior to simulating CCFs showed vastly different shapes and distributions than those from the original papers. Therefore, when reviewing the fourth bin of richness by FER22, where consecutive repetitions of gaps and hills were observed in the CCFs, we adopted a new method consisting on replacing the outer halo by a series of compound low-mass SIS profiles to reproduce the observed CCF (check again figure 6.9). Additionally, we saw that the right choice of the amount of sources distributed could reproduce well the maps observed by FER22. Results were mostly satisfactory in this part. SIS profiles of mass in order to what is expected for typical galaxies ($\sim 10^{11} - 10^{12}\ M_{\odot}$) were found to cover well most of the tendency, at any spotted oscillation in the larger angular scale ($\gtrsim 10$ arcsec). The physical interpretation of it is somewhat open, though. One idea is that there are preferred locations (or distances) for non-central (e.g. not BCGs) within clusters. This means that when one puts all the sample of clusters together, there are overdensities of counts at certain rings after stacking has taken place. One does not expect a clear pattern of shells of galaxies concentric to the cluster halo centre in the real world as a general model, but maybe two or three galaxies in each cluster at preferred distances. When stacking is performed, an overdensity could in such case be observed. When we say *observed* we refer to the CCF at least, since explicit rings of counts overdensities are only expected in maps if a huge (non real) number of sources constitute our samples.

Further tests should be developed comparing the results at other bins of richness in order to see how much the virial masses can vary. Also, in other bins, FER22 found a reasonable good fit by an outer NFW profile. For that reason, there is also a need to see how a combination of both a general outer NFW profile and low mass SIS profiles improves the fit. As a final comment, our simulator offers a wide range of opportunities for inspecting WGL-due magnification bias on differnt aspects. From the distribution of fluxes of the background sample to the most addressed properties of clusters and foreground objects, our simulator has been capable of producing interesting alternatives to shed light on some yet unexplained features.

References

[1] Fernández L. et al. "Galaxy cluster mass density profile derived using the submillimetre galaxies magnification bias". In: *Astronomy and Astrophysics* 658, A19 (2022). DOI: 10.1051/0004-6361/202141905. URL: https://doi.org/10.1051/0004-6361/202141905.

[2] Dyson F. W.; Eddington A. S. & Davidson C. "A determination of the deflection of light by the Sun's gravitational field, from observations made at the total eclipse of May 29, 1919". In: *Philosophical Transactions of the Royal Society* 220, Issue 571-581 (1920), pp. 291, 333. DOI: 10.1098/rsta.1920.0009. URL: https://royalsocietypublishing.org/doi/10.1098/rsta.1920.0009.

[3] *Hubble Space Telescope*. ESA/Hubble & NASA, 2011. DOI: https://www.nasa.gov/mission_pages/hubble/main/index.html.

[4] de Swart J. G.; Bertone G. & van Dongen J. "How dark matter came to matter". In: *Nature Astronomy* 1, A0059 (2017). DOI: 10.1038/s41550-017-0059. URL: https://doi.org/10.1038/s41550-017-0059.

[5] Bucklin S. M. *A history of dark matter*. Ars Technica, 2017. URL: https://arstechnica.com/science/2017/02/a-history-of-dark-matter/ (visited on 06/17/2022).

[6] Trojanowski S. Roszkowski L. Sessolo E. M. "WIMP dark matter candidates and searches: current status and future prospects". In: *Reports on Progress in Physics* 81, 6 (2018). DOI: 10.1088/1361-6633/aab913. URL: https://iopscience.iop.org/article/10.1088/1361-6633/aab913.

[7] Marsh D. J. E. "Axion Cosmology". In: *Physics Reports* 643, 6 (2016), pp. 1–79. DOI: 10.1016/j.physrep.2016.06.005. URL: https://doi.org/10.1016/j.physrep.2016.06.005.

[8] Sachs M. (on behalf of the original author). *File:Gravitational-lensing-3d.png - Wikimedia Commons*. Wikimedia Commons, 2008. URL: https://commons.wikimedia.org/wiki/File:Gravitational-lensing-3d.png (visited on 06/17/2022).

[9] Bonavera L. et al. "QSOs sigposting cluster size halos as gravitational lenses: halo mass, projected mass density profile and concentration at $z \sim 0.7$". In: *Journal of Cosmology and Astroparticle Physics* (2019). DOI: 10.1088/1475-7516/2019/09/021. URL: https://iopscience.iop.org/article/10.1088/1475-7516/2019/09/021.

[10] Aghanim N. et al. (the Planck Collaboration). "Planck 2018 results". In: *Astronomy and Astrophysics* 641, A6 (2020). DOI: 10.1051/0004-6361/201833910. URL: https://doi.org/10.1051/0004-6361/201833910.

[11] Bonavera L. et al. "Cosmology with the sumbillimetre galaxies magnification bias: Proof of concept". In: *Astronomy and Astrophysics* 639, A128 (2020). DOI: 10.1051/0004-6361/202038050. URL: https://doi.org/10.1051/0004-6361/202038050.

[12] González-Nuevo G. J. et al. "Cosmological constraints on the magnification bias on submillimetre galaxies after large-scale bias corrections". In: *Astronomy and Astrophysics* 646, A152 (2021). DOI: 10.1051/0004-6361/202039043. URL: https://www.aanda.org/articles/aa/full_html/2021/02/aa39043-20/aa39043-20.html.

[13] Bonavera L. et al. "Cosmology with the submillimetre galaxies magnification bias. Tomographic analysis". In: *Astronomy and Astrophysics* 656, A99 (2021). DOI: 10.1051/0004-6361/202141521. URL: https://doi.org/10.1051/0004-6361/202141521.

[14] González-Nuevo G. J. et al. "H-ATLAS/GAMMA: magnification bias tomography. Astrophysical contraints above $\sim$ 1 arcmin". In: *Journal of Comology and Astroparticle Physics* (2017). DOI: 10.1088/1475-7516/2017/10/024. URL: https://doi.org/10.1088/1475-7516/2017/10/024.

[15] Ryden B. *Introduction to Cosmology*. Cambridge University Press, 2017.

[16] Pettini M. *Introduction to Cosmology, Lectures*. Cambridge University, 2018. URL: https://people.ast.cam.ac.uk/~pettini/Intro%5C%20Cosmology/ (visited on 04/22/2022).

[17] Carroll S. *An Introduction to General Relativity: Spacetime and Geometry*. Addison Wesley, 2004.

[18] Soares D. S. L. "Newtonian gravitational deflection of light revisited". In: *arXiv* (2009). DOI: 10.48550/arXiv.physics/0508030. URL: https://doi.org/10.48550/arXiv.physics/0508030.

[19] Narayan R. & Bartelmann M. "Letures on Gravitational Lensing". In: *arXiv* (1997). DOI: 10.48550/arXiv.astro-ph/9606001. URL: https://doi.org/10.48550/arXiv.astro-ph/9606001.

[20] Shuntov M. *Cosmic Magnification in COSMOS*. June 2019. DOI: 10.13140/RG.2.2.20374.19523.

[21] Bartelmann M. & Schneider P. "Weak gravitational lensing". In: *Physics Reports* 340, Issues 4-5 (2001), pp. 291–472. DOI: 10.1016/S0370-1573(00)00082-X. URL: https://doi.org/10.1016/S0370-1573(00)00082-X.

[22] Bonavera L. et al. "Cosmological and astrophysical results exploiting magnification bias with high-z sub-millimetre galaxies". In: *arXiv* (2022). DOI: 10.48550/arXiv.2112.02959. URL: https://doi.org/10.48550/arXiv.2112.02959.

[23] González-Nuevo G. J. et al. "Herschel-ATLAS/GAMA: SDSS cross-correlation induced by weak lensing". In: *Monthly Notices of the Royal Astronomical Society* 442 (2014), pp. 2680–2690. DOI: 10.1093/mnras/stu1041. URL: https://doi.org/10.1093/mnras/stu1041.

[24] Poglitsch A. et al. "The Photodetector Array Camera and Spectrometer (PACS) on the Herschel Space Observatory". In: *Astronomy and Astrophysics* 518, L2 (2010). DOI: 10.1051/0004-6361/201014535. URL: https://www.aanda.org/articles/aa/full_html/2010/10/aa14535-10/aa14535-10.html.

[25] Lapi A. et al. "Herschel-ATLAS galaxy counts and high-redshift luminosity functions: the formation of massive early-type galaxies". In: *The Astrophysical Journal* 742, 24 (2011). DOI: 10.1088/0004-637X/742/1/24. URL: https://iopscience.iop.org/article/10.1088/0004-637X/742/1/24.

[26] Pilbratt G. L. et al. "Herschel Space Observatory - An ESA facility for far-infrared and submillimetre astronomy". In: *Astronomy and Astrophysics* 518, L1 (2010). DOI: 10.1051/0004-6361/201014759. URL: https://www.aanda.org/articles/aa/full_html/2010/10/aa14759-10/aa14759-10.html.

[27] Poglitsch A. et al. "The Herschel-SPIRE instrument and its in-flight performance". In: *Astronomy and Astrophysics* 518, L3 (2010). DOI: 10.1051/0004-6361/201014519. URL: https://www.aanda.org/articles/aa/full_html/2010/10/aa14519-10/aa14519-10.html.

[28] Ross N. P. et al. "The SDSS-III Baryon Oscillation Spectroscopic survey: Quasar target selection for data release nine". In: *The Astrophysical Journal* 199, 3 (2012). DOI: 10.1088/0067-0049/199/1/3. URL: https://iopscience.iop.org/article/10.1088/0067-0049/199/1/3.

[29] Bianchini F. et al. “Broadband Spectral Energy Distributions of SDSS-selected Quasars and of Their Host Galaxies: Intense Activity at the Onset of AGN Feedback”. In: *The Astrophysical Journal* 871, 136 (2019). DOI: 10.3847/1538-4357/aaf86b. URL: https://iopscience.iop.org/article/10.3847/1538-4357/aaf86b.

[30] Wen Z. L. et al. “A Catalog of 132,684 Clusters of Galaxies Identified from Sloan Digital Sky Survey III”. In: *The Astrophysical Journal* 199, 34 (2012). DOI: 10.1088/0067-0049/199/2/34. URL: https://iopscience.iop.org/article/10.1088/0067-0049/199/2/34.

[31] Davis M. & Peebles P. J. E. “A survey of galaxy redshifts. V. The two-point position and velocity correlations”. In: *The Astrophysical Journal* 267 (1983), pp. 465–482. DOI: 10.1086/160884. URL: https://ui.adsabs.harvard.edu/abs/1983ApJ...267..465D.

[32] Landy S. D. & Szalay A. S. “Bias and Variance of Angular Correlation Functions”. In: *The Astrophysical Journal* 412 (1993), pp. 64–71. DOI: 10.1086/172900. URL: https://ui.adsabs.harvard.edu/abs/1993ApJ...412...64L.

[33] Sparke L. S. & Gallagher J. S. *Galaxies in the Universe: An Introduction*. Cambridge University Press, 2007.

[34] Navarro J. F.; Frenk C. S. & White S. D. M. “Letures on Gravitational Lensing”. In: *arXiv* (1997). DOI: 10.48550/arXiv.astro-ph/9606001. URL: https://doi.org/10.48550/arXiv.astro-ph/9606001.

[35] Mandelbaum R. et al. “A Halo Mass-Concentration Relation from Weak Lensing”. In: *Journal of Cosmology and Astroparticle Physics* (2008). DOI: 10.1088/1475-7516/2008/08/006. URL: https://iopscience.iop.org/article/10.1088/1475-7516/2008/08/006.

[36] Papovich C. et al. “Spitzer Mid- to Far-Infrared Flux Densities of Distant Galaxies”. In: *The Astrophysical Journal* 668, 45 (2007). DOI: 10.1086/521090. URL: https://iopscience.iop.org/article/10.1086/521090.

[37] White M. “The Mass of a Halo”. In: *Astronomy and Astrophysics* 367 (2001), pp. 27–32. DOI: 10.1051/0004-6361:20000357. URL: https://doi.org/10.1051/0004-6361:20000357.

[38] Bourne N. et al. “The Herschel-ATLAS Data Release 1 – II. Multi-wavelength counterparts to submillimetre sources”. In: *Monthly Notices of the Royal Astronomical Society* 462, Issue 2 (2016), pp. 1714–1734. DOI: 10.1093/mnras/stw1654. URL: https://doi.org/10.1093/mnras/stw1654.

[39] Smith D. J. B. et al. “Herschel–ATLAS: counterparts from the ultraviolet–near-infrared in the science demonstration phase catalogue”. In: *Monthly Notices of the Royal Astronomical Society* 416, Issue 2 (2011), pp. 857–872. DOI: 10.1111/j.1365-2966.2011.18827.x. URL: https://doi.org/10.1111/j.1365-2966.2011.18827.x.

[40] Maddox S. J. et al. “The Herschel-ATLAS Data Release 2. Paper II. Catalogs of Far-infrared and Submillimeter Sources in the Fields at the South and North Galactic Poles”. In: *The Astrophysical Journal Supplement Series* 236:30 (2018). DOI: 10.3847/1538-4365/aab8fc. URL: https://iopscience.iop.org/article/10.3847/1538-4365/aab8fc.

[41] Weinberg N. N. & Kamionkowski M. “Constraining dark energy from the abundance of weak gravitational lenses”. In: *Monthly Notices of the Royal Astronomical Society* 341, Issue 1 (2003), pp. 251–262. DOI: 10.1046/j.1365-8711.2003.06421.x. URL: https://doi.org/10.1046/j.1365-8711.2003.06421.x.

[42] Coe D. et al. “High-Resolution Mass Map of Galaxy Cluster Substructure: Lensperfect Analysis of A1689”. In: *The Astrophysical Journal* 723 (2010), pp. 1678–1702. DOI: 10.1088/0004-637X/723/2/1678. URL: https://iopscience.iop.org/article/10.1088/0004-637X/723/2/1678.

[43] Clowe D. et al. “Weak-Lensing Mass Reconstruction of the Interacting Cluster 1E 0657–558: Direct Evidence for the Existence of Dark Matter”. In: *The Astrophysical Journal* 604 (2004), pp. 596–603. DOI: 10.1086/381970. URL: https://iopscience.iop.org/article/10.1086/381970.

A Extra Theoretical Notes

This appendix is dedicated to a further insight into theoretical cosmology. In section 2 we had introduced the FLRW metric -equation (2.1)- and the evolution of the Hubble parameter with the redshift -equation (2.3)-. Going from the former to the latter requires some more equations (the Friedmann equations and the equations of state for different types of matter) and quite of an extended theoretical path. Actually, there are two ways that actually match each other; one can work with newtonian dynamics -allowing for a magical expansion of space parameterised by the scale factor $a(t)$- with a helping hand of thermodynamics or can derive -preferentially with a computer programme- the Einstein equations in the framework of General Relativity. Nicely, one arrives to the same point after both derivations. All of that is covered in the first two subsections from this appendix, where we are going to use as references the notes by Prof. Pettini [16] and Ryden's book [15].

When in section 4.3 we say that the profiles are parameterised by the mass of the cluster -or the deflector in a general way- we have to assess the extension of the object, which is not a trivial issue at all. Only when we talk about compact objects -let's put the Earth- we know with high precision its size or mass. Earth has a mass contained within its surface or order 10^{24} kg; its atmosphere is only a tiny fraction of that order in mass, $\sim 10^{18}$ kg. For most purposes a change in the sixth significant number of the mass of the Earth is completely irrelevant, so one typically stays with the relevant mass order.

Non compact objects require a virial treatment instead, which we are going to follow from Sparke and Gallagher's book [33]. For cosmological purposes one calculates the mass of galaxies and clusters thanks to the observed velocities of objects within them. As a matter of fact there is few other ways to detect the presence of dark matter but by exclusion of the observed baryonic mass from the needed virial mass of bound objects, calculated to match the velocity of substructures there contained.

A.1 Cosmological Parameters (I): Newton's Mechanics with a Some Concepts from Cosmology

Classical Cosmology is enough to arrive to the first Friedmann Equation and the fluid equation, without resorting to General Relativity. One has to consider, though, that it is possible that space gets stretched with time. Moreover, at some point we will have to use some *magic*

to arrive at some concepts such as curvature or energy[85] density. Actually it is not magic, but rather that we have used an ANSATZ from the general relativistic derivation.

The existence of a scale factor does not go against any prerequisite demanded by classical mechanics axioms, but it is an input, nevertheless. In General Relativity there is no need either for it, but since one of the wonders of General Relativity is that you can write the craziest metric imagined and work with it, a simple metric as that of FRLW with a scale factor $a(t)$ seems quite natural.

In any case, starting with a classical derivation requires contemplating Brikhoff's theorem (see figure A.1) to understand that what might change the size of a sphere -to be thought as the whole universe- is the matter within[86] it. We can write Newton's second law of motion for the radius $R_s(t)$ of that sphere -eq. (A.1)-, knowing that $R_s(t)$ has to be a comoving radius r_s -which does not evolve with time- and a scale factor $a \equiv a(t)$. It is here where the first typically related general relativistic term appears: the scale factor.

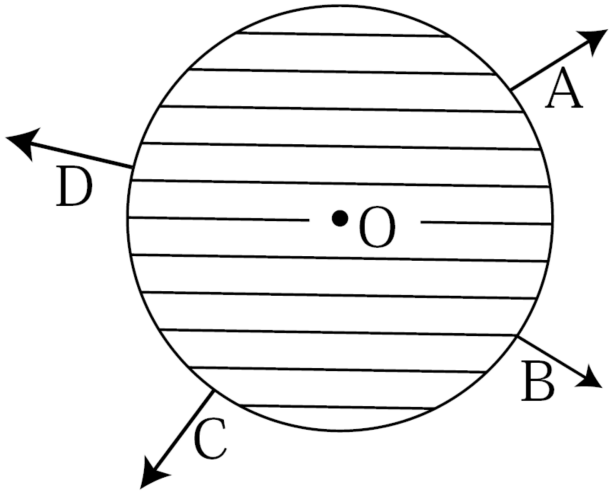

Figure A.1: Grapical representation of Birkhoff's theorem, where particles situated at some points (A, B, C, D) on the surface of a sphere suffer a gravitational attraction that can be substituted by a single particle of mass equivalent to that of the whole sphere situated at its centre.

$$r_s^2 \ddot{a} = -\frac{GM_s}{r_s a} \tag{A.1}$$

Integrating and taking everything but the integration constant to the same side we obtain

$$U = T + V = \frac{r_s}{2}\dot{a}^2 - \frac{G\ M_s}{r_s\ a} \tag{A.2}$$

where the mass of the sphere M_s can be put as a function of a time dependent density $\rho \equiv \rho(t)$ and the radius: $M_s \propto \rho\ (r_s a)^3$. The **non-relativistic** counterpart of the first Friedmann

[85]Here is where the debate when defining ρ_i as the *energy* density of a certain fluid could be raised. Mass density is the only density known in classical mechanics when working with something defined as the mass of a gravitational attractor divided by some volume. But we would need to change that density for an energy density ϵ and divide by c^2 to find the density counterpart from general relativity, which is what is defined as energy density in that theory.

[86]Concepts from statistical mechanics are needed -as well as special relativity- to understand that *matter*, in this context, refers to *all that is contained*. The proper way to address it is with the concept of **cosmological fluid**.

equation is then found when we divide equation (A.2) by $(r_s a)^2$ and rearrange it slightly, having defined the Hubble parameter H as $\dot{a}/a$.

$$H^2 \equiv H^2(t) \equiv \left(\frac{\dot{a}}{a}\right)^2 = \frac{8\pi G}{3}\rho + \frac{2U}{r_s^2}\frac{1}{a^2} \tag{A.3}$$

Now, to access the general relativistic expression, we have to change[87] ρ by ϵ/c^2 and the factor[88] accompanying a^{-2} at the right-hand side of equation (A.3) by $-kc^2$.

$$H^2 \equiv H^2(t) \equiv \left(\frac{\dot{a}}{a}\right)^2 = \frac{8\pi G}{3c^2}\epsilon - \frac{kc^2}{a^2} \tag{A.4}$$

This is the **first Friedmann equation**. If we divide it by the Hubble parameter squared, so that at the left hand side of the equation we find a 1, we have created the density parameters Ω_U and Ω_k. We had talked about them in section 2 without having appropriately defined them. Now we do so, but remind that were the density parameters evolve with time.

$$1 = \frac{8\pi G}{3H^2}\epsilon - \frac{kc^2}{H^2 a^2} \equiv \frac{\epsilon}{\epsilon_c} + \Omega_k \quad \Rightarrow \quad \Omega_k = 1 - \Omega \tag{A.5}$$

Note that the ϵ_c defined in equation (A.5), as well as ϵ, are not the energy densities **today** we talked about in section 2 but time evolving energy densities. At the end of the equation we have defined the (evolving) density parameter for the curvature -we have used that choice of the sign in order to be coherent with the notation in equation (2.3)- so that the density parameters of the fluids within our universe and the spatial curvature induced density sum up 1. This way, if at present one finds that the $\Omega(t = \text{today})$ value is different from 1, we would live in a non-flat universe. Particularly, with our choice[89] of signs, a negative value of Ω_k means a closed universe $k = +1$ (cyclic in space), while a positive value of Ω_k means an open universe $k = -1$ (hyperbolic in space).

Now, we are interested in finding the **fluid equation**, for which it is enough to put the first law of thermodynamics in play. The heat transfer to the inside or outside of a volume is $d\mathcal{Q} = dE + P\ dV$, where dE is the change in the internal energy and P the pressure within that volume. Since we do not expect our universe to cede or gain any heat, we can put $d\mathcal{Q}$

[87] This is indeed the classic rest energy of an object in the special-relativistic framework $E = mc^2$.

[88] Well, that r_s should be treated more carefully and one could talk about the curvature radius of the universe in general-relativistic terms and have a quite extended physical debate. For our purposes we will simply say that we have chosen k with units of length^{-2}, so that the kc^2/a^2 remains with time^{-2} units, as it should to match the units of Hubble parameter.

[89] Matching Ryden's choice.

to 0. This means that we are working with an adiabatic universe. Differentiating with respect to time one finds $\dot{E} + P\ \dot{V} = 0$. Now, we do know the volume of the universe since it is the volume of the sphere we began with. Besides, the energy of the universe E can be written as the product of its volume by its energy density ϵ. This translates into

$$\dot{E} = -P\ \dot{V} \quad \Rightarrow \quad 3a^2\dot{a}\epsilon + a^3\dot{\epsilon} = -3Pa^2\dot{a} \quad \Rightarrow \quad 3\frac{\dot{a}}{a}(\epsilon + P) + \dot{\epsilon} = 0 \tag{A.6}$$

which is the fluid equation. It can be solved with the inclusion of a fluid equation. Moreover, note that since ϵ and $\dot{\epsilon}$ are the **total** energy density of the universe and its derivative, there is no problem in writing them as the sum of several fluids, e.g. $\epsilon \equiv \sum_i \epsilon_i$. This is, we do not need to know how the universe behaves as a whole, but knowing the fluids that make it up. It is customary in every introductory course to Cosmology to start here a discussion on the several models of universe available depending on the type of fluid that dominates. It is done in section 5.3 of Ryden's book and in the fourth lecture of Pettini's course, as it is extremely useful to understand the behaviour of the universe at the time when each type of fluid dominated its composition. However, we will only stop to describe the equations of state for each component, since our aim is to arrive to $H(z)$ expression in 2.3.

Counting the fluid equation and the first Friedmann equation we have 3 unknowns in a system of two differential equations. The unknowns are $\epsilon \equiv \epsilon(t)$, $a \equiv a(t)$ and $P \equiv P(t)$. But we had seen that $\{P, \epsilon\}$ are $\{P_i, \epsilon_i\}$ for each type of cosmic fluid i; and each of the fluids can be parameterised with a fluid equation that can be derived from statistical mechanics and be written in the form

$$P_i(\epsilon_i) = w_i\epsilon_i \tag{A.7}$$

Relativistic matter is characterised by a factor $w_{\rm rel} = 1/3$, cold matter by $w_{\rm m} = 0$ and dark energy by $w_\Lambda = -1$. The equation of fluid is deemed as a differential equation that relates a and ϵ, taking into account the information that we have acquired from state equations. The result is[90] that the energy density of every fluid will evolve with the scale factor, but each of them will do so in a particular way

[90]This is just as saying that each type of fluid does not talk to each other, which might not be true. Nicely, though, the mathematical part of this theory works perfectly well if we plug the result for each type of fluid (the $\epsilon_i(a, w_i)$ functions) into the fluid equation.

$$3\frac{\dot{a}}{a}\left(\sum_i \epsilon_i + \sum_i w_i\epsilon_i\right) + \sum_i \dot{\epsilon}_i = 0 \quad \Rightarrow \quad \frac{\dot{\epsilon}_i}{\epsilon_i} = -3\,(1+w_i)\,\frac{\dot{a}}{a} \quad \Rightarrow \quad \epsilon_i = \epsilon_{i,0}\; a^{-3(1+w_i)} \tag{A.8}$$

For relativistic matter this translates into $\epsilon_{\rm rad} \propto a^{-4}$, for cold matter into $\epsilon_{\rm m} \propto a^{-3}$ and for dark energy into $\epsilon_\Lambda = \epsilon_{\Lambda,0}$. This is, the energy density of the dark energy is expected to remain the same at any point in the history of our universe. Although it might not seem clear as it is written know, we have arrived to the end, we just need to plug equation (A.8) into the first Friedmann equation, but a special form of it. To get the result with the density parameters **today** -the ones we measure-, we need to divide the Friedmann equation by the Hubble constant -the value of the Hubble parameter today- squared H_0^2. The result is

$$E^2(a) \equiv \left(\frac{H}{H_0}\right)^2 = \frac{8\pi G}{3c^2H_0^2}\sum_i \epsilon_{i,0}a^{-3(1+w_i)} + \frac{kc^2}{a^2H_0^2} = \sum_i \Omega_{i,0}a^{-3(1+w_i)} + \Omega_{k,0}a^{-2} \tag{A.9}$$

The last step -to get to equations (2.3) and (A.11) from the previous expression- is just a simple question of redshift being the quantity that is convened in cosmology to measure distances. Also, since it has the easiest relation with respect to light's wavelength and frequency. It is defined as a function of the scale factor as

$$1 + z_{\rm obj} = \frac{a(t = \text{today}) \equiv 1}{a(t = t_{\rm em})} = \frac{\lambda_{\rm obs}}{\lambda_{\rm em}} = \frac{\nu_{\rm em}}{\nu_{\rm obs}} \tag{A.10}$$

where $z_{\rm obj}$ refers to the object's redshift, $\lambda_{\rm em}$ to light's wavelength from that object at the time it was emitted and $\lambda_{\rm obs}$ to that light's wavelength when it gets to us. Similarly for the frequencies ν. With the definition $z(a)$ we can substitute in equation (A.9) and obtain

$$\begin{aligned} E^2(z) =& \sum_i \Omega_{i,0}(1+z)^{3(1+w)} + \Omega_k(1+z)^2 \\ H(z) =& H_0\sqrt{\Omega_\Lambda + \Omega_{k,0}(1+z)^2 + \Omega_{\rm m,0}(1+z)^3 + \Omega_{\rm rad,0}(1+z)^4} \end{aligned} \tag{A.11}$$

A.2 Cosmological Parameters (II): Non-Stop Flight from FLRW to H(z)

One of the greatest things about general relativity is that one does not need to resort to extremely armed arguments or theorems such as Birkhoff's, nor making up that $U \propto k$ an

invented curvature of space-time. By the way, this would be quite a strange thought in the minds of classical physicists[91] before Einstein's special and general ways. The downside of General Relativity is that everything becomes a bit more boring when words are unneeded and all one requires is either a lot of time to work out Christoffels and Riemmans or a good computation programme.

The non-zero elements of the metric of FLRW (2.1) are

$$g_{tt} = -c^2 \ , \quad g_{rr} = \frac{a^2}{1-kr^2} \ , \quad g_{\theta\theta} = a^2 r^2 \ , \quad g_{\phi\phi} = a^2 r^2 \sin^2\theta \tag{A.12}$$

Once the computation programme has made its magic, one obtains the time-time and radial-radial components of the Einstein equations as the ones that are independent and non-zero. At the right-hand side of the traditional Einstein equations one finds a stress-energy tensor for the cosmological fluid, with components[92] those of (A.13). This time, though, as we have already introduced the cosmological constant before, we will just simply say that at the left-hand side. Adding to the Einstein tensor we will have a constant term multiplied by the metric $-\Lambda g_{\mu\nu}$, which is the natural way of introducing the cosmological constant as a scalar field theory in the Lagrangian of our theory.

$$\mathcal{T}_{tt} = \epsilon \ , \quad \mathcal{T}_{rr} = \frac{pa^2}{1-kr^2} \tag{A.13}$$

where p stands for the fluid's pressure. Einstein (A.14) equations[93] translate into the two Friedmann (A.15) equations

$$\mathcal{G}_{\mu\nu} = \frac{8\pi G}{c^4}\mathcal{T}_{\mu\nu} \ , \quad \begin{cases} G_{tt} = 3(ca)^{-2}(\dot{a}^2 + kc^2) = \frac{8\pi G}{c^4}\epsilon \\ \tilde{\mathcal{G}}_{rr} = -c^{-2}(2a\ddot{a} + \dot{a}^2 + k) = \frac{8\pi G}{c^4}p \end{cases} \tag{A.14}$$

$$\text{(I)} \quad H^2 = \left(\frac{\dot{a}}{a}\right)^2 = \frac{8\pi G}{3c^2}\epsilon - \frac{kc^2}{a^2} \qquad \text{(II)} \quad 2\frac{\ddot{a}}{\dot{a}} + \left(\frac{\dot{a}}{a}\right)^2 = -\frac{8\pi G}{c^2}p - \frac{kc^2}{a^2} \tag{A.15}$$

Subtracting from the second Friedmann equation the firs one, we obtain the acceleration equation. That is useful to see whether the universe expands faster or slower with time. With respect to finding $H(z)$, we have arrived to the same point as with equation (A.4) in the previous

[91] Why would our R^3 space be the surface of a four-dimensional sphere or hyperboloid?

[92] We only care about the time-time and the radial-radial ones.

[93] The $\tilde{\mathcal{G}}_{rr}$ equals $\mathcal{G}_{rr}$ but multiplied by the $(1+kr^2)$ factor from the radial-radial term of the metric. It was chosen so that the expression in (A.14) is clearer.

subsection. Now the rest of the path is the same as before. One needs both the fluid equation and some equations of state for the different types of cosmological fluids, and happily gets to equation (A.11)

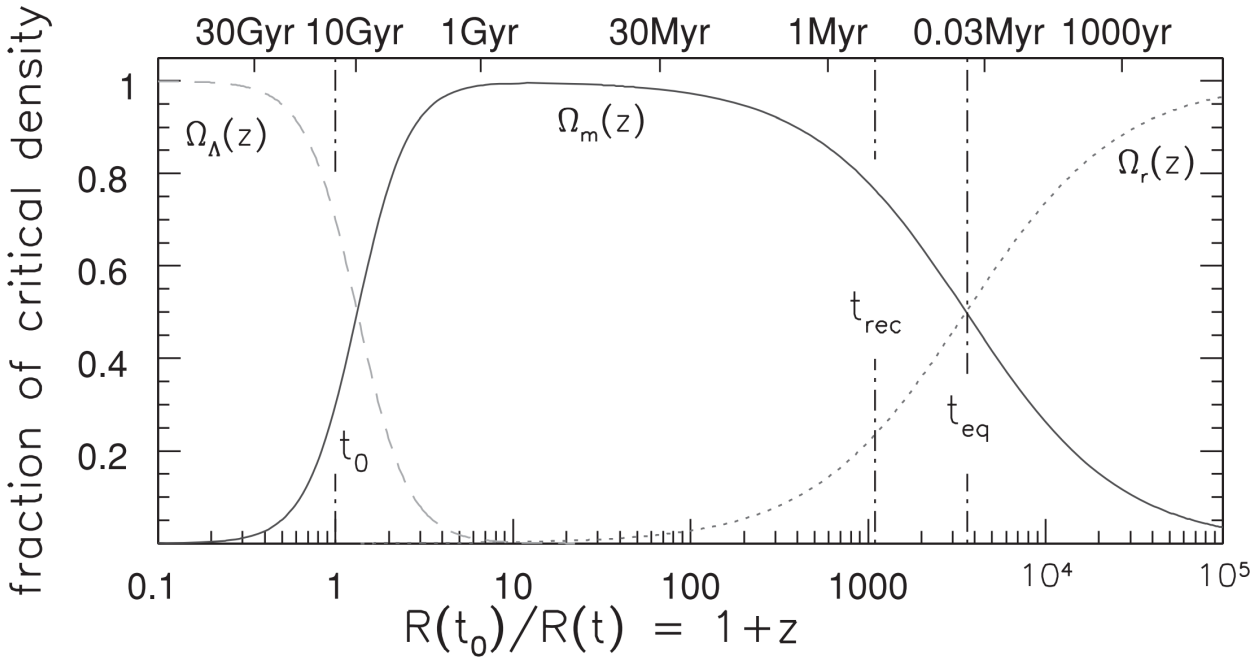

Figure A.2: Evolution of the density parameters with redshift. Figure 8.7 from Sparke and Gallagher 2007 [33]. The benchmark model takes $\Omega_{\Lambda,0} \sim 0.7$ and $\Omega_{m,0} \sim 0.3$.

A.3 Galaxies and Clusters are Bound

If dark matter was discovered and a direct way to detect it -other than gravitational need for it- was available, it would be easy to say that clusters of galaxies are gravitationally bound structures. Despite it not having happened, the fact that these kind of structures are common and some reconstructions of the mass density due to weak lensing phenomena with background sources of particular clusters helped us determine that these groups of galaxies are indeed gravitationally bound. Note that from galaxies and downwards in complexity, the timescale of phenomena showed enough variability in human standards so that structures could be classified

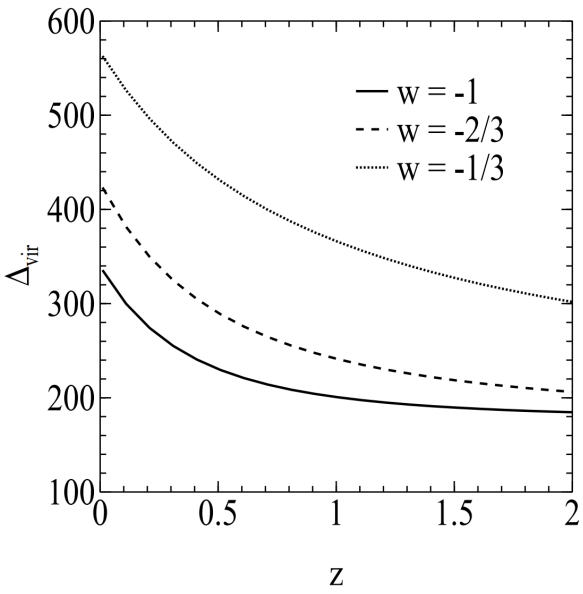

Figure A.3: Figure 3 from Weinberg & Kamionkowski 2003 [41]. Represented the evolution of the Δ_{vir} value with respect to redshift in the benchmark model.

as bound. The comprehensive reconstruction of the mass density of Abell 1689 by Coe et al. in 2010 [42] and the weak lensing contours of the Bullet Cluster by Clowe et al. 2004 [43] are but two examples of the rich literature studying the dark matter component of clusters.

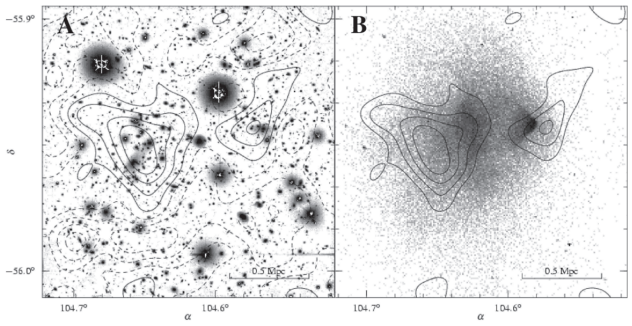

Figure A.4: Density levels of the region belonging to the known as Bullet Cluster; plots A and B from figure 1 in Clowe et al. 2004. The dark lines represent mass density contours levelling $2.8 \times 10^8\ M_\odot\ \mathrm{kpc}^{-2}$ in each step.

Our simulation requires an analytical description of dark matter models (NFW and SIS) that depend -particularly the first of them- on a notion of scale radius. It was define after equation (4.6) as the radio enclosing a region with $\rho > 200\rho_c(z)$ at the z of the bound object that is being studied. The critical density at which a region is considered gravitationally virialised is $\rho_{\rm vir} = \Delta_{\rm vir}\rho_c$, with $\Delta_{\rm vir}$ being quite a variable quantity. It depends on the type of cosmology used[94], but a standard value tends to be[95] $\Delta_{\rm vir} = 200$, so astrophysicists and cosmologists typically work with M_{200} and r_{200}. With the convention established, the mass we are using all throughout the work in general referring to the mass of the deflector is

$$M_{200} = \frac{800}{3}\pi r_{200}^3 \rho_c(z) \tag{A.16}$$

Since $\rho_c(z)$ is fully determined at known z, r_{200} and M_{200} are the same[96]. Remembering that r_s is a function of C and r_{200}, we can set $r_s \equiv r_s(M, C)$, so with the (virial) mass and concentration we can fully determine the NFW halo profile of a dark matter overdensity. However, the NFW profile can also be taken to be a one-parameter family by using the relation obtained from Mandelbaum et al. 2008 [35] (their equation (7) and surrounding text). This fact was taken into account, for example, by BON19; where they used

$$C(M_{200}, z) = \frac{4.6}{1+z}\left(\frac{M_{200}}{1.56 \times 10^{14} h^{-1}\ M_\odot}\right)^{-0.13} \quad \Rightarrow \quad NFW(C, M_{200}) \to NFW(M_{200}) \tag{A.17}$$

[94]This means, the numbers chosen for a ΛCDM model parameters in a non-precision level. For example, $\Delta_{\rm vir} = 200$ is used for $\Omega_{\rm m} = 1$ models (see White's 2001 paper [37].), which is notably far from the present status of the universe. Once upon a (long) time, $\Omega_{\rm m} \sim 1$ though. This happened after the first life forms already lived in Earth (!), at $z \sim 2$.

[95]We see from Weinberg & Kamionkowski 2003 [41] that $\Delta_{\rm vir} \approx 200$ works quite well in the benchmark model for $z \gtrsim 1$. See figure A.3.

[96]Just as $2.998... \times 10^8$ m equal 1 s at $c = 1$.

B Coding Lines

In this section the functions that make up the backbone of our work are displayed. Firstly, we introduce the functions that served to create the fluxes of the background sources and to calculate the plateau of the CCF. Then we move on to the functions that created the maps of counts. Finally, we address the functions that were used to calculate the observed CCFs and perform the fit with the theoretical (modified) CCFs.

The theoretical CCF functions that appear within the ones below -e.g. *get_xc_SIS* or *get_xc_NFW*- are provided in libraries provided by the supervisors. Essentially they reproduce the theoretical functions commented in section 4.3. The Jackknife analysis function was also provided by the supervisors and belonged to another library.

B.1 Random Fluxes

```
def rand_flux(Ns, hor, ver, Sn, Sx):
    from numpy import random, interp, hstack
    Sx = min(Sx, max(hor[ver * Ns > 0.01]))
    ver = ver[(hor >= Sn) & (hor < Sx)]
    hor = hor[(hor >= Sn) & (hor < Sx)]
    Nr = int(max((Ns * 3, 1e6)))
    x = Sn + (Sx - Sn) * random.rand(Nr)
    y = min(ver) + (max(ver) - min(ver)) * random.rand(Nr)
    y0 = interp(x, hor[::-1], ver[::-1])
    S = x[y < y0]
    if (S.size < Ns):
        while (S.size < Ns):
            x = Sn + (Sx - Sn) * random.rand(Nr)
            y = min(ver) + (max(ver) - min(ver)) * random.rand(Nr)
            y0 = interp(x, hor[::-1], ver[::-1])
            S = hstack((S, x[y < y0]))
        S = S[:Ns]
    else:
        S = S[:Ns]
    return 10 ** S
```

Listing 1: Function used for the generation of random fluxes. It uses input variables *hor* and *ver* that come from another function named *counts* provided by the supervisors.

```
def cuantosN0(N, Sn, LIM):#PXlim == maxarcsec/ratio [ratio]==arcsec/pixel, [LIM]==Jy, [Sn]==log_10(Sn) (NEGATIVO)
    from numpy import isnan, log10
    hor, ver = counts(857, 'lapi11')
    ver[isnan(ver)] = 1e-20
    mn = log10(10**(Sn))
    Mx = log10(100)
    arrayf = rand_flux(N, hor, ver, mn, Mx)
    testi = 0
    N0_supS = 0
    while testi<N:
        if arrayf[testi]>LIM:
            N0_supS+=1
        testi+=1
    wxc_max = (N-N0_supS)*N0_supS**(-1.0)
    return wxc_max, N0_supS
```

Listing 2: Function used to calculate the plateau of the CCF depending on the number of sources simulated, on the minimum of the flux distribution Sn, and the flux limit of the detector.

B.2 Maps of Counts

```
def rand_distr_G(N, PXlim, LIM, nfw, sis, Sfilt,G=False, Gz = False):#PXlim == maxarcsec/ratio [ratio]==arcsec/pixel, [LIM]==Jy
    from numpy import array, isnan, random.normal, random.rand, log10, zeros, dot, pi
    SIZE = int(PXlim*2)
    conc = 4.0 #Concentration
    beta = 3 #Logarithmic slope of background source number counts
    cpar = array([(0.3089, 0.6911, 0.7)], dtype=[("omgM", "f"), ("omgL", "f"), ("h", "f")])
    Mass = 1.0e13
    mapaWOM = np.zeros((SIZE, SIZE))
    hor, ver = counts(857, 'lapi11')
    # print(hor, ver)
    ver[isnan(ver)] = 1e-20
    mn = log10(10.0**(-2.0))
    Mx = log10(100)
    arrayf = rand_flux(N, hor, ver, mn, Mx)
```

```
    testi = 0
    testb = 0
    mapaNFW = zeros((SIZE, SIZE))
    mapaSIS = zeros((SIZE, SIZE))
    if Gz ==True:
        zl_Gauss = random.normal(0.268794356307358, 0.2814263623965842, N)
        zs_Gauss = random.normal(2.2038906736872597, 0.4686407172675681, N)
        for i in range(np.shape(zl_Gauss)[0]):
            if zl_Gauss[i]<=0.0:
                zl_Gauss[i] = -1.0*zl_Gauss[i]+0.00001
            if zs_Gauss[i]<=1.0:
                zs_Gauss[i] = 1.0+(1.0-zs_Gauss[i])
            if zl_Gauss[i]>=1.0:
                zl_Gauss[i] = 1.0-(zl_Gauss[i]-int(zl_Gauss[i]))
    while testi<N:
        coordsmapa = random.rand(2)*SIZE #We assign random coordinates
        coords = coordsmapa-PXlim
        radial = dot(coords, coords)**0.5 #We calculate the radial distance
from the deflector
        if radial>PXlim:
            continue
        else:
            if Gz==False:
                if arrayf[testi]>LIM:
                    mapaWOM[int(coordsmapa[0]), int(coordsmapa[1])]+=1
                if arrayf[testi]*nfw[int(coordsmapa[0]), int(coordsmapa[1])
]>LIM:
                    mapaNFW[int(coordsmapa[0]), int(coordsmapa[1])]+=1
                    testb+=1
                if arrayf[testi]*sis[int(coordsmapa[0]), int(coordsmapa[1])
]>LIM:
                    mapaSIS[int(coordsmapa[0]), int(coordsmapa[1])]+=1
                testi+=1
            else:
                radialr = radial*pi/(180.*3600.)
                magNFW = (get_xc_NFW(radialr, Mass, zl_Gauss[testi],
zs_Gauss[testi], conc, cpar)+1.0)**(1.0/(beta-1.0))
                magSIS = (get_xc_SIS(radialr, Mass, zl_Gauss[testi],
zs_Gauss[testi], cpar)+1.0)**(1.0/(beta-1.0))
                if arrayf[testi]>LIM:
```

```
                    mapaWOM[int(coordsmapa[0]), int(coordsmapa[1])]+=1
                if arrayf[testi]*magNFW>LIM:
                    mapaNFW[int(coordsmapa[0]), int(coordsmapa[1])]+=1
                    testb+=1
                if arrayf[testi]*magSIS>LIM:
                    mapaSIS[int(coordsmapa[0]), int(coordsmapa[1])]+=1
                testi+=1
    print('el numero de mayorquemag es '+str(testb))
    print('el numero de simulated es '+str(testi))
    from scipy.ndimage import gaussian_filter
    if G==True:
        mapaWOM = gaussian_filter(mapaWOM, Sfilt)
        mapaNFW = gaussian_filter(mapaNFW, Sfilt)
        mapaSIS = gaussian_filter(mapaSIS, Sfilt)
    return mapaWOM, mapaNFW, mapaSIS
```

Listing 3: General model of function used for the generation of maps of counts. It allows for the redshift distribution of sources, although the computation time gets longer due to the nested loops, it activates with $Gz = True$. It covers as well the gausian filtering of the generated maps with $G = True$, with *Sfilt* being the filter used -typically 2.4 arcsec-. Note that *nfw* and *sis* are **magnification maps**, the same size of our resulting maps of counts. They should be built up beforehand.

```
def GENERAL_rand(N, PXlim, LIM, Sfilt, M, conc=4.0,G=False):#PXlim ==
    maxarcsec/ratio [ratio]==arcsec/pixel, [LIM]==Jy
    from numpy import array, zeros, isnan, log10, random.normal, random.rand
    , dot, pi
    SIZE = int(PXlim*2)
    conc = 4.0 #Concentration
    beta = 3 #Logarithmic slope of background source number counts
    cpar = array([(0.3089, 0.6911, 0.7)], dtype=[("omgM", "f"), ("omgL", "f"
    ), ("h", "f")])
    # Mass = 1.0e13
    mapaWOM = zeros((SIZE, SIZE))
    hor, ver = counts(857, 'lapi11')
    # print(hor, ver)
    ver[isnan(ver)] = 1e-20
    mn = log10(10.0**(-2.0))
    Mx = log10(100)
```

```
    arrayf = rand_flux(N, hor, ver, mn, Mx)
    testi = 0
    testb = 0
    mapaNFW = zeros((SIZE, SIZE))
    # mapaSIS = zeros((SIZE, SIZE))
    zl_Gauss = random.normal(0.268794356307358, 0.2814263623965842, N)
    zs_Gauss = random.normal(2.2038906736872597, 0.4686407172675681, N)
    M_Gauss = random.normal(M, 0.5*M, N)
    C_Gauss = random.normal(conc, 0.5*conc, N)
    for i in range(N):
        if zl_Gauss[i]<=0.0:
            zl_Gauss[i] = -1.0*zl_Gauss[i]+0.00001
        if zs_Gauss[i]<=1.0:
            zs_Gauss[i] = 1.0+(1.0-zs_Gauss[i])
        if zl_Gauss[i]>=1.0:
            zl_Gauss[i] = 1.0-(zl_Gauss[i]-int(zl_Gauss[i]))
        if M_Gauss[i]<=0.0:
            M_Gauss[i] = M+M_Gauss[i]
        if C_Gauss[i] <= 0.0:
            C_Gauss[i] = conc + C_Gauss[i]
    while testi<N:
        coordsmapa = random.rand(2)*SIZE #We assign random coordinates
        coords = coordsmapa-PXlim
        radial = dot(coords, coords)**0.5 #We calculate the radial distance
from the deflector
        if radial>PXlim:
            continue
        else:
            radialr = radial*pi/(180.*3600.)
            magNFW = (get_xc_NFW(radialr, M_Gauss[i], zl_Gauss[testi],
zs_Gauss[testi], C_Gauss[i], cpar)+1.0)**(1.0/(beta-1.0))
            magSIS = (get_xc_SIS(radialr, M_Gauss[i], zl_Gauss[testi],
zs_Gauss[testi], cpar)+1.0)**(1.0/(beta-1.0))
            if arrayf[testi]>LIM:
                mapaWOM[int(coordsmapa[0]), int(coordsmapa[1])]+=1
            if arrayf[testi]*magNFW>LIM:
                mapaNFW[int(coordsmapa[0]), int(coordsmapa[1])]+=1
                testb+=1
                print(testb)
            if arrayf[testi]*magSIS>LIM:
```

```
                mapaSIS[int(coordsmapa[0]), int(coordsmapa[1])]+=1
            testi+=1
    print('el numero de mayorquemag es '+str(testb))
    print('el numero de simulated es '+str(testi))
    from scipy.ndimage import gaussian_filter
    if G==True:
        mapaWOM = gaussian_filter(mapaWOM, Sfilt)
        mapaNFW = gaussian_filter(mapaNFW, Sfilt)
        mapaSIS = gaussian_filter(mapaSIS, Sfilt)
    return mapaWOM, mapaNFW, mapaSIS
```

Listing 4: Function used for the generation of maps in a realistic way that takes into account all the astrophysical parameters: mass, concentration and redshift distributions.

```
def double_distr_G(N, PXlim, LIM, mag, Sfilt, G=False, N_M = 1.0):
    from numpy import zeros, isnan, log10, random.rand, dot
    SIZE = int(PXlim*2)
    mapaWOM = zeros((SIZE, SIZE))
    mapaMAG = zeros((SIZE, SIZE))
    hor, ver = counts(857, 'lapi11')
    ver[isnan(ver)] = 1e-20
    mn = log10(10.0**(-2.0))
    Mx = log10(100)
    arrayf = rand_flux(N, hor, ver, mn, Mx)
    NT = 0
    testi = 0
    testb = 0

    while testb<N_M:
        coordsmapa = random.rand(2)*SIZE #We assign random coordinates
        coords = coordsmapa-PXlim
        radial = dot(coords, coords)**0.5 #We calculate the radial distance
    from the deflector
        if radial>PXlim:
            continue
        else:
            if testi>N-2:
                NT = NT+testi
                arrayf = rand_flux(N, hor, ver, mn, Mx)
                testi = 1
```

```
            testi+=1
            # if testi % 100.0 == 0.0 and testi>0.0:
            #     print(testi/100.0)
            if arrayf[testi]>LIM:
                mapaWOM[int(coordsmapa[0]), int(coordsmapa[1])]+=1
            if arrayf[testi]*mag[int(coordsmapa[0]), int(coordsmapa[1])]>LIM
    :
                mapaMAG[int(coordsmapa[0]), int(coordsmapa[1])]+=1
                testb+=1
                if testb % 1000.0 == 0.0:
                    print(testb/1000.0)
    NT = NT+testi
    print('el numero de mayorquemag es '+str(testb))
    print('el numero de simulated es '+str(NT))
    from scipy.ndimage import gaussian_filter
    if G==True:
        mapaWOM = gaussian_filter(mapaWOM, Sfilt)
        mapaMAG = gaussian_filter(mapaMAG, Sfilt)
    return mapaWOM, mapaMAG
```

Listing 5: Function used to generate the maps of counts used in section 6 for the compound profiles.

```
def caso1025(Min, Cin, Minter, LOCinter, Mout, Cout, TMN):
    from numpy import array, linspace, pi, zeros_like, zeros
    zl = 0.268794356307358 #Mean redshift of the lenses
    zs = 2.2038906736872597 #Mean redshift of the sources
    beta = 3 #Logarithmic slope of background source number counts
    cpar = array([(0.3089, 0.6911, 0.7)], dtype=[("omgM", "f"), ("omgL", "f"
    ), ("h", "f")])
    size = 250.0/TMN
    radios = linspace(0.5*size, (TMN-0.5)*size, TMN)
    radiosrad = radios*pi/(3600.0*180.0)

    radiosinter = zeros_like(radios)
    for i in range(TMN):
        if radios[i]<LOCinter:
            radiosinter[i]=(LOCinter-0.5-i)*size
        else:
            radiosinter[i]=(i-LOCinter+0.5)*size
```

```
    radiosinterrad = radiosinter*pi/(3600.0*180.0)
    mag_in = (get_xc_NFW(radiosrad, Min, zl, zs, Cin, cpar)+1)**(1/(beta -1)
    )
    mag_inter = (get_xc_SIS(radiosinterrad, Minter, zl, zs, cpar)+1)**(1/(
    beta -1))
    mag_out = (get_xc_NFW(radiosrad, Mout, zl, zs, Cout, cpar)+1)**(1/(beta
    -1))

    MAG = mag_in*mag_inter*mag_out

    MAPA = zeros((TMN*2, TMN*2))
    for i in range(TMN*2):
        print(i)
        for j in range(TMN*2):
            if i < TMN:
                if j < TMN:
                    pos = (((TMN-0.5-i)*size)**2+ ((TMN-0.5-j)*size)**2)
    **0.5
                else:
                    pos = (((TMN-0.5-i)*size)**2+((j-(TMN-0.5))*size)**2)
    **0.5
            else:
                if j < TMN:
                    pos = (((TMN-0.5-j)*size)**2+((i-(TMN-0.5))*size)**2)
    **0.5
                else:
                    pos = (((j-(TMN-0.5))*size)**2+((i-(TMN-0.5))*size)**2)
    **0.5
            for k in range(TMN):
                if pos>k*size and pos<(k+1.0)*size:
                    MAPA[i, j] = MAG[k]
    return MAPA
```

Listing 6: Function used to generate a map of magnification with an introduced SIS profile at an angular separation defined by *LOCinter*.

```
def caso1025B(Min, Cin, Minter, LOCinter, Mouter, LOCouter, Mouter2,
    LOCouter2, Mouter3, LOCouter3, Mouter4, LOCouter4, TMN):
    from numpy import array, linspace, zeros_like, pi
    zl = 0.268794356307358 #Mean redshift of the lenses
```

```
    zs = 2.2038906736872597 #Mean redshift of the sources
    beta = 3 #Logarithmic slope of background source number counts
    cpar = array([(0.3089, 0.6911, 0.7)], dtype=[("omgM", "f"), ("omgL", "f"
), ("h", "f")])
    size = 250.0/TMN
    radios = linspace(0.5*size, (TMN-0.5)*size, TMN)
    radiosrad = radios*pi/(3600.0*180.0)

    radiosinter = zeros_like(radios)
    radiosouter = zeros_like(radios)
    radiosouter2 = zeros_like(radios)
    radiosouter3 = zeros_like(radios)
    radiosouter4 = zeros_like(radios)
    for i in range(TMN):
        if radios[i]<LOCinter:
            radiosinter[i]=(LOCinter-0.5-i)*size
        else:
            radiosinter[i]=(i-LOCinter+0.5)*size
        if radios[i]<LOCouter:
            radiosouter[i]=(LOCouter-0.5-i)*size
        else:
            radiosouter[i]=(i-LOCouter+0.5)*size
        if radios[i]<LOCouter2:
            radiosouter2[i]=(LOCouter2-0.5-i)*size
        else:
            radiosouter2[i]=(i-LOCouter2+0.5)*size
        if radios[i]<LOCouter3:
            radiosouter3[i]=(LOCouter3-0.5-i)*size
        else:
            radiosouter3[i]=(i-LOCouter3+0.5)*size
        if radios[i]<LOCouter4:
            radiosouter4[i]=(LOCouter4-0.5-i)*size
        else:
            radiosouter4[i]=(i-LOCouter4+0.5)*size
    radiosinterrad = radiosinter*pi/(3600.0*180.0)
    radiosouterrad = radiosouter*pi/(3600.0*180.0)
    radiosouterrad2 = radiosouter2*pi/(3600.0*180.0)
    radiosouterrad3 = radiosouter3*pi/(3600.0*180.0)
    radiosouterrad4 = radiosouter4*pi/(3600.0*180.0)
    mag_in = (get_xc_NFW(radiosrad, Min, zl, zs, Cin, cpar)+1)**(1/(beta -1)
```

```
    )
    mag_inter = (get_xc_SIS(radiosinterrad, Minter, zl, zs, cpar)+1)**(1/(beta -1))
    mag_out = (get_xc_SIS(radiosouterrad, Mouter, zl, zs, cpar)+1)**(1/(beta -1))
    mag_out2 = (get_xc_SIS(radiosouterrad2, Mouter2, zl, zs, cpar)+1)**(1/(beta -1))
    mag_out3 = (get_xc_SIS(radiosouterrad3, Mouter3, zl, zs, cpar)+1)**(1/(beta -1))
    mag_out4 = (get_xc_SIS(radiosouterrad4, Mouter3, zl, zs, cpar)+1)**(1/(beta -1))

    MAG = mag_in*mag_inter*mag_out*mag_out2*mag_out3*mag_out4

    MAPA = np.zeros((TMN*2, TMN*2))
    for i in range(TMN*2):
        print(i)
        for j in range(TMN*2):
            if i < TMN:
                if j < TMN:
                    pos = (((TMN-0.5-i)*size)**2+ ((TMN-0.5-j)*size)**2)**0.5
                else:
                    pos = (((TMN-0.5-i)*size)**2+((j-(TMN-0.5))*size)**2)**0.5
            else:
                if j < TMN:
                    pos = (((TMN-0.5-j)*size)**2+((i-(TMN-0.5))*size)**2)**0.5
                else:
                    pos = (((j-(TMN-0.5))*size)**2+((i-(TMN-0.5))*size)**2)**0.5
            for k in range(TMN):
                if pos>k*size and pos<(k+1.0)*size:
                    MAPA[i, j] = MAG[k]
    return MAPA
```

Listing 7: Function used in section 6.2 to produce a requence of SIS profiles imitating the variable behaviour of the observed CCF in the fourth bin of richness in FER22.

B.3 CCF Construction and Fitting

```
def xc_maker (SinMG, MG, radio, ssnMG, sMG):
    salida = array([])
    radiosalida = array([])
    sigmasalida = array([])
    for i in range(shape(SinMG)[0]):
        if SinMG[i]==0.0:
            continue
        else:
            salidai = MG[i]/SinMG[i]-1
            salida = append(salida, salidai)
            radiosalida = append(radiosalida, radio[i])
            if MG[i]==0.0:
                sigmasalida = append(sigmasalida, salidai*(ssnMG[i]/SinMG[i
   ]))
            else:
                sigmasalida = append(sigmasalida, salidai*(ssnMG[i]/SinMG[i]
    + sMG[i]/MG[i]))
    return salida, sigmasalida, radiosalida
```

Listing 8: Function used to produce the arrays of observed CCF, the associated uncertainty and the array of angular separations associated to each data point of the CCF trend.

```
def plateauXC (XC_arr, plateau):
    from numpy import copy, shape
    salida = copy(XC_arr)
    for i in range(shape(salida)[0]):
        if salida[i]>plateau:
            salida[i]=plateau
    return salida
```

Listing 9: Function used to modify the theoretical CCFs in order to add the plateau.

```
def MBF_parts(rxc, xcobs, sigma_xcobs, prof, M, S):
    from numpy import logspace, array, zeros_like, shape, sum, argmin, amin,
    amax, pi
    Ms = logspace(11.5, 17.5, 10000)
```

```
    cpar = array([(0.3089, 0.6911, 0.7)], dtype=[("omgM", "f"), ("omgL", "f"
), ("h", "f")]) #Wikipedia https://en.wikipedia.org/wiki/Lambda-CDM_model
    zl = 0.268794356307358 #Mean redshift of the lenses
    zs = 2.2038906736872597 #Mean redshift of the sources
    conc = 4.0 #Concentration
    beta = 3.0 #Logarithmic slope of background source number counts

    radrxc = rxc*pi/(180.0*3600.0)

    msqs = zeros_like(Ms)
    msqs_up = zeros_like(Ms)
    msqs_down = zeros_like(Ms)
    from scipy.ndimage import gaussian_filter1d
    for i in range(shape(Ms)[0]):
        if prof=='NFW':
            msqs[i] = sum((gaussian_filter1d(plateauXC(get_xc_NFW(radrxc, Ms
[i], zl, zs, conc, cpar), 8.257)-xcobs), S)**2.0)
            msqs_up[i] = sum((gaussian_filter1d(plateauXC(get_xc_NFW(radrxc,
 Ms[i], zl, zs, conc, cpar), 8.257)-(xcobs+sigma_xcobs)), S)**2.0)
            msqs_down[i] = sum((gaussian_filter1d(plateauXC(get_xc_NFW(
radrxc, Ms[i], zl, zs, conc, cpar), 8.257)-(xcobs-sigma_xcobs)), S)**2.0)
        if prof=='SIS':
            msqs[i] = sum((gaussian_filter1d(plateauXC(get_xc_SIS(radrxc, Ms
[i], zl, zs, cpar), 8.257)-xcobs), S)**2.0)
            msqs_up[i] = sum((gaussian_filter1d(plateauXC(get_xc_SIS(radrxc,
 Ms[i], zl, zs, cpar), 8.257)-(xcobs+sigma_xcobs)), S)**2.0)
            msqs_down[i] = sum((gaussian_filter1d(plateauXC(get_xc_SIS(
radrxc, Ms[i], zl, zs, cpar), 8.257)-(xcobs-sigma_xcobs)), S)**2.0)

    MASSOUT = Ms[argmin(msqs)]/M
    S_up = Ms[argmin(msqs_up)]/M
    S_down = Ms[argmin(msqs_down)]/M
    return MASSOUT, amin(array([S_up, S_down])), amax(array([S_up, S_down]))
```

Listing 10: Function developed to perform a fit on the mass parameter from the observed CCFs, with a least squares method built up by hand.

```
def MBF_parts_TOT(rxc, xcobs, sigma_xcobs, M, S):
    from numpy import logspace, array, pi, zeros_like, shape, sum, argmin,
amin, amax
```

```
    Ms = logspace(11.5, 17.5, 10000)
    cpar = array([(0.3089, 0.6911, 0.7)], dtype=[("omgM", "f"), ("omgL", "f"), ("h", "f")]) #Wikipedia https://en.wikipedia.org/wiki/Lambda-CDM_model
    zl = 0.268794356307358 #Mean redshift of the lenses
    zs = 2.2038906736872597 #Mean redshift of the sources
    conc = 4.0 #Concentration
    beta = 3.0 #Logarithmic slope of background source number counts

    radrxc = rxc*pi/(180.0*3600.0)

    msqsNFW = zeros_like(Ms)
    msqs_upNFW = zeros_like(Ms)
    msqs_downNFW = zeros_like(Ms)
    msqsSIS = zeros_like(Ms)
    msqs_upSIS = zeros_like(Ms)
    msqs_downSIS = zeros_like(Ms)
    from scipy.ndimage import gaussian_filter1d
    for i in range(shape(Ms)[0]):
        msqsNFW[i] = sum((gaussian_filter1d(plateauXC(get_xc_NFW(radrxc, Ms[i], zl, zs, conc, cpar), 8.257)-xcobs), S)**2.0)
        msqs_upNFW[i] = sum((gaussian_filter1d(plateauXC(get_xc_NFW(radrxc, Ms[i], zl, zs, conc, cpar), 8.257)-(xcobs+sigma_xcobs)), S)**2.0)
        msqs_downNFW[i] = sum((gaussian_filter1d(plateauXC(get_xc_NFW(radrxc, Ms[i], zl, zs, conc, cpar), 8.257)-(xcobs-sigma_xcobs)), S)**2.0)
        msqsSIS[i] = sum((gaussian_filter1d(plateauXC(get_xc_SIS(radrxc, Ms[i], zl, zs, cpar), 8.257)-xcobs), S)**2.0)
        msqs_upSIS[i] = sum((gaussian_filter1d(plateauXC(get_xc_SIS(radrxc, Ms[i], zl, zs, cpar), 8.257)-(xcobs+sigma_xcobs)), S)**2.0)
        msqs_downSIS[i] = sum((guassian_filter1d(plateauXC(get_xc_SIS(radrxc, Ms[i], zl, zs, cpar), 8.257)-(xcobs-sigma_xcobs)), S)**2.0)

    MASSOUTNFW = Ms[argmin(msqsNFW)]/M
    MASSOUTSIS = Ms[argmin(msqsSIS)]/M
    if abs(MASSOUTNFW-1)>abs(MASSOUTSIS-1):
        print('SIS')
        S_up = Ms[argmin(msqs_upSIS)]/M
        S_down = Ms[argmin(msqs_downSIS)]/M
        print(MASSOUTSIS, amin(array([S_up, S_down])), amax(array([S_up, S_down])))
        return MASSOUTSIS, amin(array([S_up, S_down])), amax(array([S_up,
```

```
    S_down]))
35     else:
36         print('NFW')
37         S_up = Ms[argmin(msqs_upNFW)]/M
38         S_down = Ms[argmin(msqs_downNFW)]/M
39         print(MASSOUTNFW, amin(array([S_up, S_down])), amax(array([S_up,
    S_down])))
40         return MASSOUTNFW, amin(array([S_up, S_down])), amax(array([S_up,
    S_down]))
```

Listing 11: Function used to test the ability of the simulator to differentiate SIS from NFW observed CCFs.

```
1  def M_L(rxc, xcobs, prof, M):
2      from numpy import log10, pi, array, shape, append
3      xcobs_LC = log10(xcobs)
4      from scipy.optimize import curve_fit
5      radrxc = rxc*pi/(180.0*3600.0)
6      radrxc_LC = log10(radrxc)
7      radrxc_L = array([])
8      xcobs_L = array([])
9      for i in range(shape(xcobs_LC)[0]):
10         if xcobs_LC[i]>0.00001:
11             radrxc_L = append(radrxc_L, radrxc_LC[i])
12             xcobs_L = append(xcobs_L, xcobs_LC[i])
13     if prof == 'NFW':
14         pars, dpars = curve_fit(get_xc_NFW_M, radrxc_L, xcobs_L, p0=[M],
    bounds=(0.5*M, 2.0*M))
15     if prof == 'SIS':
16         pars, dpars = curve_fit(get_xc_SIS_M, radrxc_L, xcobs_L, p0=[M],
    bounds=(0.5*M, 2.0*M))
17     return pars, dpars
```

Listing 12: *curve_fit* adapted function to perform the filtered theoretical + plateau mass fit of the CCFs.

```
1  def MC(rxc, xcobs, M, C):
2      xcobs_LC = np.log10(xcobs)
3      from scipy.optimize import curve_fit
4      radrxc = rxc*np.pi/(180.0*3600.0)
```

```
    radrxc_LC = np.log10(radrxc)
    radrxc_L = np.array([])
    xcobs_L = np.array([])
    for i in range(np.shape(xcobs_LC)[0]):
        if xcobs_LC[i]>0.00001:
            radrxc_L = np.append(radrxc_L, radrxc_LC[i])
            xcobs_L = np.append(xcobs_L, xcobs_LC[i])
    pars, dpars = curve_fit(get_xc_NFW_MC, radrxc_L, xcobs_L, p0=[M, C],
   bounds=((0.5*M, 0.5*C), (2.0*M, 2.0*C)))
    return pars, dpars
```

Listing 13: *curve_fit* adapted function to perform the filtered theoretical + plateau mass and concentration fit of the CCFs.

```
def fit_2NFW(rxc, xcobs, Min, Cin, Mout, Cout):
    from numpy import log10, pi, array, shape, append
    xcobs_LC = log10(xcobs)
    from scipy.optimize import curve_fit
    radrxc = rxc*pi/(180.0*3600.0)
    radrxc_LC = log10(radrxc)
    radrxc_L = array([])
    xcobs_L = array([])
    for i in range(shape(xcobs_LC)[0]):
        if xcobs_LC[i]>0.00001:
            radrxc_L = append(radrxc_L, radrxc_LC[i])
            xcobs_L = append(xcobs_L, xcobs_LC[i])
    pars, dpars = curve_fit(get_xc_2NFW, radrxc_L, xcobs_L, p0=[Min, Cin,
   Mout, Cout], bounds=((0.2*Min, 0.2*Cin,0.2*Mout, 0.2*Cout), (10.0*Min,
   10.0*Cin,10.0*Mout, 10.0*Cout)))
    return pars, dpars
```

Listing 14: *curve_fit* adapted function to perform the filtered theoretical + plateau mass and concentration fit of a compound profile made up of two NFW individual ones.

```
def fit_NFWSIS(rxc, xcobs, Min, Mout, C):
    from numpy import log10, pi, array, shape, append
    xcobs_LC = log10(xcobs)
    from scipy.optimize import curve_fit
    radrxc = rxc*pi/(180.0*3600.0)
    radrxc_LC = log10(radrxc)
    radrxc_L = array([])
    xcobs_L = array([])
```

```
    for i in range(shape(xcobs_LC)[0]):
        if xcobs_LC[i]>0.00001:
            radrxc_L = append(radrxc_L, radrxc_LC[i])
            xcobs_L = append(xcobs_L, xcobs_LC[i])
    pars, dpars = curve_fit(get_xc_NFWSIS, radrxc_L, xcobs_L, p0=[Min,Mout,
    C], bounds=((0.2*Min,0.2*Mout, 0.2*C), (10.0*Min,10.0*Mout, 10.0*C)))
    return pars, dpars
```

Listing 15: *curve_fit* adapted function to perform the filtered theoretical + plateau mass and concentration fit of a compound profile made up of one NFW for the cluster halo and a SIS one for the BCG.

```
def cortes_compound(modo, Mout, Min, profin, Cout, Cin = 1.0):
    from numpy import logspace, pi, shape
    r = logspace(-1, 3, 10000)
    rrad = r*pi/(180.0*3600.0)
    xc_out = get_xc_NFW(rrad, Mout, zl, zs, Cout, cpar)
    if profin == 'SIS':
        xc_in = get_xc_SIS(rrad, Min, zl, zs, cpar)
    if profin == 'NFW':
        xc_in = get_xc_NFW(rrad, Min, zl, zs, Cin, cpar)

    if modo == 'byhand':
        return r, xc_out, xc_in
    if modo != 'byhand':
        prueba = xc_in - xc_out
        for i in range(shape(prueba)[0]-1):
            if prueba[i]*prueba[i+1] < 0.0:
                donde = r[i]
            else:
                continue
        if modo == 'indicativo':
            return donde
        if modo == 'todo':
            return donde, r, xc_out, xc_in
```

Listing 16: *curve_fit* adapted function to perform the filtered theoretical + plateau mass and concentration fit of a compound profile made up of one NFW for the cluster halo and a SIS one for the BCG.

C Additional Figures

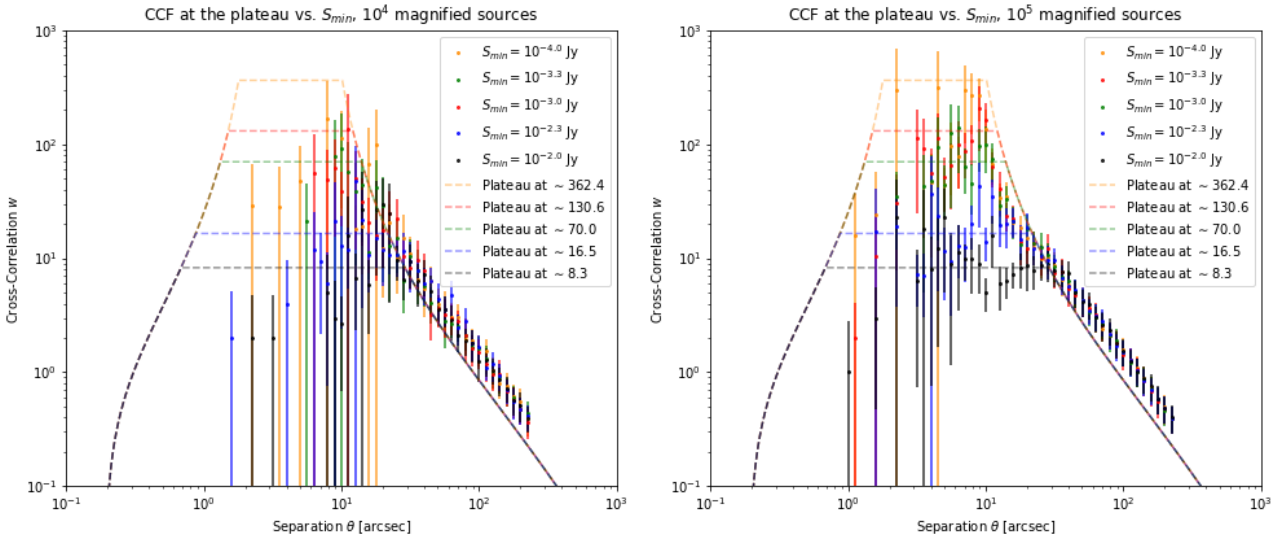

Figure C.1: Relating to figure 5.14, the left and right panel show respectively the change of the plateau region of the CCF for 10^4 and 10^5 magnified sources.

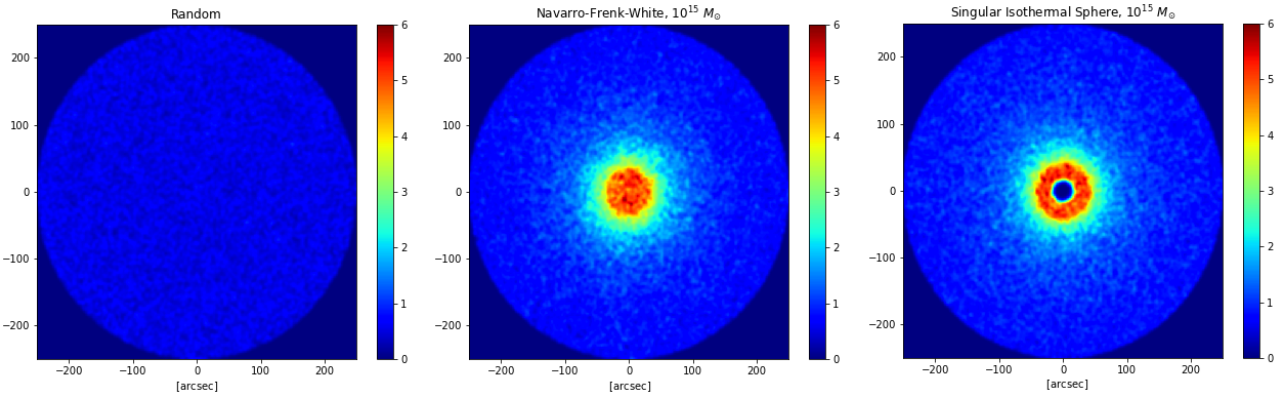

Figure C.2: Same representation as figure 5.18 but for a deflector mass of 10^{15} $M_\odot$.

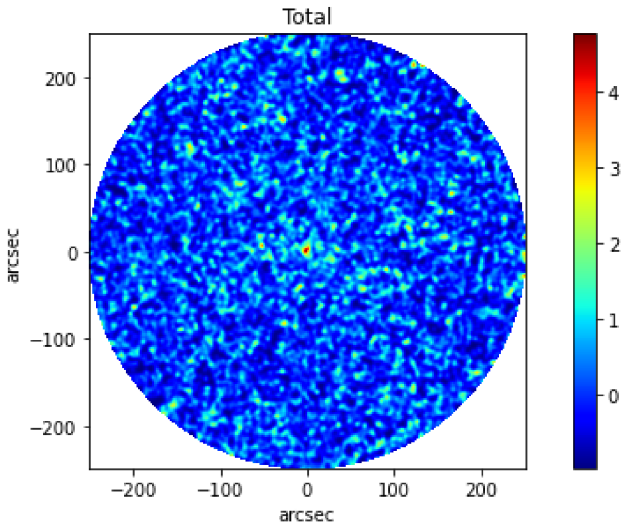

Figure C.3: Smoothed map of the observed sources in FER22 (figure 2a).

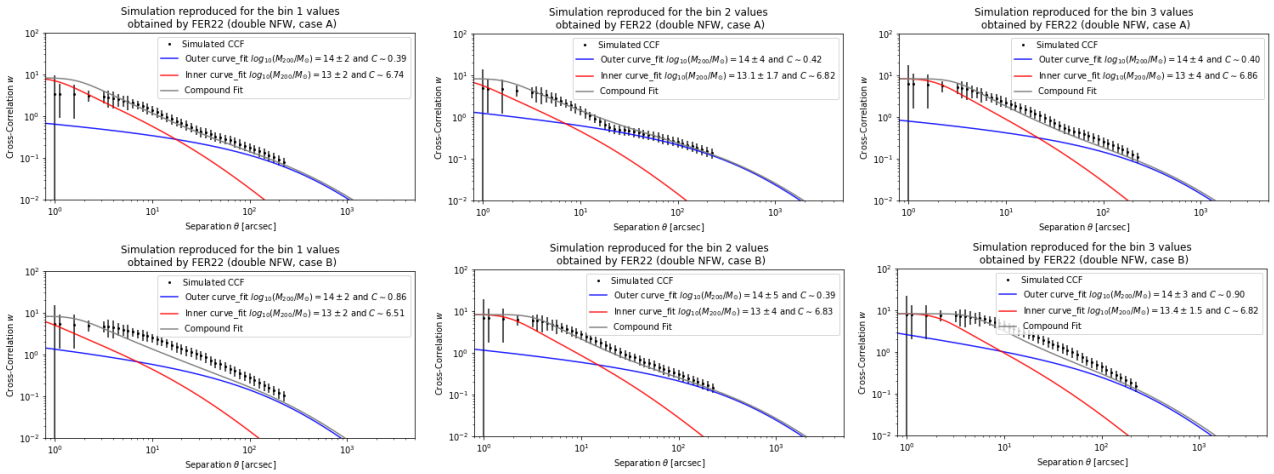

Figure C.4: Best fit to the observed compound CCFs for the double NFW profile. Maps of counts built up with input parameters the results for the first three bins of richness in FER22. Go to table 3.1 to consult them.

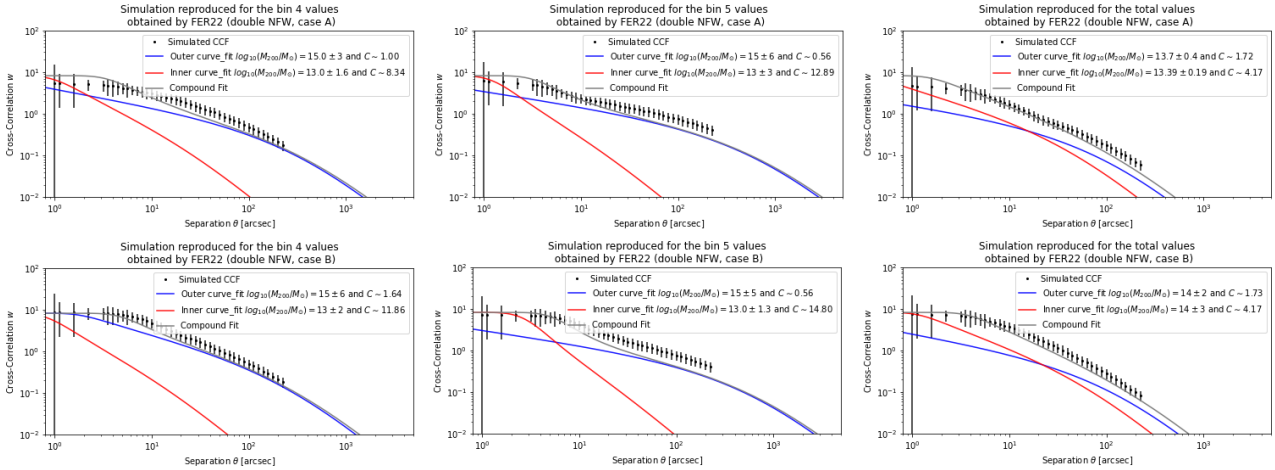

Figure C.5: Best fit to the observed compound CCFs for the double NFW profile. Maps of counts built up with input parameters the results for last two bins of richness and the total in FER22. Go to table 3.1 to consult them.

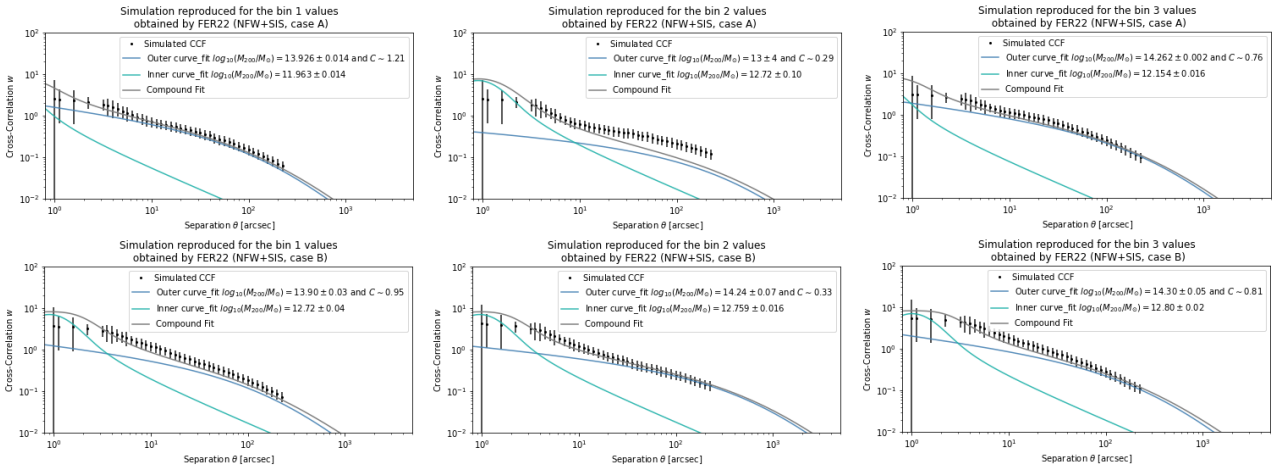

Figure C.6: Best fit to the observed compound CCFs for the SIS + NFW profile. Maps of counts built up with input parameters the results for the first three bins of richness in FER22. Go to table 3.1 to consult them.

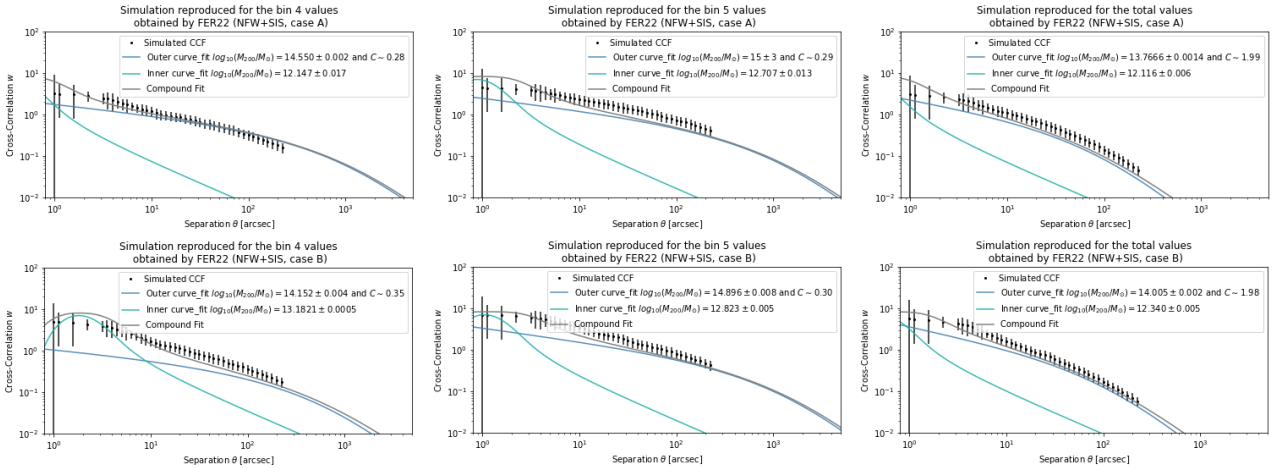

Figure C.7: Best fit to the observed compound CCFs for the SIS + NFW profile. Maps of counts built up with input parameters the results for last two bins of richness and the total in FER22. Go to table 3.1 to consult them.

	Parameters	Bin 1		Bin 2		Bin 3	
	$[M] \equiv 10^{13}\ M_\odot$	FER22	Out A	FER22	Out A	FER22	Out A
SIS + NFW	$M_{\rm SIS}$	0.5	0.1	0.6	0.5	0.6	0.1
	$M_{\rm NFW}$	4.9	8.4	5.3	2.4	10.1	18.3
	C	0.94	1.21	0.30	0.29	1.17	0.76
Outer	$M_{\rm NFW}$	5.8	5.7	7.9	16.9	11.2	8.4
	C	0.74	0.39	0.39	0.42	1.00	0.40
Inner	$M_{\rm NFW}$	3.8	1.5	2.3	1.2	7.2	2.4
	C	3.63	6.74	6.83	6.82	3.81	6.86
Inner + Outer	$M_{\rm TOT}$	9.6	7.3	10.2	18.1	18.4	10.9

Table C.1: Output values from our fitting algorithm after having introduced FER22 results, accounting for bins from 1 to 3. Magnification calculated for the case A.

	Parameters	Bin 4		Bin 5		Total	
	$[M] \equiv 10^{13}\ M_\odot$	FER22	Out A	FER22	Out A	FER22	Out A
SIS + NFW	$M_{\rm SIS}$	0.6	0.1	1.0	0.5	0.5	0.1
	$M_{\rm NFW}$	14.0	35.5	51.5	55.1	5.5	5.8
	C	0.65	0.28	0.56	0.29	1.84	1.99
Outer	$M_{\rm NFW}$	27.4	32.9	51.5	54.1	7.1	4.6
	C	1.74	1.00	0.56	0.56	1.72	1.72
Inner	$M_{\rm NFW}$	1.0	0.9	1.0	0.5	4.1	2.5
	C	11.91	8.34	14.8	12.89	4.17	4.17
Inner + Outer	$M_{\rm TOT}$	28.4	33.8	52.5	54.6	11.2	7.0

Table C.2: Output values from our fitting algorithm after having introduced FER22 results, bins 4, 5 and the totals. Magnification calculated for the case A.

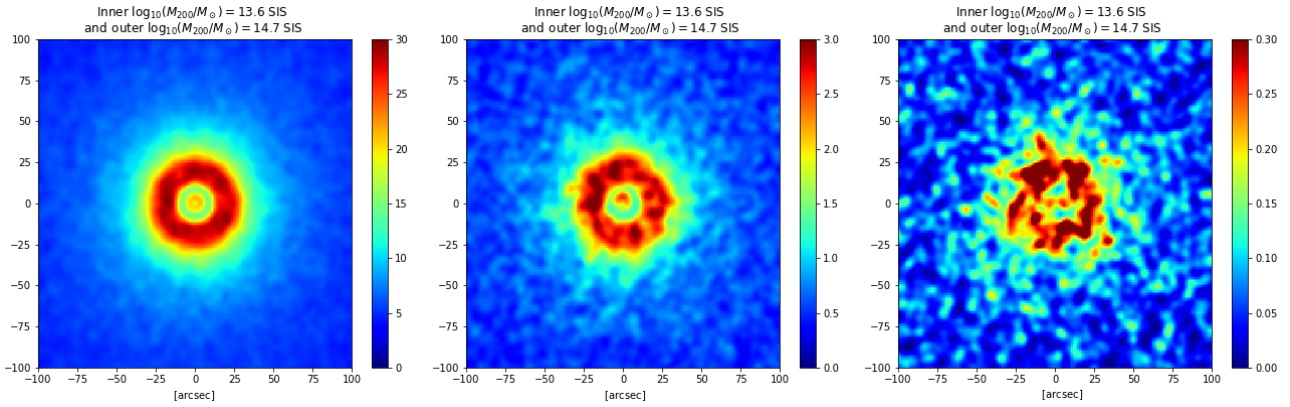

Figure C.8: Map of counts for the double SIS profile for which the simulated CCF is presented in the left panel in figure 6.5. From left to right we simulated 10^6, 10^5 and 10^4 sources. We have chosen a window of 200×200 arcsec^2 so that features are better seen. For further information go to section 6.1.

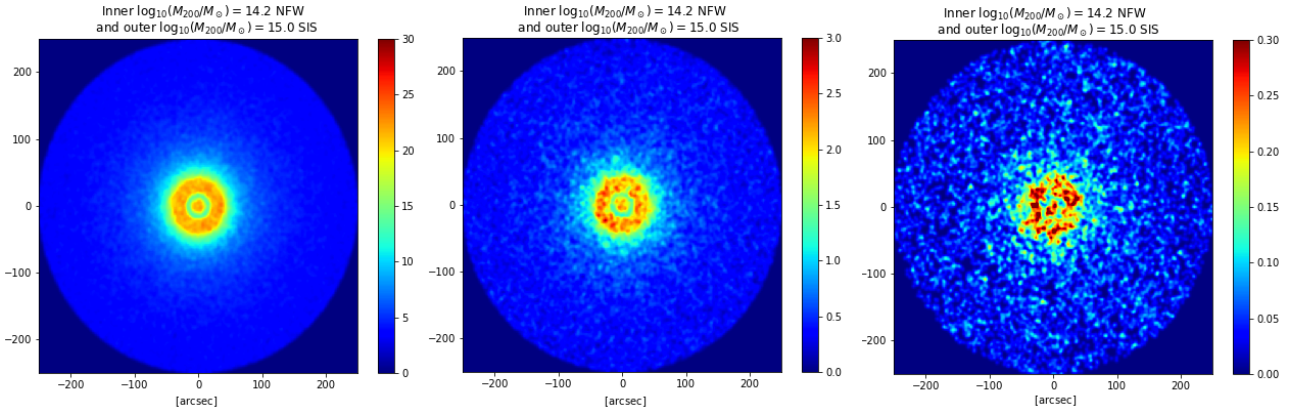

Figure C.9: Map of counts for the outer $10^{15.0}\ M_\odot$ SIS profile and inner $10^{14.2}\ M_\odot$ with concentration 6, for which the simulated CCF is presented in the right panel in figure 6.5. From left to right we simulated 10^6, 10^5 and 10^4 sources. For further information go to section 6.1.

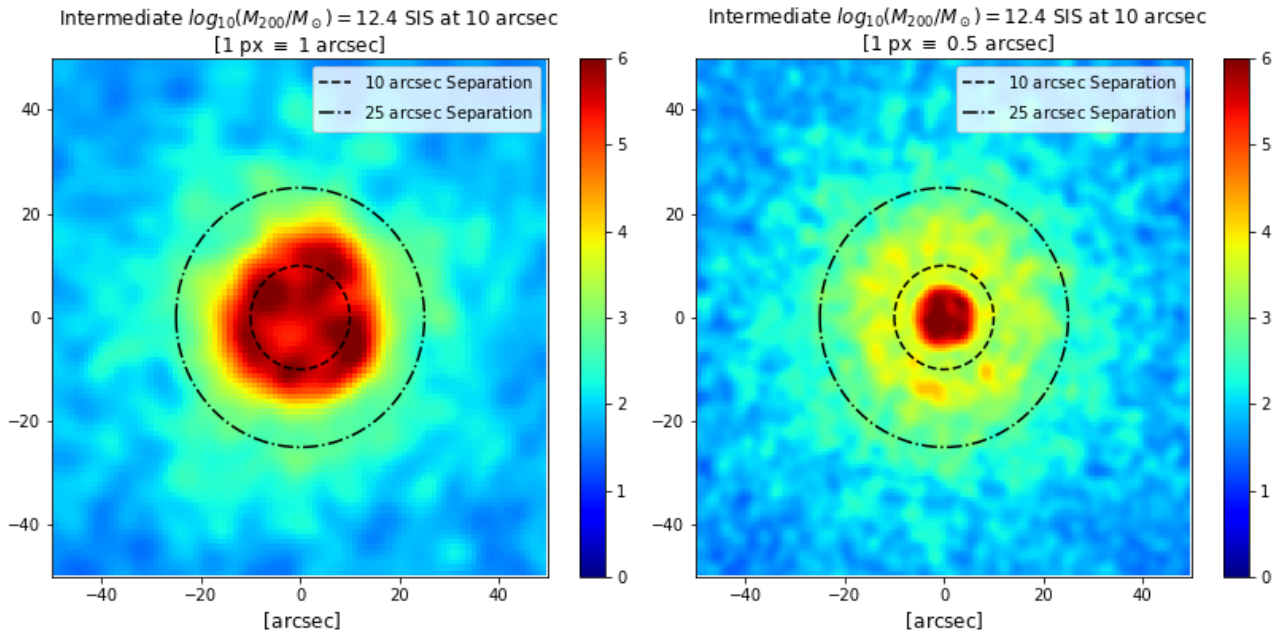

Figure C.10: Maps of counts simulated to build up CCFs in figure 6.8. A $10^{12.6}$ $M_\odot$ SIS profile was introduced at $\sim$ 12.6 arcsec. At the left the pixel size is 1 arcsec/px. At the right, 0.5 arcsec/px.